Operation and Control of a Two-Stroke, Free-Piston-Engine-Driven Linear Alternator

by

Shihab M. Elborai

Submitted to the Department of Electrical Engineering and Computer Science
in partial fulfillment of the requirements for the degrees of

Master of Engineering in Electrical Engineering and Computer Science

and

Bachelor of Science in Electrical Science and Engineering

at the

MASSACHUSETTS INSTITUTE OF TECHNOLOGY

June 2000

Author .....
Department of Electrical Engineering and Computer Science
May 22, 2000

Certified by .....
Dr. Stephen D. Umans
Principal Research Engineer
Thesis Supervisor

Accepted by .....
Arthur C. Smith
Chairman, Department Committee on Graduate Students

Operation and Control of a Two-Stroke, Free-Piston-Engine-Driven Linear Alternator

by

Shihab M. Elborai

Submitted to the Department of Electrical Engineering and Computer Science
on May 22, 2000, in partial fulfillment of the
requirements for the degrees of
Master of Engineering in Electrical Engineering and Computer Science
and
Bachelor of Science in Electrical Science and Engineering

Abstract

The modeling effort documented in this thesis investigates the operation and control of a two-stroke, free-piston-engine driven linear-alternator for resistive and battery-charging loads. First-principles models of each of the individual components of the system were tied together into a dynamic model of the overall system. A constant step-size, fourth-order Runge-Kutta algorithm was used to numerically simulate the engine/alternator/load system. The simulation predicts the existence of a range of resistive and battery loads for which steady-state operation is possible without the aid of feedback-control. The computer program embodying the model of the two-stroke, free-piston-engine driven linear-alternator enables the investigation of electromechanical design trade-offs and is intended to serve as the forerunner of a numerical design tool.

Thesis Supervisor: Dr. Stephen D. Umans
Title: Principal Research Engineer

Acknowledgments

I would like to thank my advisor Dr. Stephen Umans of the MIT Electromechanical Systems Laboratory for his excellent guidance and inexhaustible patience. His understanding and friendship have helped me make the most out of this educational experience.

I would also like to extend thanks to professor Joseph Smith of the MIT Cryogenic Engineering Laboratory for the many informative discussions we had over the course of this work. Special thanks are due to Chris Connaire, David Otten, Doris Elsemiller and Anthony Caloggero, they have made the Laboratory feel more like a family than a work place.

I am extremely fortunate to have had the opportunity to work for Professor Gerald Wilson of the MIT Electromechanical Systems Laboratory both as an undergraduate and as a graduate student. Professor Wilson is a lot more than a teacher; he is an excellent role model for any young engineer.

I would like to thank Ken Galitello of Galileo Research for providing me with the resources that made this research possible. I am also thankful for the data he made available for this thesis.

Joshua Cates and Markus Kangas have looked at my simulation code and have been invaluable references on the quirks of C-coding. Omar Roushdy, Wojtech Giziewicz, Oskar Bruening, Tetsuya Matsuguchi and Martin Calles always found interesting diversions whenever I needed a break from work, and for that they have my lasting gratitude. I thank Matthew Mishrikey for attempting to proof read parts of this thesis.

I would not be where I am today if it were not for my very special family. Foremost is my mother Suad Dakhil, who shall always remain my first teacher. My wonderful father, Mahmoud Elborai, is also my best friend. Finally I must acknowledge my dear siblings, Hisham, Marwa and Ranim for their relentless love and support.

I dedicate this thesis to my grandfather Hadj Mohammed Dakhil and to the memory of my grandmother Emmeyma Hadjah.

Contents

List of Figures

List of Tables

Chapter 1

Introduction

1.1 Background and motivation

Hybrid-electric vehicles need compact, light weight and efficient auxiliary-power units to become a commercially viable product. A system in which a linear alternator extracts energy from a two-stroke free-piston engine claims to address this need. This design also claims to provide significant savings in frictional losses, reduce weight and size, and increase durability by eliminating the conversion from linear motion to rotational motion. In addition, a battery separates the vehicle load from the engine, which should enable the engine to always run at an optimal operating speed.

The system under consideration was proposed and built by Galileo Research [1] and consists of two identical internal-combustion cylinders and two pistons joined by a rigid rod, which supports the plunger of a linear alternator. The cylinders fire so that the expansion in one cylinder drives the compression in the opposite cylinder, consequently the motion of the piston assembly results from thermodynamic as well as electro-mechanical forces.

A conventional internal-combustion engine decouples the thermal and electrical dynamics with a large reservoir of mechanical energy (i.e., a big hefty flywheel). The most interesting features of the two-stroke engine/linear-alternator derive from the

[1] Galileo Research, Inc., P.O. Box 25 Torrington, CT 06790-0025

interaction between the alternator, the engine and the load.

First-principles analytical modeling of the free-piston-engine/linear-alternator system is an important step that can greatly facilitate the realization and development of this technology. The problem is that experience with the behavior of conventional rotating-systems does not apply very well to this unconventional system. A model is needed to investigate the conditions for steady-state operation of such a system. Without a good model, the operation and tuning of the system would depend on blind trial and error.

Another reason for first-principles modeling is the investigation of electromechanical design-tradeoffs. Numerical simulation makes the study of the effects of various properties, parameters and configurations a simple, efficient and cheap endeavor. Furthermore, because the model is based on physical laws and fundamental physical models, modifications to the system's design can be readily investigated by making small adjustments to the previous models.

In addition, the model and the simulation are useful tools for gaining an understanding of the capabilities and shortcomings of this technology. These analytical tools are needed to evaluate the feasibility and impact of two-stroke free-piston engine auxiliary-power units in hybrid-electric vehicle applications.

1.2 System overview

The engine is a two-stroke internal combustion engine with a permanent-magnet plunger mounted on the rod linking the two pistons. Figure 1-1 shows the configuration of the engine and the alternator. The engine consists of two internal-combustion cylinders that fire in opposition, pushing the reciprocating assembly (pistons, plunger and link-rod) back and forth between them. Firing is timed so that the expansion in one cylinder drives the compression in the opposite cylinder. Energy is extracted from the engine on every stroke, as the reciprocating assembly carries the plunger into and out of the stator iron. The output of the alternator is full-wave rectified into a battery, which in turn drives a load.

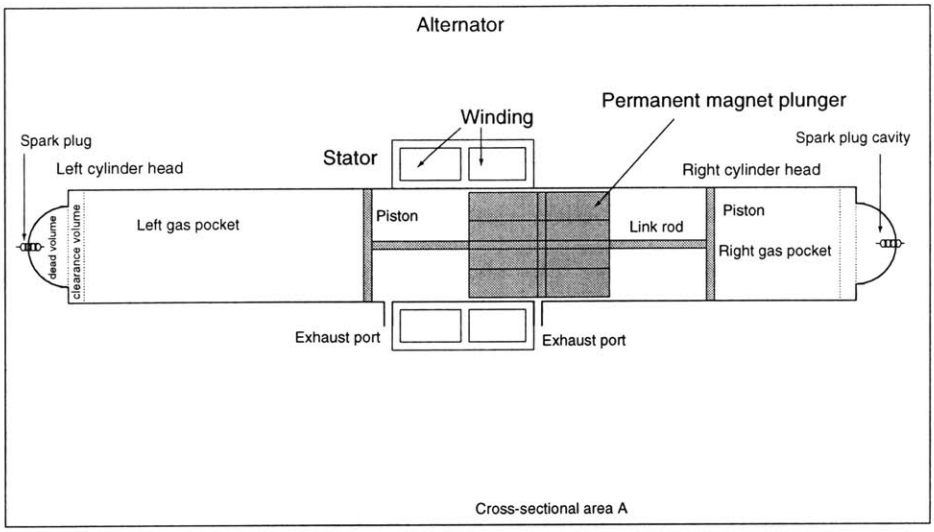

Figure 1-1: Schematic of the configuration of the engine/alternator/load

1.3 Modeling approach

A model of the two-stroke engine linear-alternator system has been developed and implemented in C-code to investigate steady-state operation under different loads. This model combines simple analytical models of the three components of the engine/alternator/load system in a dynamic simulation to investigate the interaction between the engine thermodynamics, the alternator electromechanics and the power delivered to the load.

1.4 Preview

Chapter 2 presents a simple model of the linear-alternator's electromechanics. The alternator is modeled by an equivalent lumped-parameter circuit with an internal voltage source, winding inductance and winding resistance.

Chapter 3 describes a model for the thermodynamics of the two-stroke free-piston reciprocating engine. The standard Otto cycle with instantaneous combustion and exhaust events was chosen to model the engine's cycle. The model computes the force on the plunger due to the difference in pressure between the two cylinders. The goal is to capture the role of the engine without resorting to sophisticated modeling.

Chapter 4 starts by briefly documenting the models used to investigate the effects of different electrical loads on the operation of the system. The chapter then proceeds to describe the framework of the overall system-model. In particular, it documents how the models for the three components (alternator, engine, load) combine to form an overall system-model. The chapter also details some of the features of the implemented numerical simulation.

Chapter 5 discusses the predictions and results of the numerical simulation.

Chapter 6 compares the predictions of the model to some preliminary experimental data.

Chapter 7 presents conclusions and recommendations for further work.

Chapter 2

Modeling the linear alternator

2.1 Geometry of the alternator

Figure 2-1 displays the cross-sectional geometry of the linear alternator under consideration[1]. Note that the plunger consists of thirty two permanent-magnets with azimuthal fields that are mounted radially on eight symmetric arms stemming from a non-magnetic shaft so that the magnets move into and out of the stator iron as the plunger reciprocates. The magnets on either side of an arm have the same polarity. A set of magnets of opposite polarity are mounted behind the set of sixteen shown in Figure 2-1, so that the magnetic-flux through each air gap sums to zero when the plunger is centered in the stator. Figure 2-2 shows an axial view of the plunger.

The stator has eight wedge-shaped iron pole pieces. Coils are wound around each pole piece and are connected in series to extract energy from the plunger and deliver it to the load. The magnets on each arm have the opposite polarity of their counterparts in the contiguous arms, so that the magnets neighboring a pole piece are either both pushing flux into the pole piece or both pulling flux out of the pole piece. Consequently, the magnet arrangement and the symmetry of the alternator's geometry ensure that the magnetic flux lines never cross the line bisecting a pole piece.

[1]The STAR alternator. Clever Fellows Innovation Consortium, Inc. 302 Tenth Street, Troy, New York, 12180

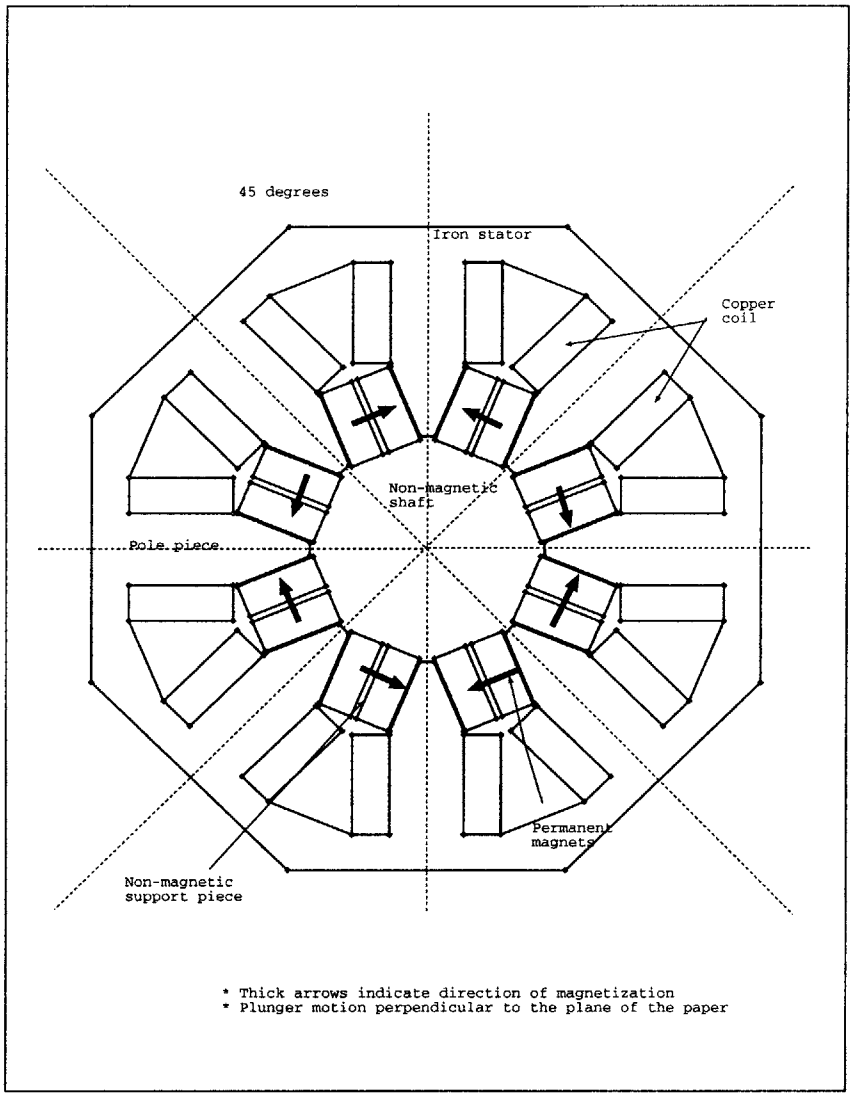

Figure 2-1: Alternator geometry in cross-section

Four flexure-springs are mounted on each end of the linear alternator. The flexure-springs connect the reciprocating shaft to the stator's back-iron. The purpose of this flexure suspension is to restrain the plunger's torsional-motion, thus preventing contact between the brittle permanent-magnets and the iron pole-pieces.

2.2 Modeling assumptions

The linear alternator behaves like a single-winding, single-magnet alternator despite its complicated geometry. Figure 2-3 illustrates a lumped-parameter model of the

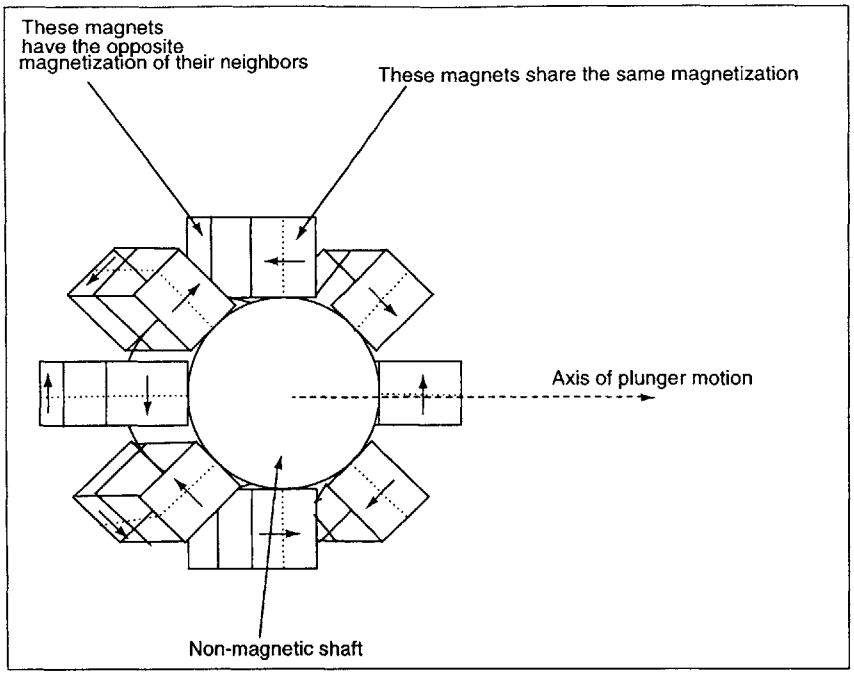

Figure 2-2: Axial view of the magnetic arms on the plunger

alternator consisting of a voltage source $e_{af}(t)$ in series with a resistance R_w and an inductance L_w. The internal voltage-source models the conversion of mechanical motion into an induced voltage, while the inductance and the resistance model energy storage and dissipation in the stator winding. Although this machine is clearly three-dimensional in nature, the expressions derived in this chapter rely on a simplified two-dimensional analysis. The appropriateness of these approximations and assumptions has been examined with finite-element methods as well as experimentally.

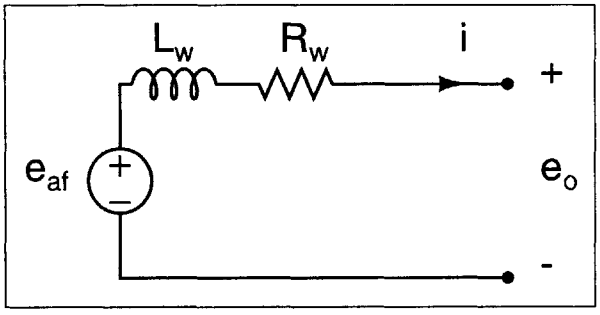

Figure 2-3: Equivalent lumped-parameter model of the alternator

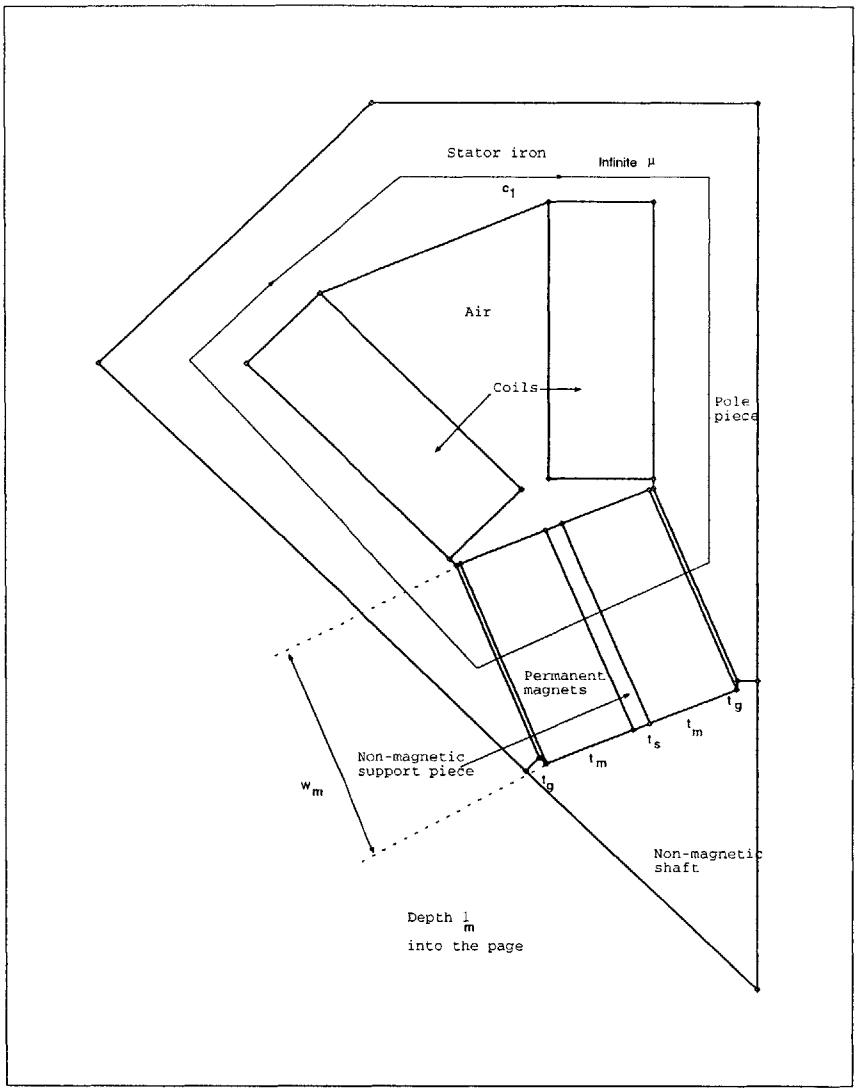

Figure 2-4: A 45° section of the alternator showing the contour of integration C_1

The field analysis relies on magnetic-circuit approximations, which hold when the permeability of the stator iron is much greater than the permeability of free space, and when the thickness of the air gap and magnets is small. Furthermore, the model ignores reluctance effects and assumes that the permeability of the permanent-magnet material equals the permeabilty of free space. Finally, expressions derived in this chapter exploit the alternator's symmetry by solving the fields in the 45° arc shown in Figure 2-4.

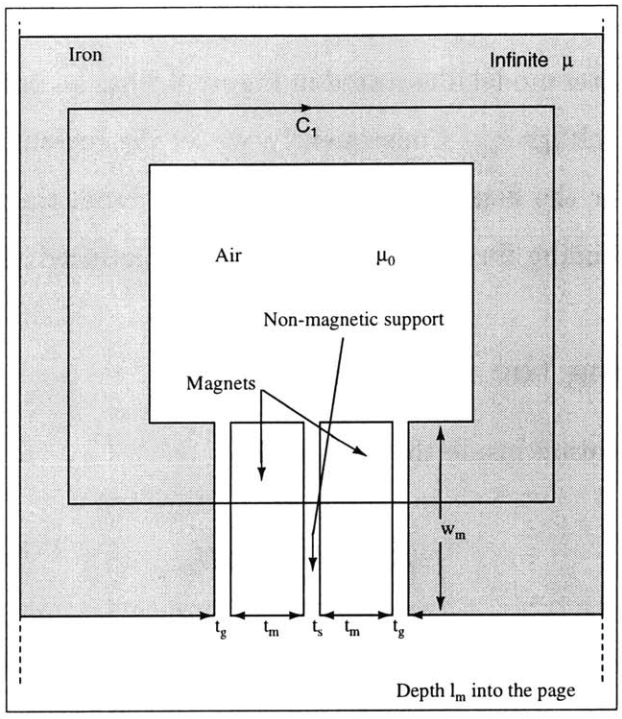

Figure 2-5: Equivalent magnetic circuit

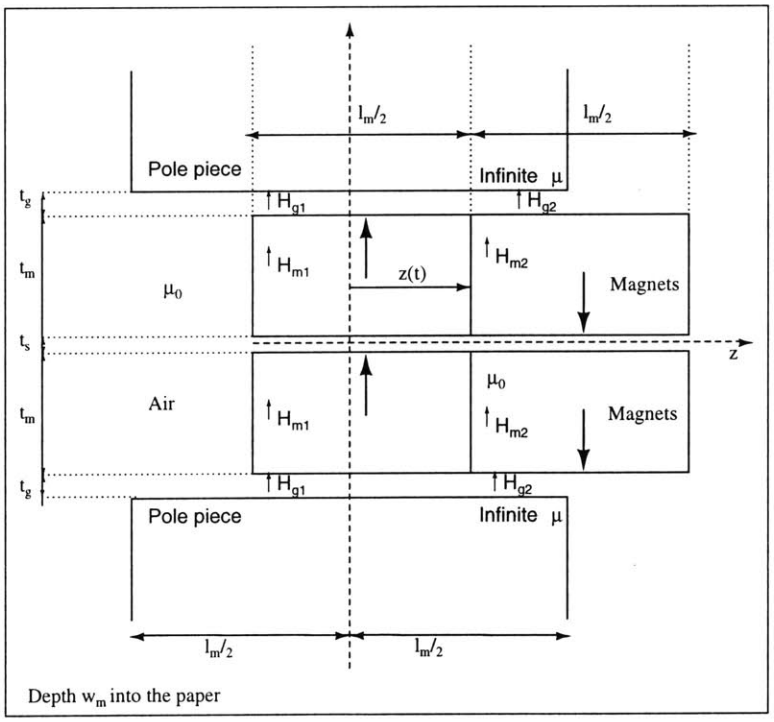

Figure 2-6: Radial view of the magnets displaced along the axis of reciprocation

2.3 Internal voltage

The lumped-parameter model illustrated in Figure 2-3 has an open circuit voltage that equals the internal voltage e_{af}. Consequently, we set the current through the windings to zero and solve for the fields due to the magnets. From the field distribution, we can calculate the winding flux-linkage and hence the induced voltage.

2.3.1 Modeling the internal voltage

The constitutive relation inside the magnet is,

$$B_m = B_r + \mu_r H_m \tag{2.1}$$

where B_m and H_m are the magnetic flux-density and field intensity inside the magnet, μ_r is the permeability of the magnetic material, and B_r is a constant residual flux-density. We ignore the reluctance of the magnetic material and set,

$$\mu_r = \mu_0 \tag{2.2}$$

This assumption holds since the permanent-magnet material used in the alternator under study has a relative permeability of 1.05. This means that the constitutive relation inside the magnet can be rewritten as,

$$B_m = B_r + \mu_0 H_m \tag{2.3}$$

The constitutive relation in the air gap and in the non-magnetic support is linear,

$$B_g = \mu_0 H_g \tag{2.4}$$

$$B_s = \mu_0 H_s \tag{2.5}$$

where the subscripts g and s denote field variables in the air gap and in the mounting support. The model ignores the fringing fields in the air gap and mounting support

and assumes that these fields are uniform.

The permeability of the iron is assumed to be infinite, which confines the flux lines in the iron and forces the magnetic-field intensity in the iron to zero. These assumptions reduce the 45° arc in Figure 2-4 to the magnetic circuit in Figure 2-5. Going around the contour C_1 in Figure 2-5 and taking the line integral of H yields,

$$2t_g H_g + t_s H_s + 2t_m H_m = 0 \tag{2.6}$$

where t_g is the thickness of the air gap, t_s is the thickness of the magnet mounting-support, and t_m is the thickness of the magnet. The section of the contour within the iron makes no contribution to the line integral because H in the iron is zero by assumption.

To conserve magnetic flux, the flux density in the air gap $\mu_0 H_g$ must equal the flux density in the mounting support $\mu_0 H_s$ because the area of the air gap is constant and the fields are uniform. This results in the equality,

$$H_g = H_s \tag{2.7}$$

which when combined with Equation 2.6 gives the expression,

$$(2t_g + t_s)H_g + 2t_m H_m = 0 \tag{2.8}$$

Conservation of magnetic flux also requires that the flux densities at the interface between the air-gap and the magnet be equal,

$$B_g = B_m \tag{2.9}$$

Using the constitutive relations 2.3 and 2.4 along with Equations 2.8 and 2.9 to solve the fields in the air-gap and in the magnet results in,

$$H_g = \frac{2t_m B_r}{\mu_0 (2t_m + 2t_g + t_s)} \tag{2.10}$$

$$H_m = \frac{-(2t_g + t_s)B_r}{\mu_0 (2t_m + 2t_g + t_s)} \tag{2.11}$$

Figure 2-6 shows a radial view of the section in Figure 2-4 with the magnets displaced along the axis of reciprocation. The figure shows two pairs of magnets of opposite polarity between the iron pole-pieces, where each magnet is half the stator length l_m. The total magnetic-flux through the air gap depends on the position of the magnets within the iron as the plunger travels along the axis of reciprocation. The net flux is zero when the magnet pair is completely centered within the stator pole-piece.

Neglecting fringing effects, the total flux crossing the air gap in Figure 2-6 can be calculated as,

$$\Phi_g = \mu_0 \left(H_{g1} \frac{l_m}{2} + H_{g2} \left(\frac{l_m}{2} - z(t) \right) \right) w_m \tag{2.12}$$

where H_{g1} and H_{g2} are the magnetic-field intensities in the regions of the air gap shown in Figure 2-6, $z(t)$ is the displacement of the magnets from the center of the pole pieces, and w_m is the width of a magnet pair. Recognizing that,

$$H_{g1} = -H_{g2} = H_g \tag{2.13}$$

and substituting the expression for H_g from Equation 2.10 into Equation 2.12, yields the net flux through the air gap as,

$$\Phi_g = \frac{2t_m B_r}{2t_m + 2t_g + t_s} w_m z(t) \tag{2.14}$$

This expression holds until only one of the magnets remains in the gap ($i.e, |z| < \frac{l_m}{2}$).

Since the arc of Figure 2-4 includes only one half of each pole piece, the total flux through each pole piece Φ_p must be twice Φ_g,

$$\Phi_p = \frac{4t_m B_r}{2t_m + 2t_g + t_s} w_m z(t) \tag{2.15}$$

Table 2.1: Values of the alternator's geometric-parameters

t_g	0.50 mm
t_s	2.16 mm
l_m	25.40 mm
t_m	11.25 mm
w_m	27.94 mm
B_r	1.25 T
μ_0	$4\pi \times 10^{-7}$ $\frac{H}{m}$

The flux linkage λ for an N-turn coil wound around a pole piece is,

$$\lambda = \frac{4t_m B_r N}{2t_m + 2t_g + t_s} w_m z(t) \tag{2.16}$$

Taking the time derivative of Equation 2.16 gives the voltage induced across each N-turn coil,

$$e_c = \frac{4Nt_m w_m B_r}{2t_m + 2t_g + t_s} \frac{dz}{dt} \tag{2.17}$$

The alternator armature winding consists of eight such coils connected in series. Hence the generated voltage is given by,

$$e_{af} = 8e_c = G\frac{dz}{dt} \tag{2.18}$$

where,

$$G = \frac{32Nt_m w_m B_r}{2t_m + 2t_g + t_s} \tag{2.19}$$

Table 2.1 lists the dimensions of the alternator used in the prototype. These values lead to $G = 30.87$ $\frac{kg \cdot m}{Coul \cdot s}$.

2.3.2 Finite-element analysis

The model derived in Section 2.3.1 is based on a simple magnetic-circuit representation which neglects three-dimensional effects. In particular, the model assumes that

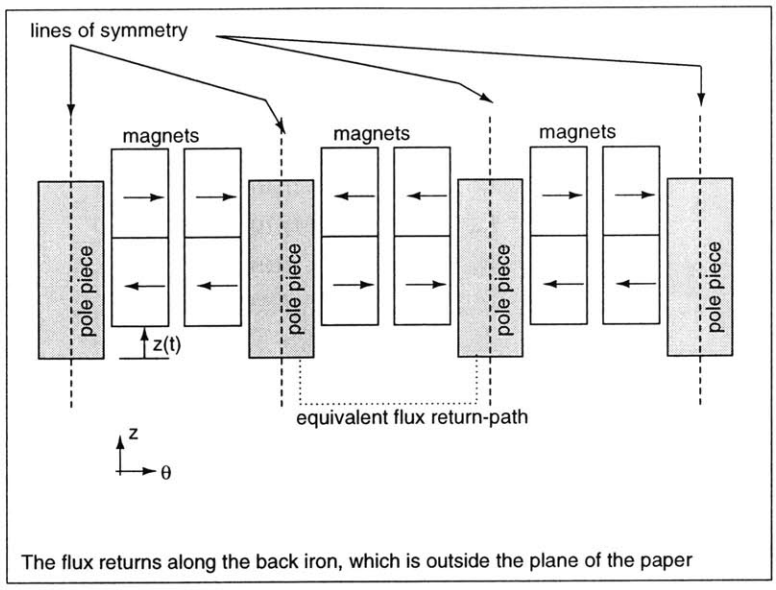

Figure 2-7: Developed radial view of the alternator

the fields are confined to the plane of Figure 2-1, thus ignoring any axial leakage fields. Although it is reasonable to expect the model of Section 2.3.1 to be an adequate representation of the linear alternator, it is necessary to investigate some of the modeling assumptions in detail.

Therefore, a two-dimensional finite-element analysis program[2] was employed to investigate axial permanent-magnet leakage-flux. The geometry of Figure 2-7 was chosen to perform this analysis. The geometry corresponds to a cylindrical cut through the alternator at the mid-point radius of of the magnets which is then laid out flat. In this figure, the plunger is shown displaced by a distance z from its rest position when it is centered in the stator pole-pieces.

Note first of all that this developed radial view of the machine is periodic. If one draws lines of symmetry through the stator pole-pieces as is done in Figure 2-7, the symmetry of the machine requires that no magnetic flux cross these lines. Hence, for the purposes of a finite-element analysis it is sufficient to investigate a single section including one magnet set between two lines of symmetry (referred to as a solution region in Figure 2-7). This can be readily done in a finite-element program. Setting a boundary condition of zero vector potential on the two symmetry lines will

[2]QuickField. Tera Analysis, 17114 Birchner Street, Granada Hills, CA 91344

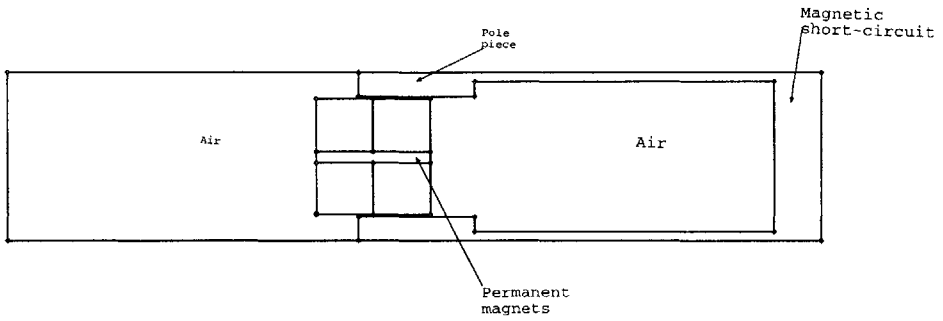

Figure 2-8: Finite-element geometry used to investigate axial leakage fluxes

guarantee that no flux will cross them, consistent with the symmetry imposed by the conditions of the actual machine. To perform the finite element analysis, the boundary surrounding the solution region must be closed. The rectangular solution-region illustrated in Figure 2-8 is formed by adding two boundary segments which are also set to zero vector potential. This is reasonable since only the fields near the air gap are of interest.

It is also important to note that the three-dimensional nature of the machine requires that the geometry of Figure 2-7 be somewhat modified to enable a two-dimensional solution. The problem is that, although the flux produced by the magnets is directed predominantly in the plane of the figure, the flux going through the pole pieces flows out of the plane of the paper and returns through the stator back-iron which is not included in the two dimensional section under study.

Because the analysis is primarily interested in the leakage flux which flows in the plane of Figure 2-7, an approximate representation will be investigated in which an equivalent flux return-path will be included in the plane of the figure. The resultant

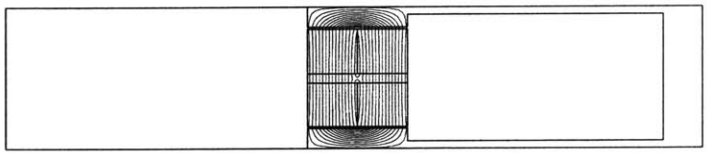

Figure 2-9: Finite element solution of the axial leakage-fields, $z = 0$ mm

geometry shown in Figure 2-8 provides a flux return-path in the plane of the solution region. Note the presence of a magnetic short-circuit between the two pole-pieces as well as the zero potential boundary that surrounds the solution region. Because the short-circuit is far away from the region where leakage fluxes are expected, it is reasonable to expect that the presence of short-circuit will not affect the solution (certainly to the extent that this two-dimensional solution can be considered to approximate the full three dimensional situation).

Figures 2-9 to 2-11 present the finite element solution for zero displacement, a displacement of $z = 6.7$ mm, and a displacement of $z = 13.4$ mm. With the magnets centered within the stator iron (Figure 2-9), the finite element solution indicates that no net flux is going through the flux return-path, which is in agreement with the magnetic-circuit model of Section 2.3.1. However, note that when a portion of the permanent-magnet plunger is out (as in Figures 2-10 and 2-11) only some of the flux lines crossing the air gap return through the equivalent short-circuit and link the armature coil. This finite element investigation shows that there are significant, unmodeled axial leakage-fluxes when the plunger is displaced outside the stator iron.

To appreciate the extent to which the model of Section 2.3.1 needs refinement,

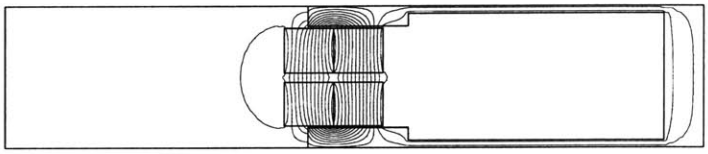

Figure 2-10: Finite element solution of the axial leakage-fields, $z = 6.7\ mm$

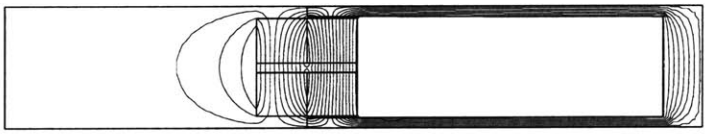

Figure 2-11: Finite element solution of the axial leakage fields, $z = 13.4\ mm$

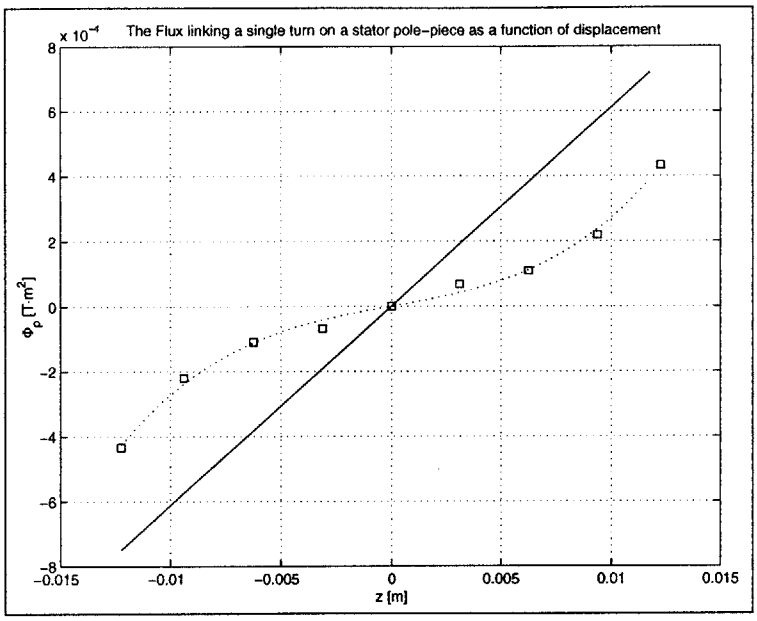

Figure 2-12: The flux linking an armature coil: analytical-model predictions (solid) and finite element results (squares)

we examine the effect these leakage phenomena have on the induced internal-voltage. Figure 2-12 compares the the finite-element results for the flux through a pole piece with the predictions of Equation 2.15. The symmetry of the alternator was used to produce the values for negative displacements. Note that the finite-element results are not linear, in contrast with the predictions of Equation 2.15 from Section 2.3.1. Because the flux is an odd function of displacement, a cubic best-fit through the finite-element results shown in Figure 2-12 was chosen to represent the data. The best fit curve is given by,

$$\Phi_p = q_3 z^3 + q_1 z \tag{2.20}$$

where $q_3 = 152.8$, and $q_1 = 0.0118$. The lack of qualitative as well as quantitative agreement between the results of Section 2.3.1 and this finite-element analysis makes it very hard to justify the assumption that axial leakage fluxes are negligible.

Although it would be interesting to return to analytical considerations of Section 2.3.1 and refine the modeling assumptions in the light of the evidence from the finite-element analysis, the numerical fit of the finite-element results as given by Equation 2.20 is sufficient for the purposes of this thesis. Incorporating this refinement to

the model of Section 2.3.1 changes the flux linkage for an N-turn coil λ predicted in Equation 2.16 to,

$$\lambda = Nq_3z^3 + Nq_1z \tag{2.21}$$

This leads to the induced voltage across each N-turn coil given by the expression,

$$e_c = 3Nq_3z^2(t)\frac{dz(t)}{dt} + Nq_1\frac{dz(t)}{dt} \tag{2.22}$$

which in turn leads to the winding-voltage expression,

$$e_{af} = 24Nq_3z^2(t)\frac{dz(t)}{dt} + 8Nq_1\frac{dz(t)}{dt} \tag{2.23}$$

which is non-linear in contrast with Equation 2.18 from Section 2.3.1.

2.4 Magnetic axial restoring-forces

The magnetic plunger resists being pulled away from its rest position in the center of the iron-stator structure. A displacement of the plunger from the center of the stator results in a force that acts to restore the plunger to the center. This section uses the field solution of Equations 2.10 and 2.11 and the assumptions associated with them to derive an expression for the alternator co-energy U' as a function of the displacement z. The restoring force can then be calculted by taking the derivative of U' with respect to z.

In this section, the fringing fields in the air and the portion of the magnetic plunger displaced outside the stator iron are assumed to be negligible. Only the region where the permanent magnet overlaps with the stator iron is assumed to have a significant concentration of magnetic flux-lines (see Figure 2-6). In addition, all of the fields of interest are assumed to be uniform.

These assumptions are consistant with magnetic circuit approximations, which hold when the permeability of the stator iron is much greater than the permeability of free space, and the thickness of the air gap and magnet is small. Section 2.4.2

examines the appropriatness of these assumptions against the predictions of a finite-element analysis.

2.4.1 Modeling the magnetic axial restoring-forces

Figure 2-6 shows a radial view of the displaced magnets. If the displacement is positive $z > 0$, then the co-energy stored in the air gap and magnet support structure $U_g^{'}$ is given by the integral of co-energy density over the overlap volume,

$$U_g^{'} = w_m(l_m - z)(2t_g + t_s)u_g^{'} \tag{2.24}$$

where $u_g^{'}$ is the co-energy density in the air gap and magnet support structure in the region where the magnets overlap the stator iron in Figure 2-6. Note that the air-gap fields H_{g1} and H_{g2} shown in Figure 2-6 have the same co-energy density since they are of equal magnitude and opposite direction.

$$H_{g1} = -H_{g2} = H_g \tag{2.25}$$

The co-energy density is given by,

$$u_g^{'} = \frac{1}{2}\mu_0 H_g^2 \tag{2.26}$$

This leads to,

$$U_g^{'} = w_m(l_m - z)(2t_g + t_s)\frac{1}{2}\mu_0 H_g^2 \tag{2.27}$$

Substitution of the field solution from Equation 2.10 into Equation 2.27 yields,

$$U_g^{'} = w_m(l_m - z)(2t_g + t_s)\frac{B_r^2 t_m^2}{2\mu_0(2t_g + ts + 2t_m)^2} \tag{2.28}$$

The co-energy density in the permanent-magnet material[3],

$$u_m^{'} = \frac{1}{2}\mu_0 H_m^2 + B_r|H_m| + \frac{1}{2}\frac{B_r^2}{\mu_0} \tag{2.29}$$

Since the fields in the magnetic material are of equal magnitude H_m and opposite direction, the co-energy density in Equation 2.29 holds for the magnetic material in the region of overlap between the permanent-magnet and the stator iron.

The co-energy stored in the magnetic material is calculated by multiplying the co-energy density by the volume of permanent magnet in the overlap region,

$$U_m^{'} = 2t_m w_m (l_m - z) u_m^{'} \tag{2.30}$$

Using the co-energy density from Equation 2.29 to rewrite Equation 2.30 gives,

$$U_m^{'} = 2t_m w_m (l_m - z)(\frac{1}{2}\mu_0 H_m^2 + B_r H_m + \frac{1}{2}\frac{B_r^2}{\mu_0}) \tag{2.31}$$

Substitution of the field solution from Equation 2.11 into Equation 2.31 followed by some algebraic manipulation yields,

$$U_m^{'} = w_m (l_m - z)\frac{B_r^2 (2t_m)^3}{2\mu_0 (2t_g + t_s + 2t_m)^2} \tag{2.32}$$

The total co-energy $U^{'}$ is the sum of $U_m^{'}$ and $U_g^{'}$ from Equations 2.28 and 2.32,

$$U^{'} = U_g^{'} + U_m^{'} = w_m (l_m - z)\frac{B_r^2 (2t_m)^2}{2\mu_0 (2t_g + t_s + 2t_m)} \tag{2.33}$$

The derivative of $U^{'}$ with respect to z gives the force as,

$$f_{ms} = \frac{dU^{'}}{dz} = -w_m \frac{B_r^2 (2t_m)^2}{2\mu_0 (2t_g + t_s + 2t_m)} \tag{2.34}$$

for $z > 0$.

[3]Fitzgerald, A., E., Kingsley, C. Jr., Umans, S., D., Electric Machinery

A similar consideration for $z < 0$ leads to the force,

$$f_{ms} = w_m \frac{B_r^2 (2t_m)^2}{2\mu_0 (2t_g + t_s + 2t_m)} \tag{2.35}$$

Because of the eightfold symmetry of the alternator, the net restoring-force f_m has the magnitude,

$$|f_m| = 8|f_{ms}| \tag{2.36}$$

According to this model the magnetic restoring-force is a non-linear function of position; whenever the magnetic assembly is displaced to either side, a force of constant magnitude acts to oppose that displacement. The force on the magnetic assembly is zero only when the magnets are completely centered in the stator iron. Using the values in Table 2.1 gives a force f_m of magnitude 2738 N.

2.4.2 Finite-element analysis

This section utilizes the finite-element solution of section 2.3.2 to examine the axial magnetic restoring-force. It is clear that axial fringing-fields and the three-dimensional nature of the machine are far from negligible. The finite-element solutions in Figures 2-10 and 2-11 show that, contrary to the modeling assumptions, a considerable amount of co-energy is stored in the fringing fields. This indicates that the results of the simple two-dimensional consideration of Section 2.4.1 are likely to be inaccurate.

An experiment in which the restoring force due to the magnet and the mechanical flexure-springs are measured (see Figure 2-13) confirms that the modeling assumptions are inappropriate. Not only is the magnitude of force calculated in the previous section much higher than the experimental data, the measurements indicate that the magnet force is a relatively linear function of displacement in contrast to the constant restoring-force derived in Section 2.4.1. Thus it is clear that the fringing fields in the air and in the portion of the magnetic plunger displaced outside the stator iron cannot be ignored.

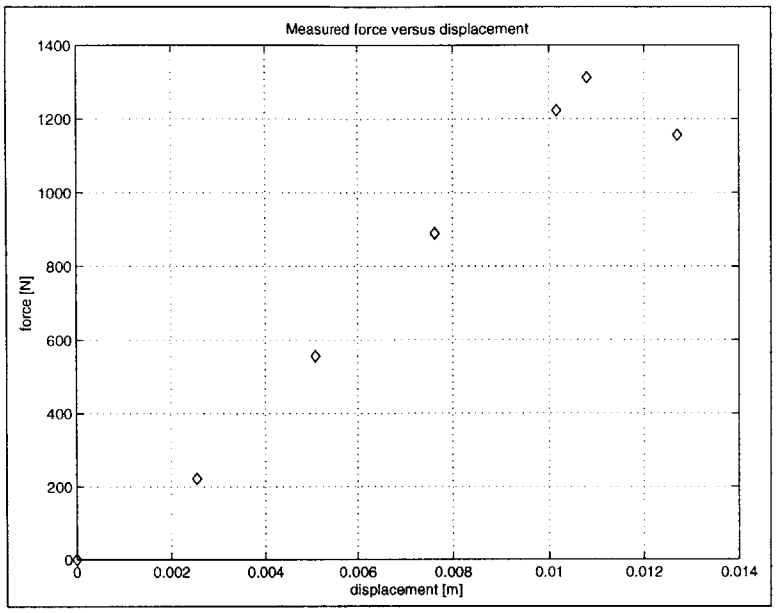

Figure 2-13: Force-displacement experimental measurements

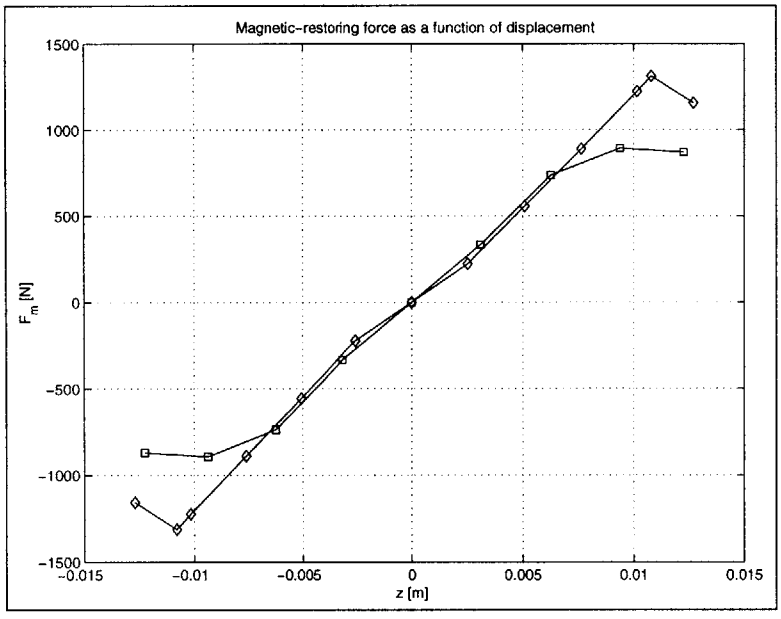

Figure 2-14: Force-displacement profile: experimental measurements (diamonds) and finite element results (squares)

Presented in Figure 2-14 is a comparison between the experimental measurements (diamonds) and the finite-element force calculations for five plunger displacements (squares). The symmetry of the alternator was used to infer the values for negative displacements. The results of the finite-element analysis are in good agreement with experimental data; both indicate that over a wide range of displacements the restoring force is a linear function of the displacement with a proportionality constant $K = 9.52 \times 10^4 \frac{N}{m}$. The results suggest that it is reasonable to model the magnetic axial restoring-force as simple spring,

$$f_m = Kz \tag{2.37}$$

Note that the finite-element force-displacement results "saturate" at a lower force than the experimental data. This disagreement in "saturation level" can be attributed to the approximate nature of the chosen finite-element geometry (a developed cylindrical-cut at the average radius of a magnet). The simple spring-model of the magnetic restoring-force presented in Equation 2.37 ignores this saturation effect, which should not have a big impact on the dynamics of the engine/alternator/load system, because the saturation occurs near the limits of plunger displacement.

Note also that these results imply that the flexure springs do not appear to exert much force in the axial direction. The flexure springs are mounted on the plunger to constrain the torsional motion of the plunger and thus prevent the plunger's permanent-magnets from coming into disastrous contact with the stator's pole-pieces.

2.5 Winding inductance

To calculate the winding inductance, we utilize the principle of superposition by "turning off" the magnets (i.e., setting $B_r = 0$) and then calculating the flux linkage due to current flow in the windings.

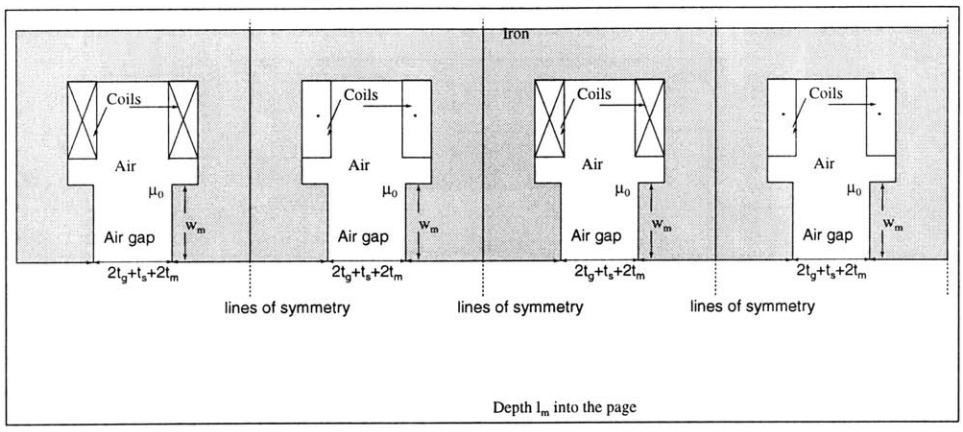

Figure 2-15: Developed view of the stator

2.5.1 Modeling the winding inductance

Magnetic-circuit approximations allow us to develop the cross-section of the linear alternator into the series of identical magnetic-circuits shown in Figure 2-15. Note that due to the symmetry of the machine, no magnetic flux can cross the symmetry lines drawn through the stator pole-pieces in Figure 2-15. Hence, it suffices to consider the fields in only one section including the $2Ni$ Amp·turns and bounded by two symmetry-lines as shown in Figure 2-16.

The contour C_2 in Figure 2-16 encloses $2Ni$ Ampere-turns and goes across a uniform air-gap of thickness $2t_m + 2t_g + t_s$. This leads to the solution,

$$B_g = \frac{2\mu_0 Ni}{2t_m + 2t_g + t_s} \tag{2.38}$$

where the magnetic-field intensity in the infinitely-permeable stator iron is assumed to be zero.

Assuming that the air gap is small enough for the fields to be uniform, the product of the of flux density B_g and the area of the air gap $w_m l_m$ yields the total flux through the air gap,

$$\Phi_g = \frac{2\mu_0 Ni}{2t_m + 2t_g + t_s} w_m l_m \tag{2.39}$$

which gives the flux through only one half of each pole piece. The flux through a pole

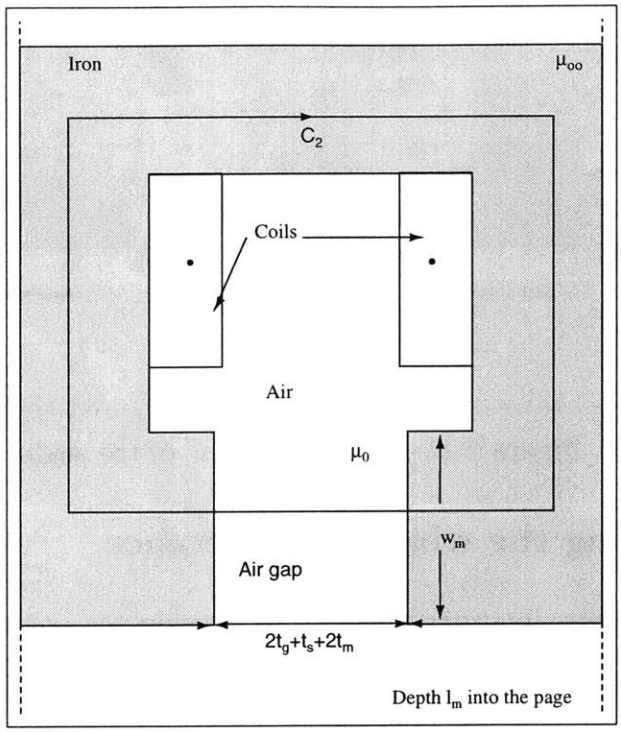

Figure 2-16: A section of the developed view of the stator

piece Φ_p is twice the value of Φ_g,

$$\Phi_p = \frac{4\mu_0 Ni}{2t_m + 2t_g + t_s} w_m l_m \tag{2.40}$$

The flux linked to an N-turn coil wound around a pole piece is given by,

$$\lambda = \frac{4N^2 \mu_0 w_m l_m}{2t_m + 2t_g + t_s} i \tag{2.41}$$

And since,

$$\lambda = Li \tag{2.42}$$

the inductance of one N-turn coil is given by,

$$L = \frac{4N^2 \mu_0 w_m l_m}{2t_m + 2t_g + t_s} \tag{2.43}$$

The winding inductance is eight times the expression in Equation 2.43,

$$L_w = \frac{32N^2\mu_0 w_m l_m}{2t_m + 2t_g + t_s} \tag{2.44}$$

Using the values from Table 2.1 yields $L_w = 4.41\ mH$.

These calculations are based on the assumption that $2t_m + 2t_g + t_s$ is small and ignore any flux linked by fringing fields. However the thickness of the air gap and magnets is not small and a finite-element solution can be used to examine the effect of fringing fields on the winding inductance.

2.5.2 Finite-element analysis

QuickField finite-element software was used to investigate some of the assumptions and approximations used to derive the inductance expression of Equation 2.44. In particular, this investigation focused on the magnetic-circuit approximations (i.e., infinitely-permeable iron, and uniform magnetic-fields with negligible fringing) by solving for the flux distribution in a cross section of the alternator. The analysis did not include three-dimensional effects like axial leakage-fluxes. It is reasonable to expect that some flux will leak axially from the ends of the alternator. Since this implies that some of the fields (and consequently the co-energy) in the alternator will remain unaccounted for, the inductance of the winding is likely to be slightly higher than the value calculated in this section.

The finite-element analysis determined the two-dimensional fields excited by a current i flowing in the stator winding in the geometry of Figure 2-17. To determine the inductance, the magnets are "turned off" by setting $B_r = 0$ and are assumed to have a permeability of $\mu_r = 1.05\mu_0$. Because it was not possible to identify the electrical steel used in the alternator, the constitutive relation for the stator iron is modeled by a non-linear B-H curve for a generic electrical-steel (see Figure 2-18).

In addition, it is reasonable to expect no flux leakage out of the alternator at its outer radius. Consequently, the vector potential at the outer circumference of the alternator was set to zero.

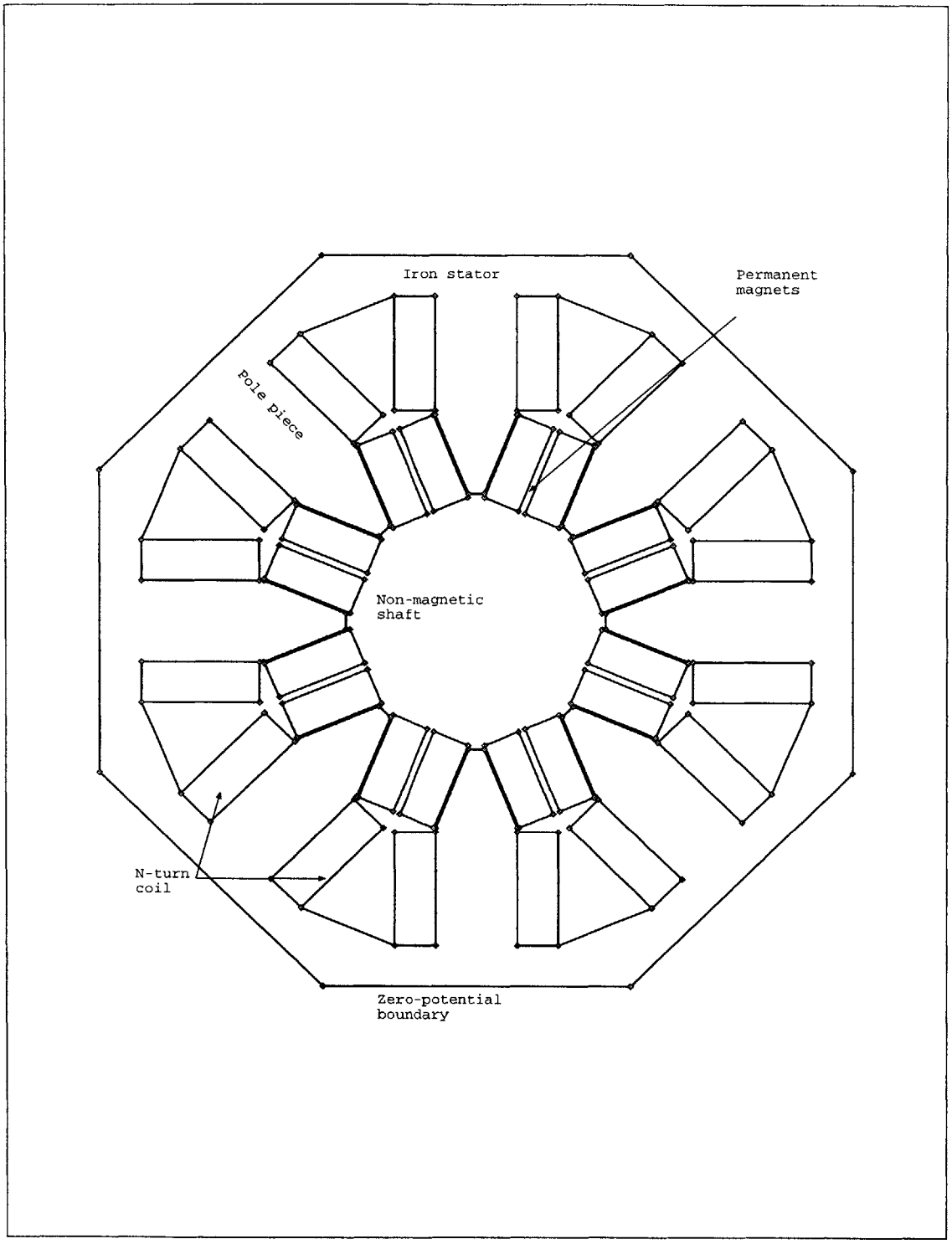

Figure 2-17: Finite element geometry used to investigate the winding inductance

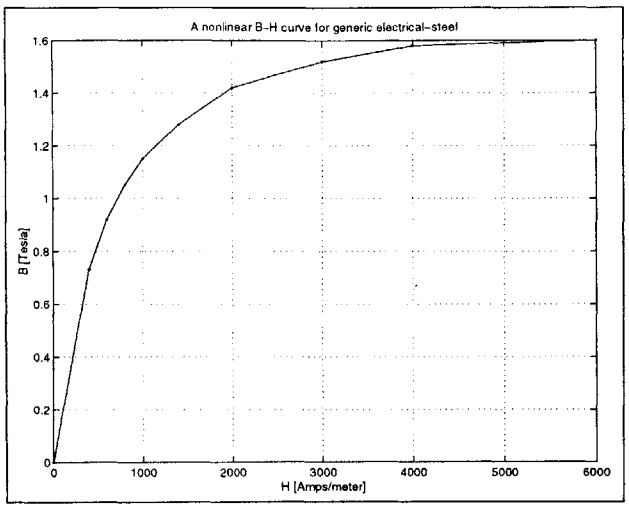

Figure 2-18: Non-linear B-H curve for generic electrical-steel

An operating point of $i = 10$ Amps was selected for the purposes of this analysis, since the alternator is expected to operate near that current level. Figure 2-19 shows the field distribution resulting from the finite-element solution. The field distribution reveals a significant amount of leakage flux, indicating that the thickness of the air gap and magnets is not small enough to justify magnetic circuit approximations.

The software calculates the magnetic field co-energy in the stator, which can then be used to calculate the inductance of the winding by using the expression,

$$\frac{1}{2}L_w i^2 = U' \tag{2.45}$$

where U' is the total magnetic co-energy stored in the alternator. Solving Equation 2.45 for L_w gives the expression,

$$L_w = \frac{2U'}{i^2} \tag{2.46}$$

The finite-element solution in Figure 2-19 shows that the total magnetic energy stored in the system due to a winding current of 10 Amps is 0.359 J. The magnetic co-energy is also equal to 0.359 J, which indicates that the stator iron has not saturated and is still in the linear regime. Substitution of $i = 10$ Amps and $U' = 0.395$ J into Equation 2.46 results in $L_w = 7.19$ mH, which is 63% larger than the value

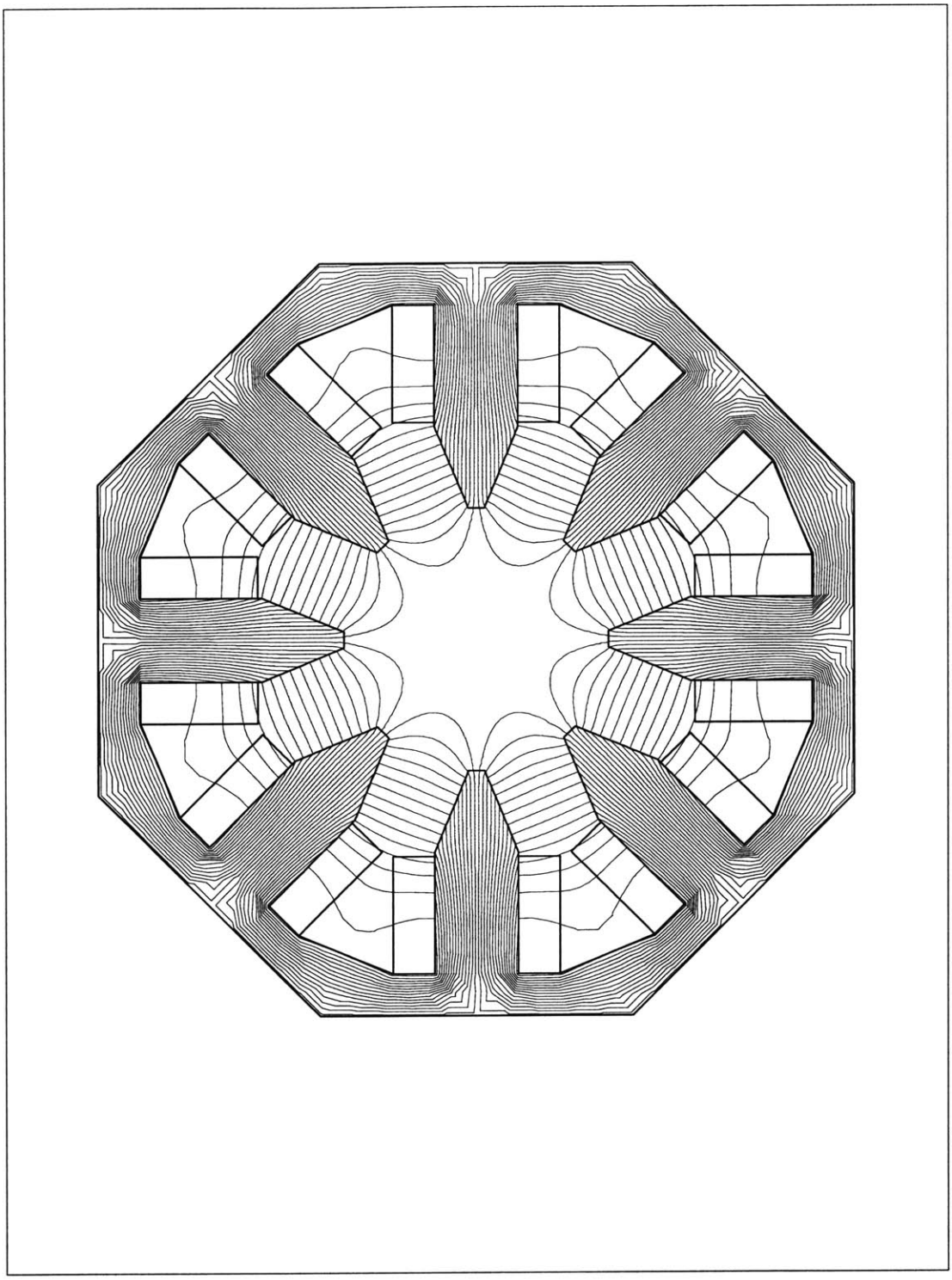

Figure 2-19: Finite element solution of fields due to 10 Amps of winding current with the magnets "turned off"

predicted by the model of section 2.5.1. This excess is due to the unmodeled leakage-flux generated by the current and linking the coils. The finite-element analysis shows that 40% of the co-energy of the system is in the fringing fields. Which according to Equation 2.46 indicates that ignoring the co-energy in the fringing fields leads to a 60% error in the inductance.

The derivation of Section 2.5.1 assumes the permeability of the stator iron is much higher than that of air (i.e., the reluctance of the iron is small relative to the reluctance of the air gap). In order to verify that the stator iron is not saturated at the alternator's operating flux density level, a finite element analysis was conducted on the geometry of Figure 2-17 with the magnets "turned on" and a winding current of 10 Amps. Note that this analysis considers only the highest possible flux-density level corresponding to the displacement where only one magnetic polarity remains in the stator iron. Furthermore, this analysis does not take into account the axial leakage-fluxes, which proved to be significant in Section 2.3.2.

The finite-element solution presented in Figure 2-20 shows that the flux density in the iron ranges from a maximum of 1.8 T to a minimum of 0.8 T which causes the permeability of the iron to range from 35 to 2000 times the permeability of air. In addition, the finite-element solution shows that going around a single flux-loop the magneto-motive force drop in the iron is on average 15% of the drop across the air gap. This indicates that the reluctance of the iron is 15% of that of the air gap, which in turn implies a 15% error in the inductance. Keeping in mind that these findings correspond to the highest flux-density levels possible and that they ignore axial leakage-flux, there is good evidence that the assumption of infinitely-permeable iron holds reasonably well at the expected regime of operation.

2.6 Force of electrical origin

The electrical power at the terminals of the alternator model shown in Figure 2-3 can be written as,

$$ie_o = -i^2 R_w - \frac{d}{dt}\left(\frac{1}{2} L_w i^2\right) + ie_{af} \tag{2.47}$$

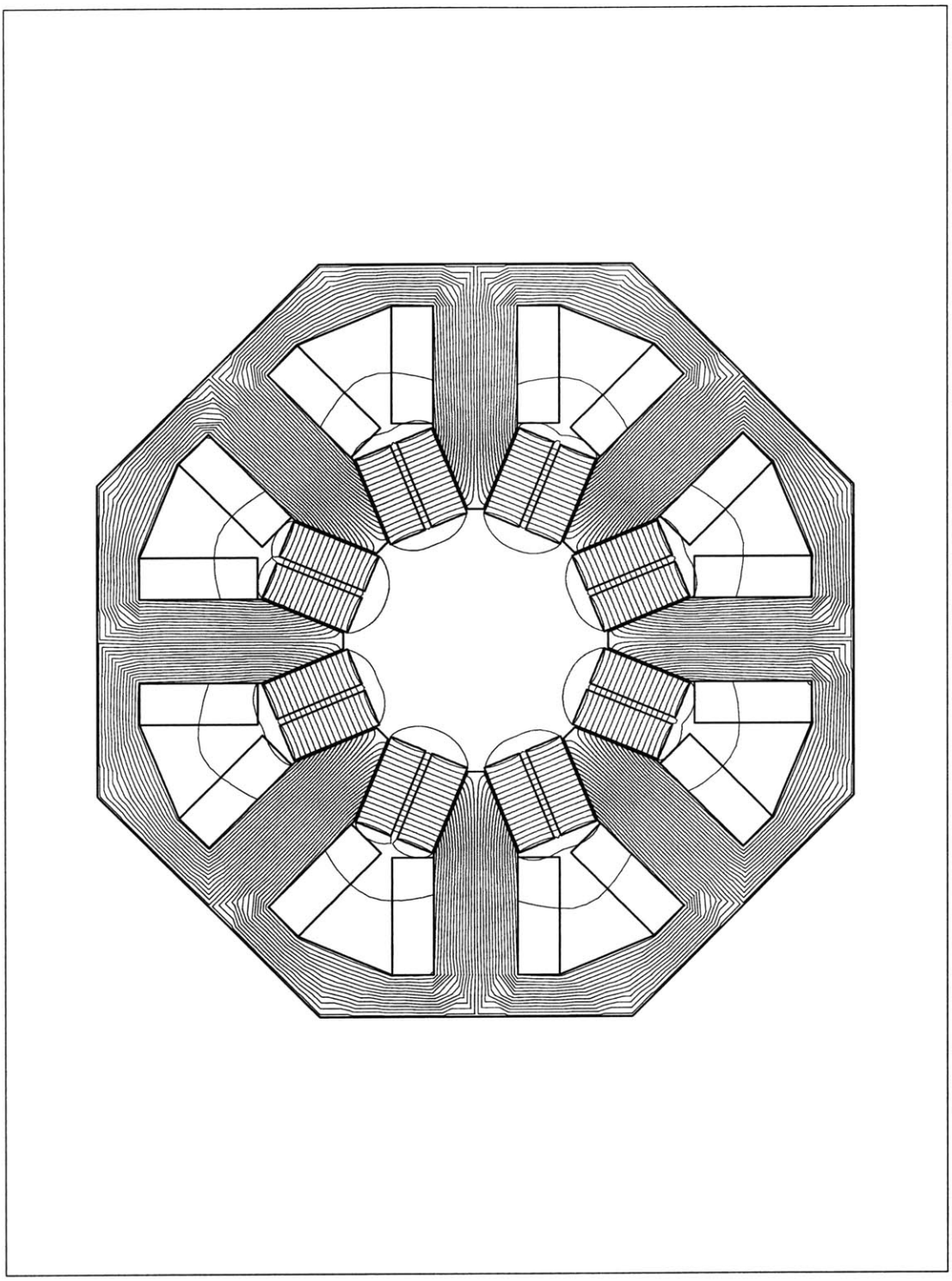

Figure 2-20: Finite element solution of fields due to 10 Amps of current and the permanent magnets

where e_o is the alternator's terminal voltage. We recognize $i^2 R_w$ as the instantaneous power dissipated in the winding, $\frac{d}{dt}\left(\frac{1}{2}L_w i^2\right)$ as the rate of change of energy stored in the winding, and ie_{af} as the converted mechanical power.

The converted mechanical power can also be expressed as the product of the force of electrical origin f_e and the velocity of the plunger $\frac{dz}{dt}$, which leads to,

$$f_e \frac{dz}{dt} = ie_{af} \tag{2.48}$$

Using the expression for the internal voltage in Equation 2.23, the force f_e is given by the expression,

$$f_e = 24Nq_3 z^2(t)i + 8Nq_1 i \tag{2.49}$$

2.7 Summary

The lumped parameter model for the alternator illustrated in Figure 2-3 has the electrical terminal relation,

$$e_o = -R_w i - L_w \frac{di}{dt} + e_{af} \tag{2.50}$$

The winding inductance in mH is,

$$L_w = 7.19 \tag{2.51}$$

and the internal voltage e_{af} is,

$$e_{af} = 24Nq_3 z^2(t)\frac{dz(t)}{dt} + 8Nq_1 \frac{dz(t)}{dt} \tag{2.52}$$

as determined by the finite-element analysis. The force of electrical origin is a function of current and position,

$$f_e = 24Nq_3 z^2(t)i + 8Nq_1 i \tag{2.53}$$

The magnetic restoring force is given by,

$$f_m = Kz \tag{2.54}$$

where $K = 9.52 \times 10^4 \ \frac{N}{m}$.

Chapter 3

Modeling the two stroke engine

The engine consists of two identical internal combustion cylinders and two pistons joined by a rigid rod. The cylinders fire so that the expansion following a combustion event in one cylinder drives the compression of the new charge in the opposite cylinder. The thermodynamic cycle in each cylinder is modeled as a standard Otto cycle[1] with instantaneous combustion and exhaust events (i.e., constant-volume heat addition/rejection). The difference in pressure between the two cylinders is used to calculate the force on the reciprocating assembly (the pistons, plunger and link-rod) as a function of position.

3.1 Engine geometry

Figure 3-1 documents the geometry of a cylinder, and Figure 3-2 shows the geometric relationship between the displacement z_p and the volumes of the left and right cylinders. The displacement z_p is referenced from half the crash-to-crash distance (the distance the reciprocating assembly moves between the position where the right piston contacts the right cylinder-head and the position where the left piston contacts the left cylinder-head). Figure 3-2 shows that the displacement z_p is related to the distance measured from each cylinder head to its corresponding piston's face by the

[1]Engineering Thermodynamics. Cravalho, E. G., Smith, J. L.

following expressions,

$$y_l = \frac{1}{2} y_{cc} + z_p \tag{3.1}$$

$$y_r = \frac{1}{2} y_{cc} - z_p \tag{3.2}$$

where y_l is the distance from the left cylinder head to the left piston's face, y_r is the distance from the right cylinder head to the right piston's face, and y_{cc} is the crash-to-crash distance.

These constraints make the volumes of the left and right pockets,

$$V_l = A(\frac{1}{2} y_{cc} + z_p) + V_{dead} \tag{3.3}$$

$$V_r = A(\frac{1}{2} y_{cc} - z_p) + V_{dead} \tag{3.4}$$

where A is the cross-sectional area of a cylinder and V_{dead} is the volume of the spark-plug cavity. Table 3.1 documents the details of the piston's geometry.

The engine/alternator configuration under consideration is constructed so that,

$$z = z_p \tag{3.5}$$

where z is the displacement of the magnetic plunger from the center of the stator iron. This means that when $z = 0$ the magnets are centered in the stator and the left and right gas pockets have the same volume $V = \frac{1}{2} A y_{cc} + V_{dead}$.

3.2 Overview of the cycle

Figure 3-3 illustrates the proposed thermodynamic cycle for a gas pocket in one of the cylinders. The cycle consists of six segments: intake, compression, combustion, expansion, heat-rejection and exhaust.

Segment $S_{0\to1}$ designates the intake of a fresh charge of premixed air and fuel. The exhaust port remains open throughout this segment and consequently the pressure

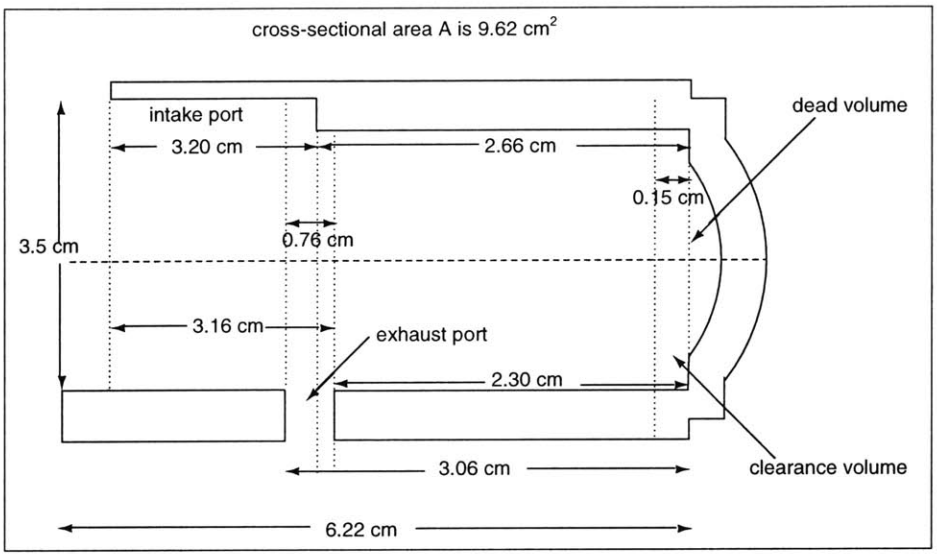

Figure 3-1: Geometry of the cylinder

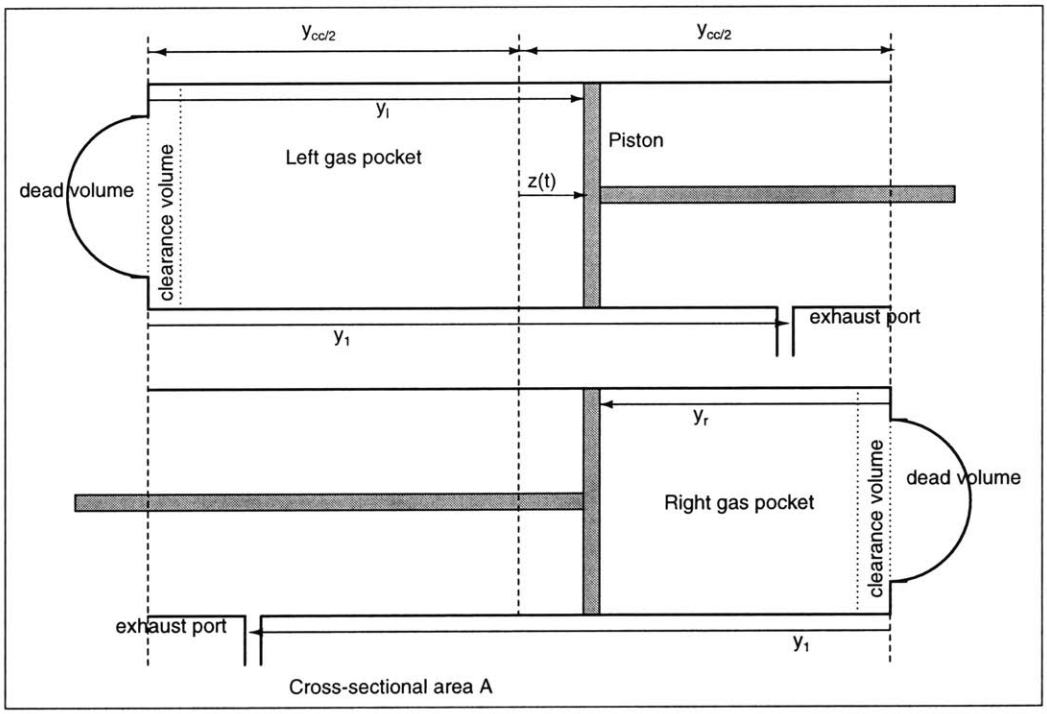

Figure 3-2: Schematic of the engine showing the relationship between left and right-cylinder volumes and the displacement z

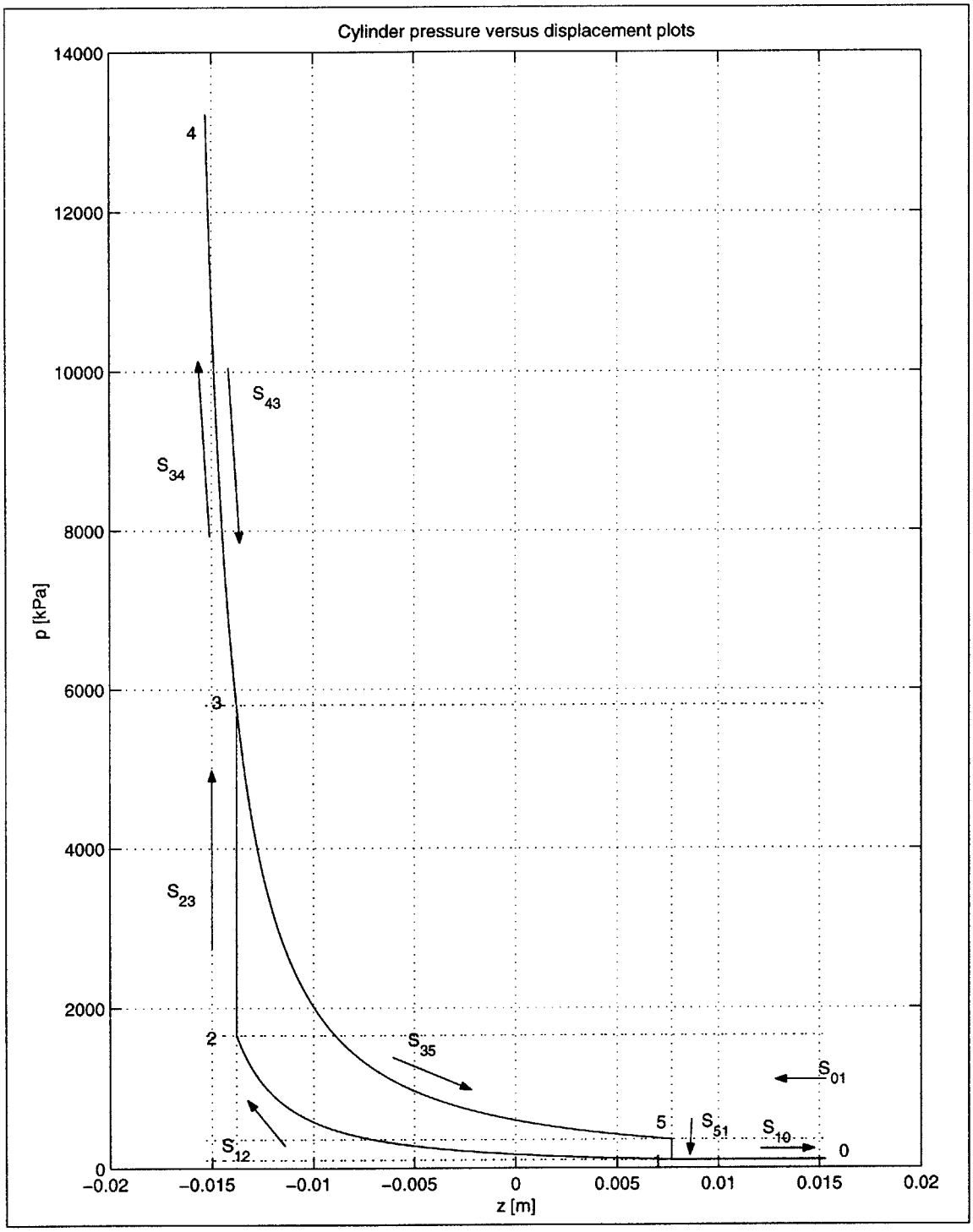

Figure 3-3: Standard Otto cycle

Table 3.1: Values of the engine's geometric parameters

γ	Unitless property of the gas	1.40
z_{1r}	Right cylinder exhaust-port	7.70 mm
z_{1l}	Left cylinder exhaust-port	-7.70 mm
$max[z_{2r}]$	Right cylinder maximum firing position	-13.80 mm
$max[z_{2l}]$	Left cylinder maximum firing position	13.80 mm
y_{cc}	Crash-to-crash distance	30.60 mm
A	Cross-sectional area of a cylinder	9.62 cm^2
V_1	Maximum volume of compressed pocket	23.93 cm^3
V_c	Clearance volume	1.44 cm^3
$min[V_2]$	Minimum combustion volume	3.24 cm^3
V_{dead}	Volume of spark-plug cavity	1.80 cm^3

in the cylinder remains atmospheric as the volume of the gas pocket decreases from V_0 to V_1. When the exhaust port closes, the gas in the cylinder undergoes reversible, adiabatic compression from an initial volume V_1 to a minimum volume V_2 along the segment labeled $S_{1\to 2}$.

The combustion event is assumed to take place instantaneously at a certain volume $V = V_2$ and is represented as $S_{2\to 3}$.

Segments $S_{3\to 4}$ and $S_{4\to 3}$ represent the overshoot following combustion. This overshoot occurs since the piston usually has some kinetic energy that it must lose before turning around. The piston reaches zero velocity at a volume $V_{min} \leq V_2$. The minimum combustion-volume $min[V_2]$ for this cylinder is specified at a clearance volume of V_c so that the piston can turn around without crashing into the cylinder head. No net work is done in the overshoot segments.

Segment $S_{3\to 5}$ represents the reversible, adiabatic expansion of the hot gas pocket back to a volume V_1. The exhaust port opens as soon as the volume reaches V_1, following which the pressure is assumed to drop instantaneously to atmospheric pressure. Exhaust of spent charge occurs along segment $S_{1\to 0}$, with the pressure remaining atmospheric.

An estimate of the heat input to the gas at combustion is required to complete

the mathematical description of this cycle. Heat transfer to the piston and cylinder walls is not included in the model and it is assumed that the estimate for the input heat takes that into account. In addition, the model neglects the change in gas composition due to combustion and assumes that the mass of the gas in the pocket remains constant throughout the closed portion of cycle. The exhaust of spent charge and the intake of fresh charge are modeled by an equivalent constant volume heat transfer process for a fixed gas pocket. The work done to push the exhaust out and pull the fresh charge into the chamber and all other losses are lumped into an external linear damper.

3.3 Cycle model

This section details the derivation of the relationship between the pressure p and volume V of the gas pocket in terms of the pressure versus cylinder volume diagram shown in Figure 3-3. The gas pocket is characterized by a boundary, and three state variables: a temperature T, a volume V, and a pressure p.

3.3.1 Segment $S_{0\to1}$

Along this segment the gas in the cylinder is open to the environment and the pressure is given by,

$$p = p_{atm} \tag{3.6}$$

3.3.2 Segment $S_{1\to2}$

The gas pocket closes and undergoes reversible, adiabatic compression when the piston passes the exhaust valve. For the gas pocket defined, conservation of energy dictates,

$$dU_t = dQ - dW \tag{3.7}$$

where dU_t is the incremental change in the thermal energy stored in the gas pocket, dQ is the incremental heat transfered from the environment to the gas pocket, and

dW is the incremental work done by the gas pocket on the environment.

For an adiabatic process the first law reduces to,

$$dU_t + dW = 0 \tag{3.8}$$

An increment in stored thermal-energy dU_t can be expressed as,

$$dU_t = mc_v dT \tag{3.9}$$

where m is the mass of the gas in the pocket, c_v is the heat capacity of the gas, and dT is the increment in pocket temperature. An increment in work dW is given by,

$$dW = pdV \tag{3.10}$$

where dV is the incremental change in pocket volume. Consequently Equation 3.11 can be rewritten as,

$$mc_v dT + pdV = 0 \tag{3.11}$$

which when solved for dT gives the expression,

$$dT = -\frac{1}{mc_v} pdV \tag{3.12}$$

The ideal gas law is assumed to hold and is given by,

$$pV = mRT \tag{3.13}$$

where R is the gas constant. Stating the ideal gas law in incremental form gives the relation,

$$pdV + Vdp = mRdT \tag{3.14}$$

Substitution of Equation 3.12 into Equations 3.14 eliminates dT,

$$(1 + \frac{R}{c_v})pdV + Vdp = 0 \tag{3.15}$$

This expression can be rearranged so that it is in the form,

$$\gamma \frac{dV}{V} + \frac{dp}{p} = 0 \tag{3.16}$$

where $\gamma = 1 + \frac{R}{c_v}$ is a constant property of the gas.

Integration of Equation 3.16 places the following constraint on the variables p and V,

$$pV^{\gamma} = k \tag{3.17}$$

where k is a constant of integration. Since the pressure p_{atm} is associated with a volume V_1 at the start of this segment, the pressure p of the gas at any other volume V between V_1 to V_2 must be,

$$p = p_{atm} \left(\frac{V_1}{V} \right)^{\gamma} \tag{3.18}$$

which is the well known pressure versus volume relationship for a gas pocket undergoing a reversible, adiabatic process. Thus,

$$p_2 = p_{atm} \left(\frac{V_1}{V_2} \right)^{\gamma} \tag{3.19}$$

3.3.3 Segment $S_{2\rightarrow 3}$

This section details the derivation of the ratio of pressures before and after combustion takes place. The combustion process is assumed to occur instantaneously at constant volume V_2, which implies,

$$\Delta W = p\Delta V = 0 \tag{3.20}$$

Conservation of energy for the combustion event can be written as,

$$\Delta U_t = \Delta Q - \Delta W \tag{3.21}$$

Since $\Delta W = 0$, all of the heat goes into stored thermal energy, as expressed by,

$$\Delta U_t = \Delta Q_{23} \tag{3.22}$$

where ΔQ_{23} is the heat transfered to the gas by the combustion process. Combining Equation 3.22 with the definition,

$$\Delta U_t = mc_v \Delta T \tag{3.23}$$

leads to the expression,

$$\Delta T = \frac{\Delta Q_{23}}{mc_v} \tag{3.24}$$

The ideal gas law written for a change in pressure Δp while holding the volume constant at V_2 yields,

$$\Delta p = \frac{mR\Delta T}{V_2} \tag{3.25}$$

which when combined with Equation 3.24 gives,

$$\Delta p = \frac{\frac{R}{c_v}\Delta Q_{23}}{V_2} \tag{3.26}$$

which can be rewritten in terms of γ and the pressures p_3 and p_2 before and after the combustion event,

$$p_3 - p_2 = \frac{(\gamma - 1)\Delta Q_{23}}{V_2} \tag{3.27}$$

It is useful to define the pressure ratio $K_c = \frac{p_3}{p_2}$ where K_c is given by,

$$K_c = 1 + \frac{(\gamma - 1)\Delta Q_{23}}{p_2 V_2} \tag{3.28}$$

Substitution of p_2 from Equation 3.19 into Equation 3.28 leads to,

$$K_c = 1 + \frac{(\gamma - 1)\Delta Q_{23} V_2^{(\gamma-1)}}{p_{atm} V_1^{\gamma}} \tag{3.29}$$

The pressure p_3 at the end of this segment is given by,

$$p_3 = K_c p_2 \tag{3.30}$$

3.3.4 Segments $S_{3\to4}$ and $S_{4\to3}$

The overshoot segment is just an extrapolation of Segment $S_{3\to5}$ out to a volume $V_{min} \leq V_2$. The gas in the pocket undergoes reversible, adiabatic compression starting from a volume V_2 at a pressure p_3 to a volume V_{min}. The pressure-volume relationship is given by,

$$p = p_3 \left(\frac{V_2}{V}\right)^{\gamma} \tag{3.31}$$

After the gas pocket reaches the minimum volume V_{min}, it expands back to a volume V_2 at a pressure p_3 along the same curve as in Equation 3.31.

The value of the volume V_{min} (corresponding to a maximum overshoot z_{max}), to which the piston overshoots, depends on the distribution of stored energy in the system when combustion occurs and hence is determined by solving the dynamics of the overall system.

3.3.5 Segment $S_{3\to5}$

The gas undergoes reversible, adiabatic expansion from an initial volume of V_2 at an initial pressure p_3 to volume V_1. The pressure-volume relationship is,

$$p = p_3 \left(\frac{V_2}{V}\right)^{\gamma} \tag{3.32}$$

which can be written in terms of p_2 (see Equation 3.30),

$$p = K_c p_2 \left(\frac{V_2}{V}\right)^{\gamma} \tag{3.33}$$

Substituting p_2 from Equation 3.19 gives,

$$p = K_c p_{atm} \left(\frac{V_1}{V}\right)^{\gamma} \tag{3.34}$$

Equation 3.34 gives the pressure at the end of this segment p_5 as,

$$p_5 = K_c p_{atm} \tag{3.35}$$

3.3.6 Segment $S_{5\to1}$

The pressure is assumed to drop instantaneously to atmospheric pressure at a constant volume V_1. This means that the pressure drops by,

$$\Delta p = (K_c - 1)p_{atm} \tag{3.36}$$

We can reverse the results of the combustion analysis for segment $S_{2\to3}$ to find the amount of heat the system loses as a result of this pressure drop,

$$\Delta Q_{51} = \frac{1}{\gamma - 1}(K_c - 1)p_{atm}V_1 \tag{3.37}$$

Substituting the expression for K_c from Equation 3.29 gives,

$$\Delta Q_{51} = -\Delta Q_{23}\left(\frac{V_2}{V_1}\right)^{(\gamma-1)} \tag{3.38}$$

3.3.7 Segment $S_{1\to0}$

The pressure remains atmospheric throughout segment $S_{1\to0}$.

3.4 Cycle efficiency

The cycle under consideration is modeled as a closed, equilibrium process. Hence, going through the cycle cannot alter the energy stored in the gas pocket (otherwise the temperature of the gas in the pocket would keep increasing every cycle). This means that for a cycle,

$$\Delta U_t = 0 \tag{3.39}$$

which in turn means that for a cycle,

$$\Delta W = \Delta Q \tag{3.40}$$

This right-hand side of Equation 3.40 can be expanded to,

$$\Delta Q = \Delta Q_{01} + \Delta Q_{12} + \Delta Q_{23} + \Delta Q_{34} + \Delta Q_{43} + \Delta Q_{35} + \Delta Q_{51} + \Delta Q_{10} \tag{3.41}$$

The only nonzero quantities in Equations 3.41 are ΔQ_{23} and ΔQ_{51}. Thus the net heat converted to mechanical work per cycle is,

$$W_{cyc} = \Delta W = \Delta Q_{23} + \Delta Q_{51} \tag{3.42}$$

Note that the fraction of ΔQ_{23} that gets converted to mechanical work is given by,

$$\eta = \frac{\Delta Q_{23} + \Delta Q_{51}}{\Delta Q_{23}} = 1 - \left(\frac{V_2}{V_1}\right)^{(\gamma-1)} \tag{3.43}$$

which is a function of only the compression ratio $\frac{V_2}{V_1}$. This yields the following expression for W_{cyc},

$$W_{cyc} = \eta \Delta Q_{23} \tag{3.44}$$

An estimate of ΔQ_{23} is required to complete the description of the cycle. The estimate for ΔQ_{23} used in the thesis is largely arbitrary, as no empirical data enabling its more exact determination could be obtained. The value of $\Delta Q_{23} = 28$ J was chosen to match the expected work per-cycle given the size of the cylinder, with the understanding that this quantity must determined empirically[2].

[2]Prof. J. L. Smith Jr., Private communication

3.5 Left and right cylinder pressures as a function of displacement

This section combines the results of Sections 3.3 and 3.1 to write expressions for the left and right cylinder pressures as a function of the displacement z. Figure 3-4 illustrates typical pressure trajectories for both cylinders superimposed on the z axis. Four critical points on the z axis characterize the curves: the locations of the exhaust port and firing position for each cylinder (z_1 and $-z_2$ for the left cylinder, and $-z_1$ and z_2 for the right cylinder).

The following set of equations describes the pressure versus position trajectory for the left cylinder. While the exhaust port is open (i.e., $z > z_1$),

$$p_l = p_{atm} \tag{3.45}$$

Along the bottom leg of the trajectory ($-z_2 < z < z_1$),

$$p_l = p_{atm}\left(\frac{V_1}{A(\frac{1}{2}y_{cc} + z) + V_{dead}}\right)^{\gamma} \tag{3.46}$$

At $z = -z_2$ the trajectory jumps to trace the following curve as the piston overshoots from z_2 to z_{max} then slides back to z_1,

$$p_l = K_c p_{atm}\left(\frac{V_1}{A(\frac{1}{2}y_{cc} + z) + V_{dead}}\right)^{\gamma} \tag{3.47}$$

The system resets when the exhaust port opens again $z > z_1$,

$$p_l = p_{atm} \tag{3.48}$$

Similarly, the trajectory of the right cylinder pressure follows the following relations. When $z < -z_1$ the pressure is,

$$p_r = p_{atm} \tag{3.49}$$

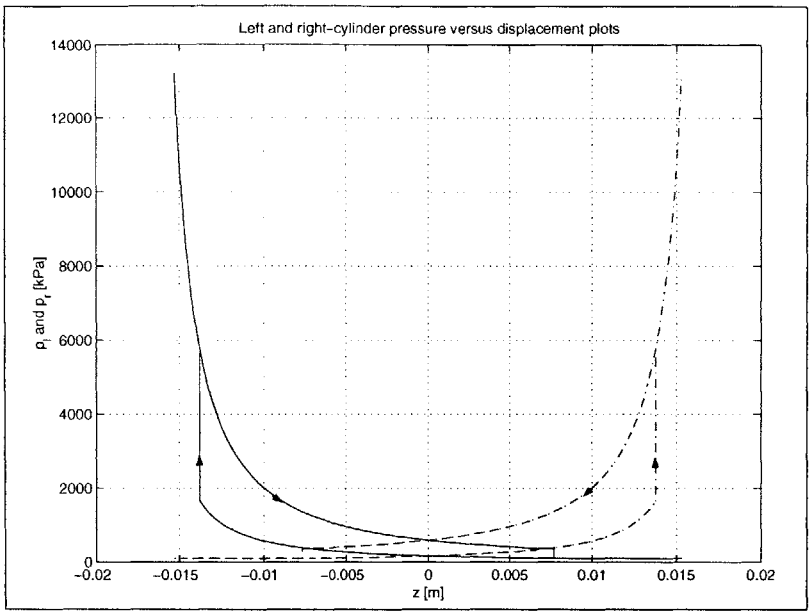

Figure 3-4: Left (solid) and Right (dashed) cylinder cycles

Along the bottom leg of the plot and while $-z_1 < z < z_2$ the right cylinder pressure is given by,

$$p_r = p_{atm}\left(\frac{V_1}{A(\frac{1}{2}y_{cc} - z) + V_{dead}}\right)^{\gamma} \tag{3.50}$$

At $z = z_2$ the trajectory jumps to trace the following curve as the piston overshoots from z_2 to z_{max} and as long as $z > -z_1$,

$$p_r = K_c p_{atm}\left(\frac{V_1}{A(\frac{1}{2}y_{cc} - z) + V_{dead}}\right)^{\gamma} \tag{3.51}$$

Again, the system resets when the exhaust port opens $z < -z_1$,

$$p_r = p_{atm} \tag{3.52}$$

3.6 Force on the reciprocating assembly

The force exerted by the gas on the reciprocating assembly f_g is a hystertic function of z, and is given by the difference of left and right cylinder pressures $p_l(z)$ and $p_r(z)$

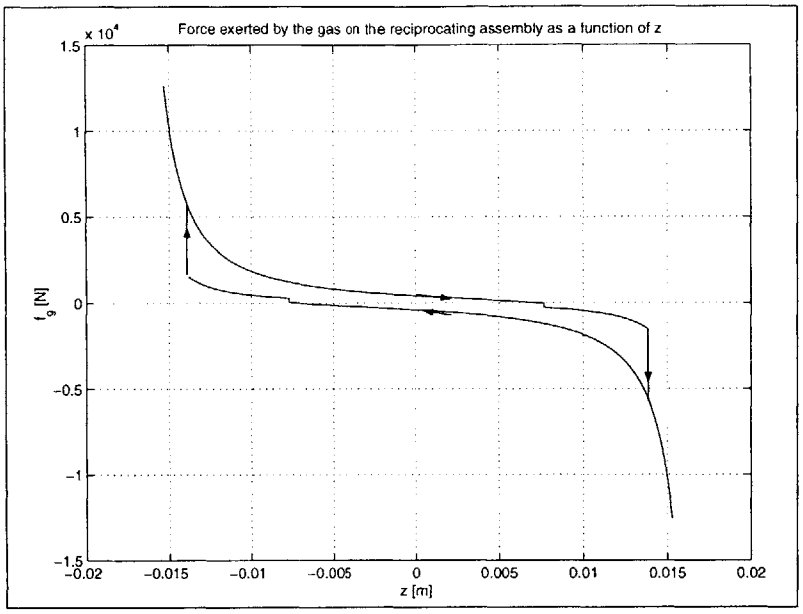

Figure 3-5: Force on the reciprocating assembly due to the difference between left and right cylinder pressures ($z_2 = 0.0138$ m, $\Delta Q_{23} = 28$ J)

as expressed by the equation,

$$f_g = A(p_l(z) - p_r(z)) \tag{3.53}$$

where A is the cross-sectional area of the cylinder. Figure 3-5 shows a plot of the force, which has two values for each z depending on which cylinder fired last. For the upper leg of the force-position plot (combustion just took place in the left cylinder), if $|z| < z_1$ the force exerted by the gas on the reciprocating assembly is given by,

$$f_g = Ap_{atm}\left(K_c\left(\frac{V_1}{A(\frac{1}{2}y_{cc}+z)+V_{dead}}\right)^{\gamma} - \left(\frac{V_1}{A(\frac{1}{2}y_{cc}-z)+V_{dead}}\right)^{\gamma}\right) \tag{3.54}$$

While if $z > z_1$,

$$f_g = Ap_{atm}\left(1 - \left(\frac{V_1}{A(\frac{1}{2}y_{cc}-z)+V_{dead}}\right)^{\gamma}\right) \tag{3.55}$$

Finally, if $z < -z_1$,

$$f_g = Ap_{atm}\left(K_c\left(\frac{V_1}{A(\frac{1}{2}y_{cc}+z)+V_{dead}}\right)^{\gamma} - 1\right) \tag{3.56}$$

Likewise, for the lower leg (combustion just took place in the right cylinder), if $|z| < z_1$ the force exerted by the gas on the piston assembly is given by,

$$f_g = Ap_{atm}\left(\left(\frac{V_1}{A(\frac{1}{2}y_{cc}+z)+V_{dead}}\right)^{\gamma} - K_c\left(\frac{V_1}{A(\frac{1}{2}y_{cc}-z)+V_{dead}}\right)^{\gamma}\right) \tag{3.57}$$

While if $z > z_1$,

$$f_g = Ap_{atm}\left(\left(\frac{V_1}{A(\frac{1}{2}y_{cc}+z)+V_{dead}}\right)^{\gamma} - 1\right) \tag{3.58}$$

Finally, if $z < -z_1$,

$$f_g = Ap_{atm}\left(1 - K_c\left(\frac{V_1}{A(\frac{1}{2}y_{cc}-z)+V_{dead}}\right)^{\gamma}\right) \tag{3.59}$$

3.7 Mechanical losses

The engine model developed in the previous sections does not include any loss mechanisms. Some work needs to be done each cycle to push the exhaust out of the cylinder, pull the fresh charge into the cylinder, overcome friction, and compensate for heat leaking out of the cylinder walls. These and all other mechanical losses are lumped into an external linear-damper exerting a force f_d given by,

$$f_d = B\frac{dz}{dt} \tag{3.60}$$

where B is the damping coefficient.

The linear damping characteristic given by Equation 3.60 is largely arbitrary. The damping coefficient B must account for all the non-electrical losses, and needs to be determined empirically.

Chapter 4

System model

The numerical simulation developed for this thesis consists of simple component models that can be combined to predict the complicated dynamic behavior of the overall system. These include the alternator model, the engine model and the models for the electrical loads. This section presents the framework for the overall system model. The alternator model used in this section is summarized in Section 2.7. The expressions for the force exerted by the gas on the reciprocating assembly are summarized in Section 3.6. Simple models for resistive and battery-charging loads will be presented in Section 4.1 before proceeding to tie the individual component models together in Section 4.2. The component models are assembled in a framework based on Newtonian rigid-body mechanics, Kirchhoff's electric-circuit laws, and the configuration of the engine/alternator/load system.

4.1 Modeling the load

The models developed for this thesis were used to investigate the system's dynamic behavior for two kinds of loads: a resistive load, and a full-bridge-rectifier battery-charging load. The load models are illustrated in Figure 4-1. The resistive load was chosen to simplify the analytical and empirical investigation of the system's dynamic behavior. Battery-charging operation introduces non-linear dynamics that add to to the complexity of the system. This load was investigated since it is the intended

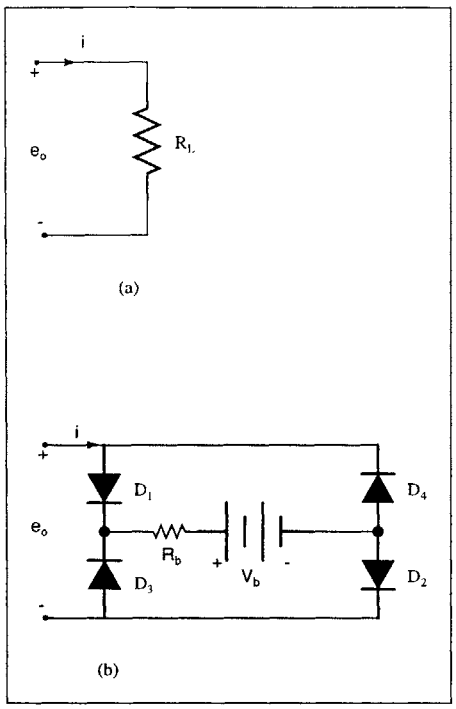

Figure 4-1: Models for the electrical loads: a resistive load (a), full-wave rectifier and a battery (b)

application for the system under investigation.

4.1.1 Resistive load

A resistive load connected to the alternator terminals imposes the relationship,

$$e_o = R_L i \tag{4.1}$$

on the alternator terminal-voltage and current, where R_L is the load resistance.

4.1.2 Battery load

From Figure 4-1(b), the terminals of the battery can be seen to be connected to the output of the linear alternator through a full-wave rectifier. The battery is modeled as the series connection of a DC voltage-source V_b and a small internal resistance R_b. The voltage drops across the rectifier diodes are neglected, because they are very small compared to the battery voltage.

The nonlinearity of the full-wave rectifier complicates the terminal relation for a battery-charging load. The full-wave rectifier in Figure 4-1 has three reachable states: state S_a where diodes 1 and 2 are on and diodes 3 and 4 are off, state S_b where diodes 3 and 4 are on and diodes 1 and 2 are off, or state S_c where all the diodes are off.

State S_a For state S_a the terminal relation is given by,

$$e_o = R_b i + V_b \tag{4.2}$$

During this state diodes 1 and 2 are on, while diodes 3 and 4 are off. This state remains valid for,

$$e_o \geq V_b \tag{4.3}$$

State S_b The terminal relation for state S_b is given by,

$$e_o = R_b i - V_b \tag{4.4}$$

where diodes 3 and 4 are on and diodes 1 and 2 are off. This state remains valid for,

$$e_o \leq -V_b \tag{4.5}$$

State S_c Finally for state S_c the output terminals are open,

$$i = 0 \tag{4.6}$$

The bridge may switch from state S_c to either state S_a or S_b. Diodes 1 and 2 start to turn-on and the bridge switches to state S_a if,

$$e_{af} > V_b \tag{4.7}$$

Diodes 3 and 4 start to turn-on and the bridge switches to state S_b if,

$$e_{af} < -V_b \tag{4.8}$$

4.2 Framework for the system model

The system model, assembled from the component models discussed previously, consists of three first-order, non-linear differential equations in three state variables: the displacement of the reciprocating-assembly z, the reciprocation velocity v and the winding current i. Figure 4-2 shows the lumped-parameter models for the electrical, mechanical, and electromechanical components of the engine/alternator/load configuration. Using Newton's law and Kirchhoff's voltage law, the information presented in the figure can be summarized by the following set of differential equations,

$$\frac{dz}{dt} = v \tag{4.9}$$

$$\frac{dv}{dt} = \frac{1}{m}(f_e + f_g + f_m + f_d) \tag{4.10}$$

$$\frac{di}{dt} = \frac{1}{L_w}(e_{af} - R_w i - e_o) \tag{4.11}$$

where m is the mass of the moving assembly, f_e is the force of electrical origin (Equation 2.53 in Section 2.7), f_g is the force due to the difference in cylinder pressures (Equations 3.54-3.59 from Section 3.6), f_m is the axial magnetic spring-force (Equation 2.54 in Section 2.7), f_d is the damping force discussed in Section 3.7, L_w is the winding inductance (Equation 2.51 in Section 2.7), R_w is the winding-resistance, the internal voltage e_{af} is given by Equation 2.52 in Section 2.7, and e_o is the terminal voltage of the load as outlined by Equations 4.1-4.8 in Section 4.1.

4.3 Model implementation in C-code

Section 4.2 concludes the presentation of the modeling and analysis of the free-piston-driven linear-alternator system. The next chapters present the results and the con-

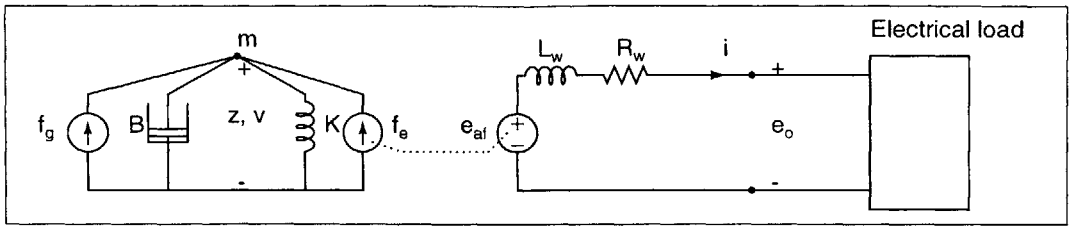

Figure 4-2: Lumped parameter model of the system

clusions of a numerical simulation of the model and make recommendations for future work .

The model components and overall system framework discussed in Section 4.2 have been implemented in a program written in C-code. The Runge-Kutta algorithm with a fixed step size of 1.5×10^{-7} seconds was used to solve the set of Equations 4.9-4.11. Given the initial conditions $z(t = 0)$, $v(t = 0)$ and $i(t = 0)$ the program proceeds to record the three state variables $z(t)$, $v(t)$ and $i(t)$ at each time step until the end of the simulation-interval is reached.

Output from the program is saved as the text of a MATLAB[1] script file. MATLAB's built-in data-processing and graphics tools can then be used to generate graphical results and analyze the data. Appendix A lists the C-code used in the simulation.

[1]MATLAB, The MathWorks, Inc. 24 Prime Park Way, Natick, Mass. 01760

Chapter 5

Simulation results

The simulation code developed for this thesis has been used to investigate the dynamics of the engine/alternator/load system. The simulations predict the existence of a range of resistive and battery loads for which the system is self stabilizing. Any load outside this range causes the reciprocating assembly to either "crash" into the cylinder head or "stall" (i.e., stop firing).

The results are presented in four sections. Section 5.1 presents a set of simulation runs which demonstrate typical dynamic behavior for resistive loads. The predicted steady-state operating characteristics for resistive loads are presented in Section 5.2. The case of a battery load is treated similarly in Sections 5.3 and 5.4.

Table 5.1 documents the set of fixed parameters for the simulation runs presented in this chapter. These parameters were chosen to represent the two-stroke, free-piston-engine driven linear-alternator prototype built by Galileo Research.

A series of preliminary simulation runs demonstrated that the behavior of the system is very sensitive to three parameters: the heat input at combustion ΔQ_{23}, the firing position z_2, and, depending on the type of electrical load, either the laod resistance R_L or the battery voltage V_b. This makes sense since given the parameters in Table 5.1, ΔQ_{23} and z_2 determine the net mechanical-work done by the engine per cycle, while R_L and V_b determine the power delivered to the load per cycle.

It is possible to adjust firing position z_2 in the experimental prototype built by Galileo Research. The left and right spark-plugs are triggered to fire whenever the

Table 5.1: Values of fixed parameters for the simulation runs

Engine fixed parameters	
γ	1.40
z_1	7.70 mm
y_{cc}	30.60 mm
A	9.62 cm^2
V_1	23.93 cm^3
V_{dead}	1.80 cm^3
m	6.4 kg
B	0.0 kg/s
Alternator fixed parameters	
L_w	7.19 mH
R_w	0.211 Ohms
N	63
K	9.52 kg/s^2
q_1	0.0118
q_3	152.8
Battery fixed parameters	
R_b	0.001 Ohms

piston assembly is displaced by $-z_2$ and z_2, where z_2 can be adjusted from a maximum value of 0.0138 m to a minimum value of 0.0118 m. However the value of ΔQ_{23} is determined by the details of the combustion process, and hence is not as controllable as z_2.

Rather than exhaustively exploring the parameter space for ΔQ_{23} and z_2 for both electrical loads, the simulations presented in this chapter hold ΔQ_{23} fixed at 7 J. Note that this is 25% of the estimated value of 28 J (see Section 3.4). The reason for this reduction is that preliminary simulation runs show that the configuration summarized in Table 5.1 is completely unstable for values of ΔQ_{23} in excess of 7 J. The estimate of $\Delta Q_{23} = 7$ J was obtained by fixing z_2 at the maximum firing-position and R_L at 9.5 Ohms and then finding the largest ΔQ_{23} that resulted in stable steady-state operation. Clearly this choice is rather arbitrary and is made with the understanding that ΔQ_{23} needs to be based upon experimental results. Preliminary data from the prototype built by Galileo Research indicate that the combustion process in the engine is inefficient, and that ΔQ_{23} for the prototype might be even lower than 7 J.

The winding resistance R_w for the alternator used in the prototype was measured to be 0.0211 Ohms. The damping coefficient B is set to zero because no empirical data enabling its determination was available. However, note that since losses in general tend to make the system more stable, setting B to zero provides the severest conditions for assessing the transient dynamics of the system.

The transient simulations in this chapter all commence from the initial state,

$$z(t=0) = -z_2 \tag{5.1}$$

$$v(t=0) = 0 \tag{5.2}$$

$$i(t=0) = 0 \tag{5.3}$$

which corresponds to pulling the reciprocating assembly all the way to the left firing position and then releasing it from rest. Note that the left cylinder is set to fire at time $t = 0$.

5.1 Typical simulated dynamics for a resistive load

During the course of the investigation into the dynamics of the engine/alternator/load system for different resistive loads, three distinctive dynamic behaviors corresponding to three load-resistance ranges were observed. This section shows representative starting-transients for each resistance range where the firing position z_2 is set to 0.0138 m, and ΔQ_{23} to 7 J.

5.1.1 Crash transient

Using large load resistances results in transients similar to the plots in Figures 5-1 through 5-3. The value of R_L used in the simulation run that produced these figures is $R_L = 11$ Ohms.

Figure 5-1 shows the trajectory of the reciprocating assembly. Solid lines at $z = \pm 0.0153$ m indicate the positions of the left and right cylinder-heads, while the dashed lines at $z = \pm 0.0138$ m show the firing positions for this run. The figure shows that the piston crashes into the cylinder head on the ninth stroke. The collision is catastrophic for the engine and violates the assumptions of the standard Otto-cycle of the thermodynamic model. Therefore it is meaningless to continue the simulation past the time of collision.

Note the presence of a third harmonic component in the current waveform (Figure 5-3). This is due to the cubic flux to displacement relationship of the linear alternator. The third harmonic content is small compared to the fundamental, and hence the dominant electrical frequency of the system is the same as its mechanical frequency.

5.1.2 Stall transient

Small load resistances result in transients similar to the plots in Figures 5-4 through 5-6. A load resistance of $R_L = 4$ Ohms was used in the simulation run that generated these results.

Figure 5-4 shows the trajectory of the reciprocating assembly. Solid lines at $z = \pm 0.0153$ m indicate the positions of the left and right cylinder-heads, while the dashed

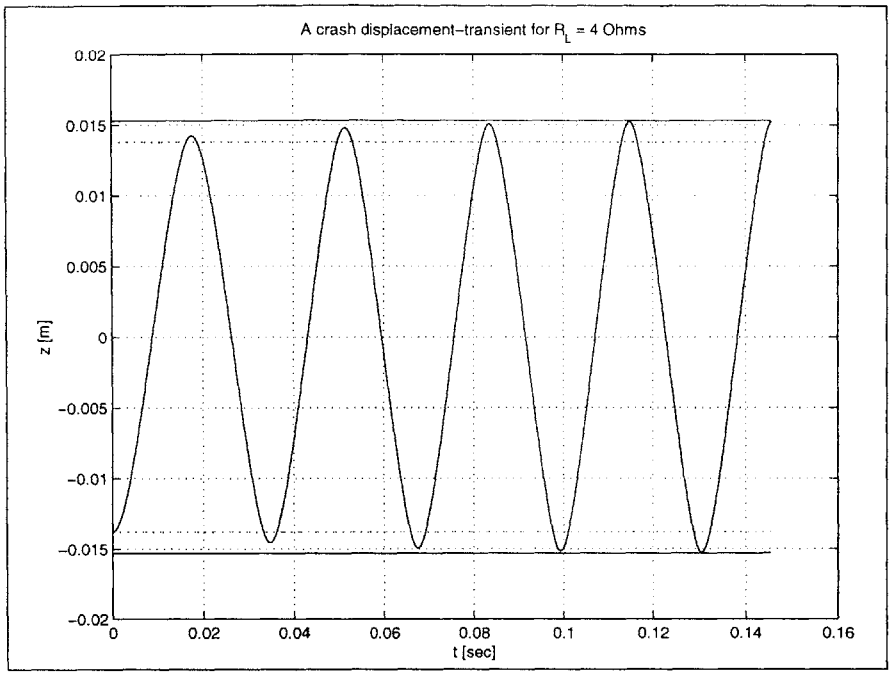

Figure 5-1: Typical displacement transient for a resistive load of $R_L = 11$ Ohms ("crash"). Solid lines at $z = \pm 0.0153$ m indicate the positions of the left and right cylinder-heads, while the dashed lines at $z = \pm 0.0138$ m show the firing positions z_2 for this run

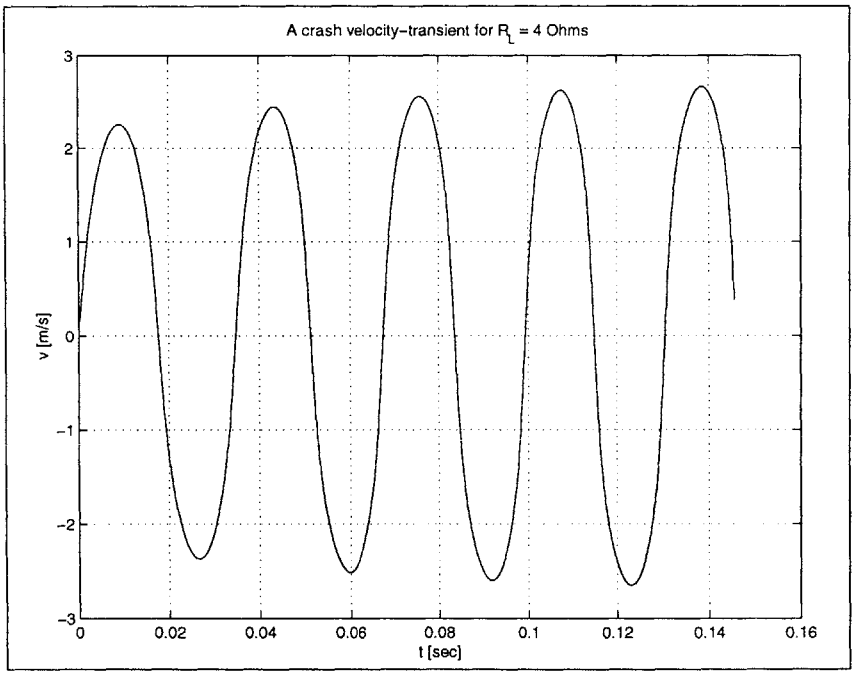

Figure 5-2: Typical velocity transient for a resistive load of $R_L = 11$ Ohms ("crash")

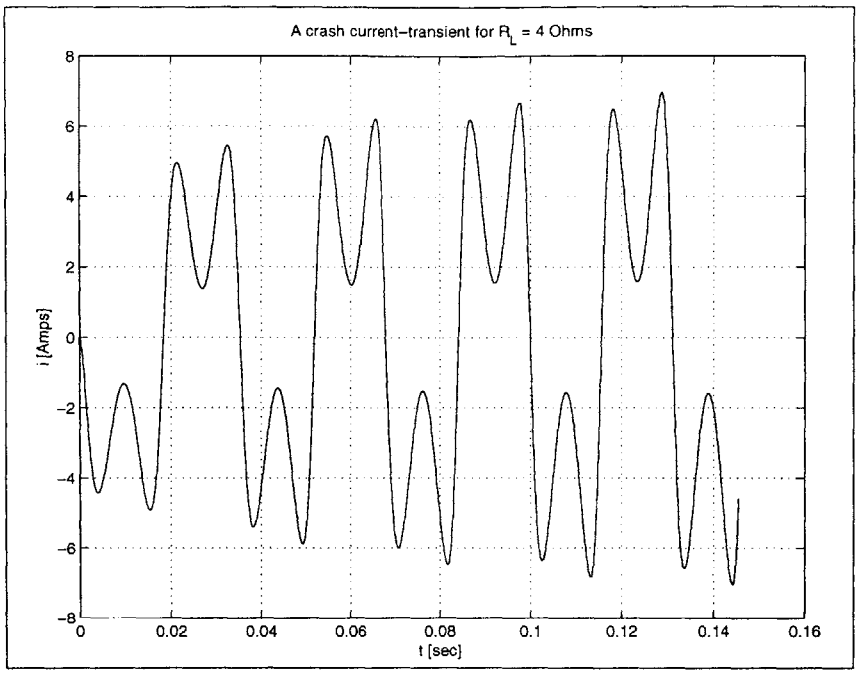

Figure 5-3: Typical current transient for a resistive load of $R_L = 11$ Ohms ("crash")

lines at $z = \pm 0.0138$ m show the firing positions for this run. The figure shows that the piston fails to reach the firing position z_2 on the first stroke. As soon as the a cylinder skips a combustion event the electrical losses dominate the dynamics and the system eventually comes to rest. Because the simulation does not include any mechanical losses, the system comes to rest very slowly.

5.1.3 Steady-state operation

The numerical simulation predicts that it is possible for the system under investigation to operate in the steady state for an intermediate range of load resistances. The load resistance chosen for this case is 7 Ohms. Figures 5-7 through 5-9 show typical plots of the state variables for this operating regime.

Figure 5-7 shows the trajectory of the reciprocating assembly. Note that the system is clearly in the steady state. Solid lines at $z = \pm 0.0153$ m indicate the positions of the left and right cylinder-heads, while the dashed lines at $z = \pm 0.0138$ m show the firing positions for this run.

It is interesting to note that the position and velocity waveforms in Figures 5-7

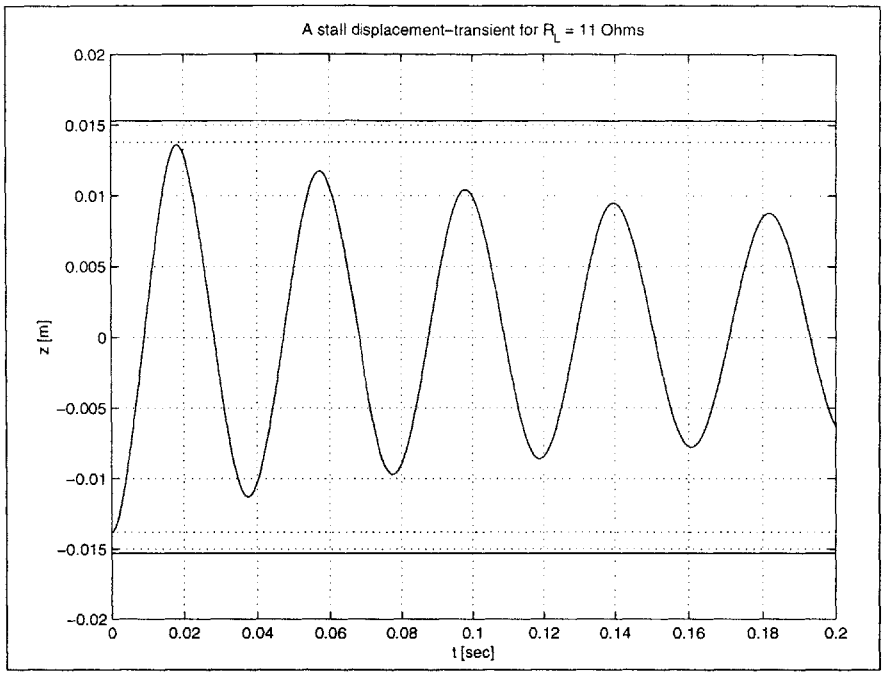

Figure 5-4: Typical displacement transient for a resistive load of 4 Ohms ("stall"). Solid lines at $z = \pm 0.0153$ m indicate the positions of the left and right cylinder-heads, while the dashed lines at $z = \pm 0.0138$ m show the firing positions z_2 for this run

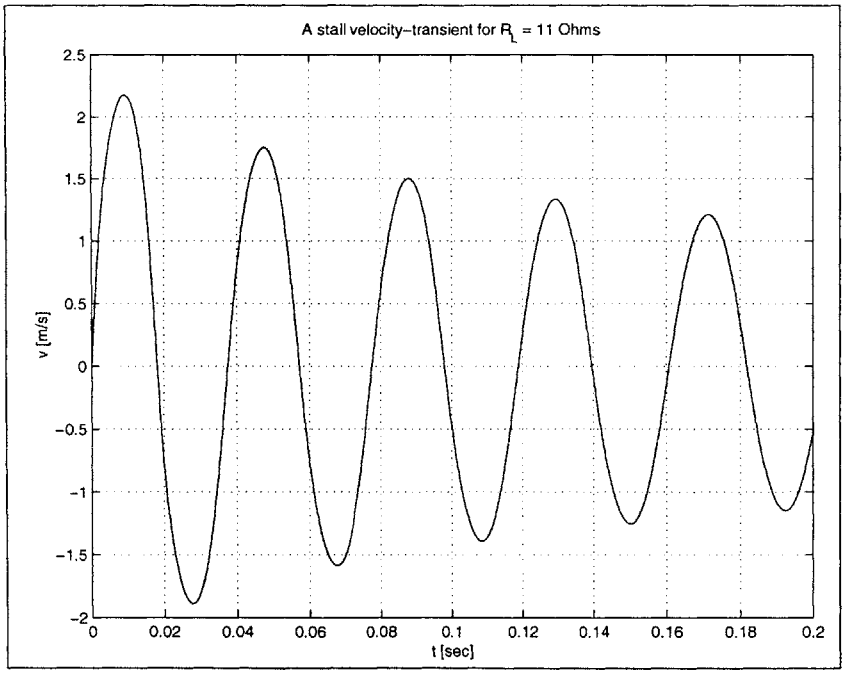

Figure 5-5: Typical velocity transient for a resistive load of 4 Ohms ("stall")

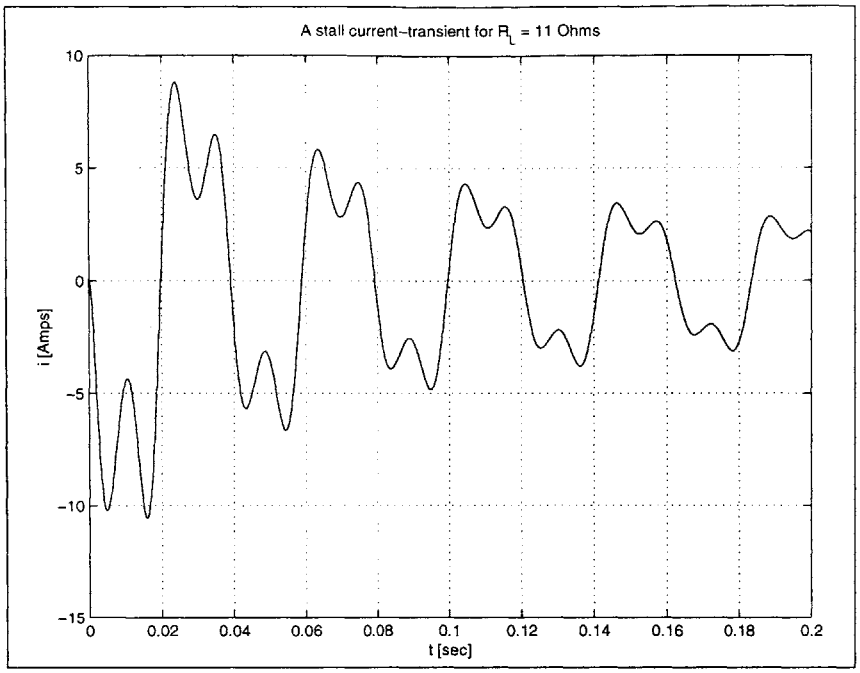

Figure 5-6: Typical current transient for a resistive load of 4 Ohms ("stall")

and 5-8 are very sinusoidal considering the non-linearities in the system. However, the current waveform continues to have third-harmonic content.

5.2 Resistive-load operating characteristics

A series of simulation runs have demonstrated the steady-state behavior shown in Section 5.1.3 for a range of resistor values. These results were observed to be relatively insensitive to small changes in the parameters in Table 5.1. Figures 5-10 through 5-12 characterize the steady-state operation of the system for three firing positions: $z_2 = 0.0138$ m (up triangles), $z_2 = 0.0128$ m (squares) and $z_2 = 0.0118$ m (down triangles). The figures display the maximum displacement, the cycle average of the extracted electric power, and the reciprocation frequency of the system versus the load resistance R_L.

It is important to note that the following relationship must hold in the steady state,

$$< P_e >_{cyc} = 2fW_{cyc} \tag{5.4}$$

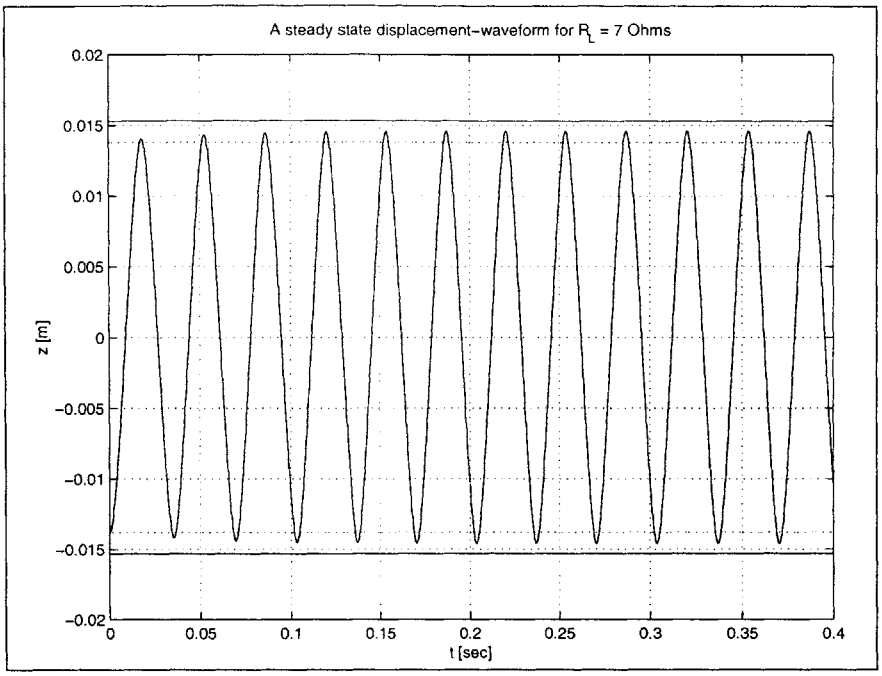

Figure 5-7: Typical steady-state displacement waveform for a resistive load of 7 Ohms. Solid lines at $z = \pm 0.0153$ m indicate the positions of the left and right cylinder-heads, while the dashed lines at $z = \pm 0.0138$ m show the firing positions z_2 for this run

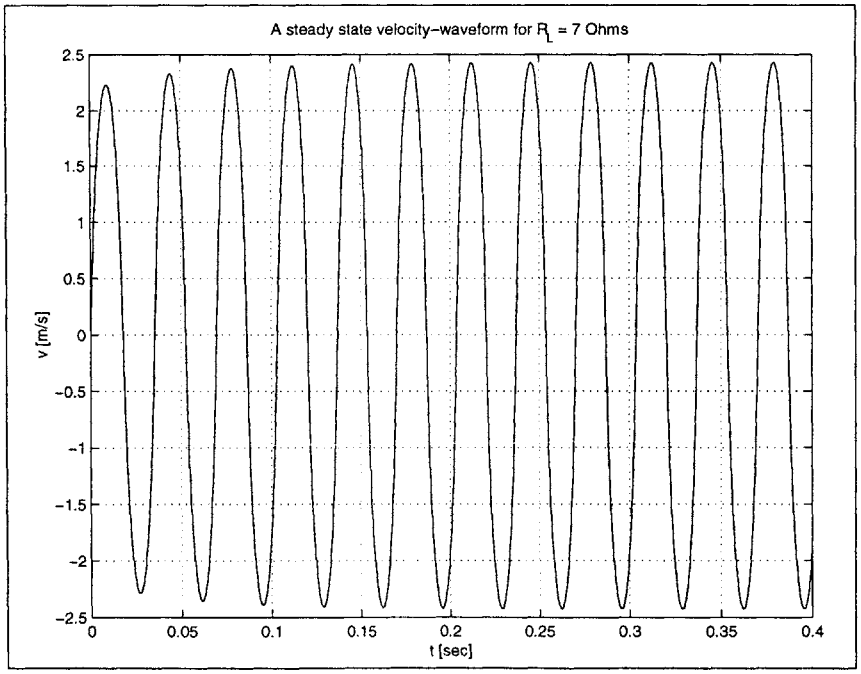

Figure 5-8: Typical steady-state velocity waveform for a resistive load of 7 Ohms

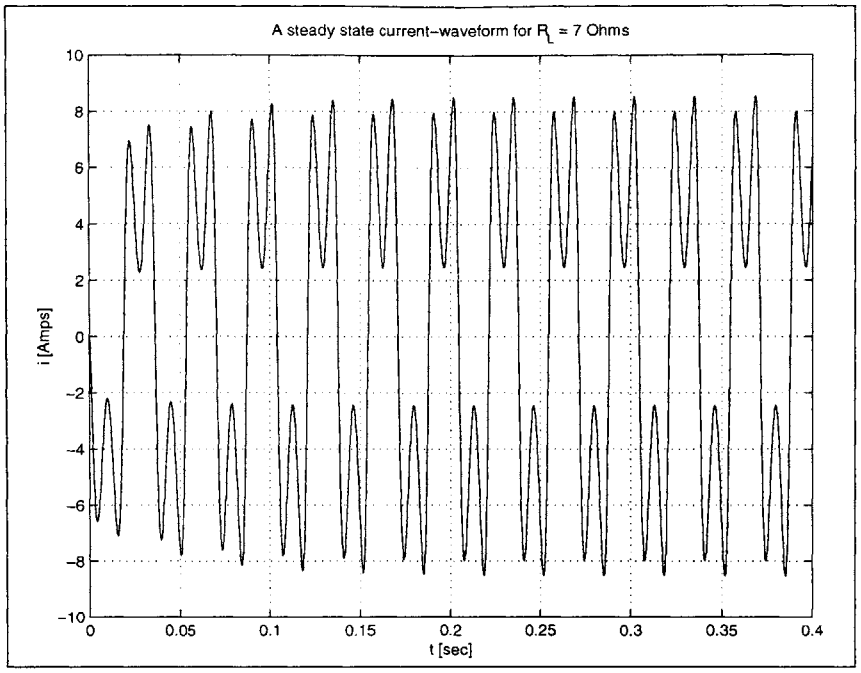

Figure 5-9: Typical steady-state current waveform for a resistive load of 7 Ohms

where $< P_e >_{cyc}$ is the cycle-average electrical-power dissipated in the alternator and delivered to the load, f is the steady-state frequency of the system, and $W_{cyc} = \Delta Q_{23} + \Delta Q_{51}$ is the net heat converted to mechanical work in each cylinder per cycle. Equation 3.44 gives W_{cyc} as a function of the firing position z_2, which, when substituted into Equation 5.4 yields,

$$\frac{< P_e >_{cyc}}{f} = 2\Delta Q_{23}(1 - \left(\frac{A(y_{cc} - z_2) + V_d}{V_1}\right)^{\gamma-1}) \tag{5.5}$$

Figure 5-13 shows a plot of the steady-state average electrical-power versus reciprocation frequency for the three firing positions. The figure demonstrates the linear relationship predicted by Equation 5.4. For $z_2 = 0.0138$ m the figure shows a slope of 7.64 W·s compared to the slope of 7.71 W·s predicted by Equation 5.5. For $z_2 = 0.0128$ m and $z_2 = 0.0118$ m the slopes shown on the figure are 7.00 W·s and 6.39 W·s, which are very close to the predicted slopes of 7.02 and 6.42. These results are within tolerance considering that they are based on averaging .4 seconds of simulation time.

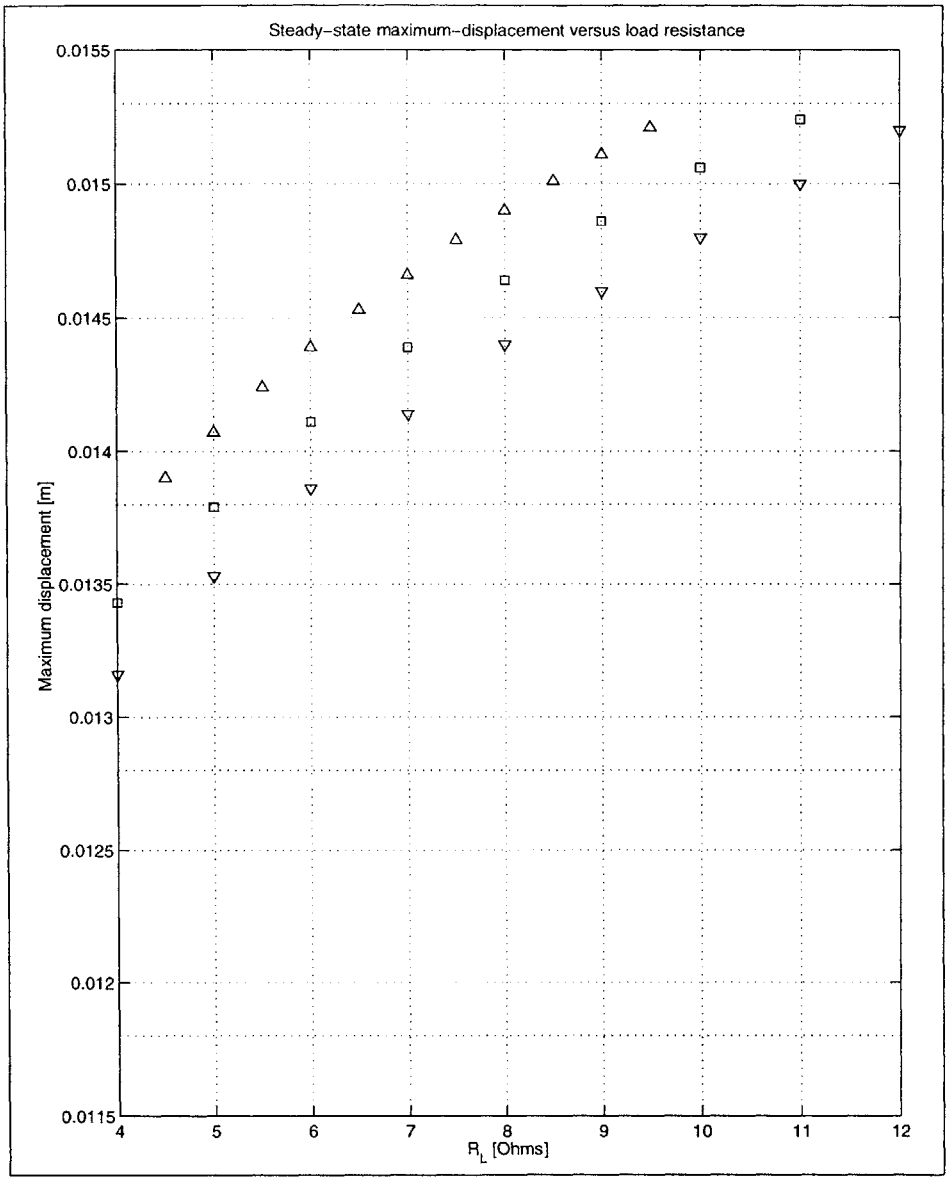

Figure 5-10: Characterization of the steady-state relationship between the maximum displacement of the reciprocating assembly and load resistance for three firing positions: up triangles for $z_2 = 0.0138$ m, squares for$z_2 = 0.0128$ m and down triangles for $z_2 = 0.0118$ m

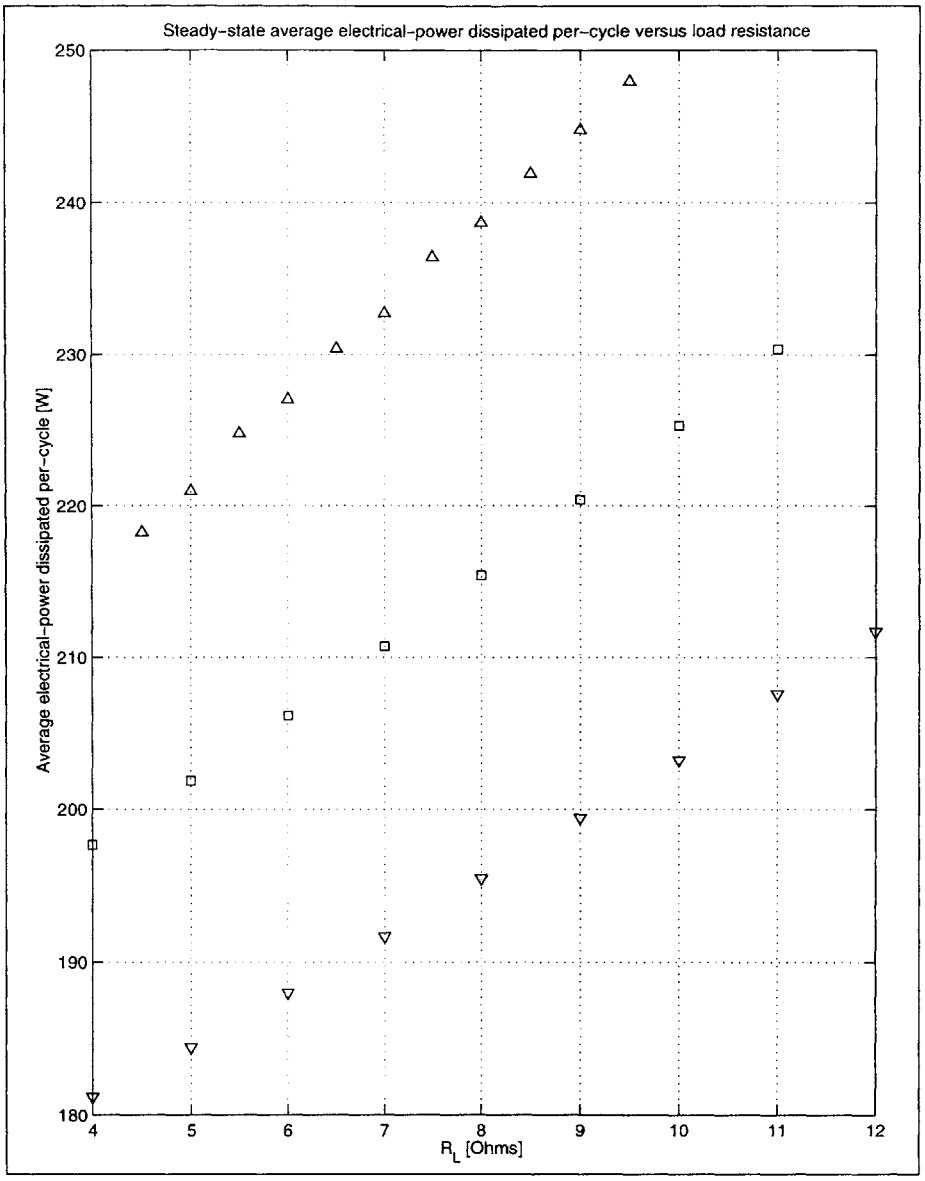

Figure 5-11: Characterization of the steady-state relationship between the cycle-average electrical-power and load resistance for three firing positions: up triangles for $z_2 = 0.0138$ m, squares for $z_2 = 0.0128$ m and down triangles for $z_2 = 0.0118$ m

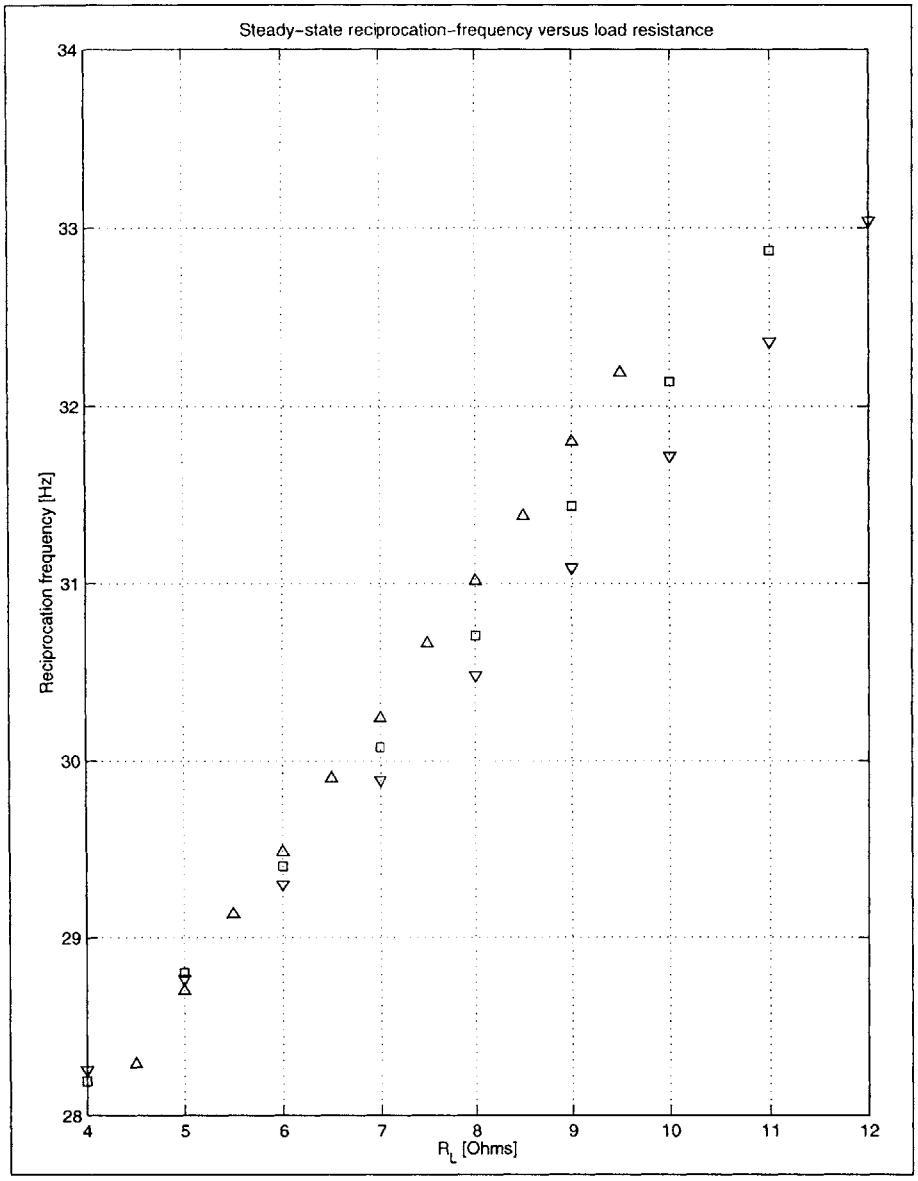

Figure 5-12: Characterization of the steady-state relationship between the frequency of reciprocation and load resistance for three firing positions: up triangles for$z_2 =$ 0.0138 m, squares for $z_2 = 0.0128$ m and down triangles for $z_2 = 0.0118$ m

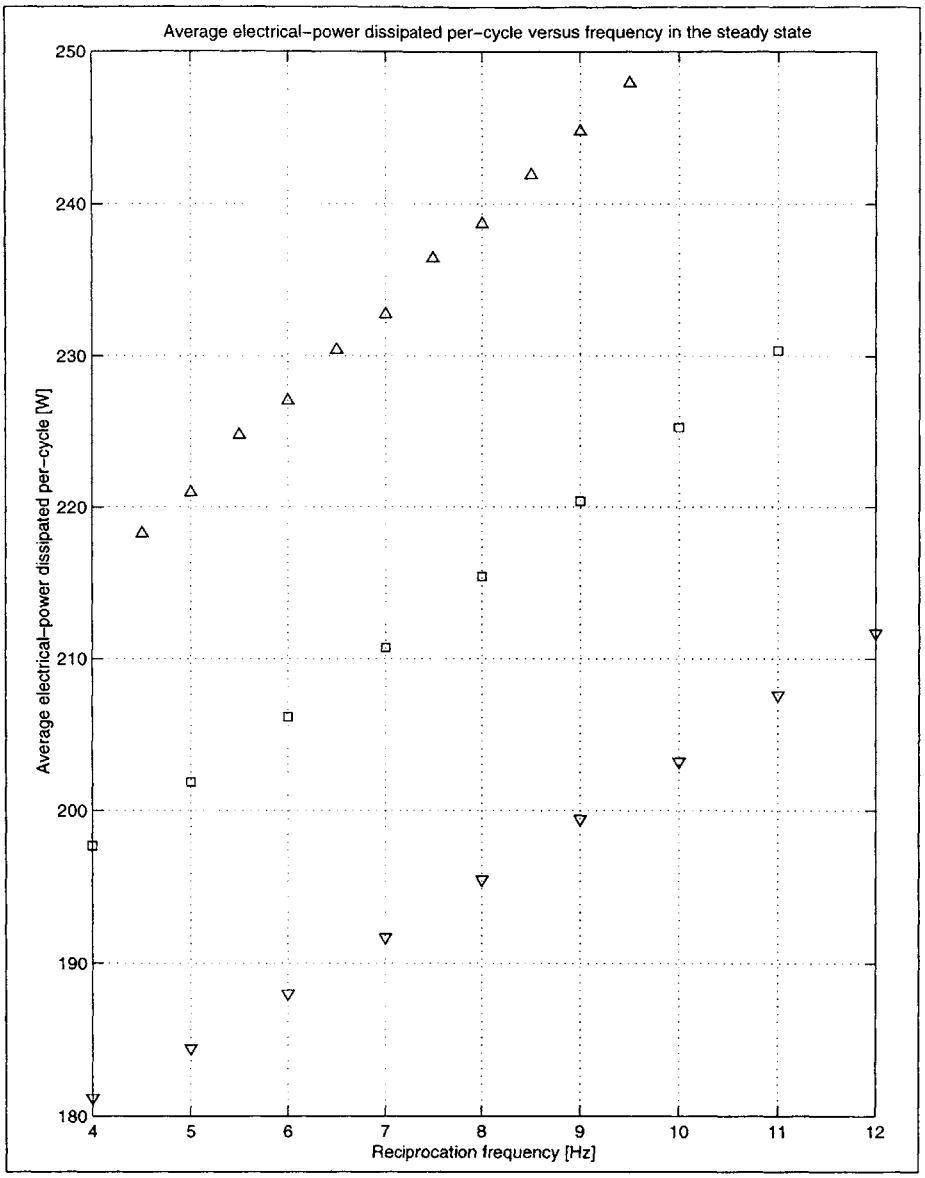

Figure 5-13: Characterization of the steady-state relationship between the cycle-average extracted electrical-power and reciprocation frequency for three firing positions: up triangles for $z_2 = 0.0138$ m, squares for $z_2 = 0.0128$ m and down triangles for $z_2 = 0.0118$ m

5.3 Typical simulated dynamics for a battery load

The battery-charging load simulations were run in a the same manner as the resistive-load simulations of Section 5.1. The investigation shows that the dynamics for the initial conditions given in Equations 5.1-5.3 can result in three distinctive behaviors depending on the value of the battery voltage V_b. This section presents typical plots for the observed behavior.

5.3.1 Crash transient

Using large battery voltages causes the piston to crash into the cylinder head (Figure 5-14). Figures 5-14 through 5-16 show typical plots of the state variables demonstrating this behavior. The value of V_b used in the simulation run that produced these plots is 48 Volts.

Figure 5-14 shows the trajectory of the reciprocating assembly. Solid lines at $z = \pm 0.0153$ m indicate the positions of the left and right cylinder-heads, while the dashed lines at $z = \pm 0.0138$ m show the firing positions for this run.

Note from Figure 5-16 that the rectifier operates in discontinuous conduction mode, with the terminals of the alternator remaining open for much of the cycle. The load cannot deliver the power input at each combustion to the battery, and the stroke continues to grow until the piston crashes into the cylinder head on the fourth stroke.

5.3.2 Stall transient

The engine stalls if the battery voltage is too small as demonstrated by Figures 5-17 through 5-19. The battery voltage was set to $V_b = 24$ Volts in the run that produced these plots.

Figure 5-14 shows the trajectory of the reciprocating assembly. Solid lines at $z = \pm 0.0153$ m indicate the positions of the left and right cylinder-heads, while the dashed lines at $z = \pm 0.0138$ m show the firing positions z_2 for this run. Note from the figure that the reciprocating assembly never reaches z_2 on the first stroke.

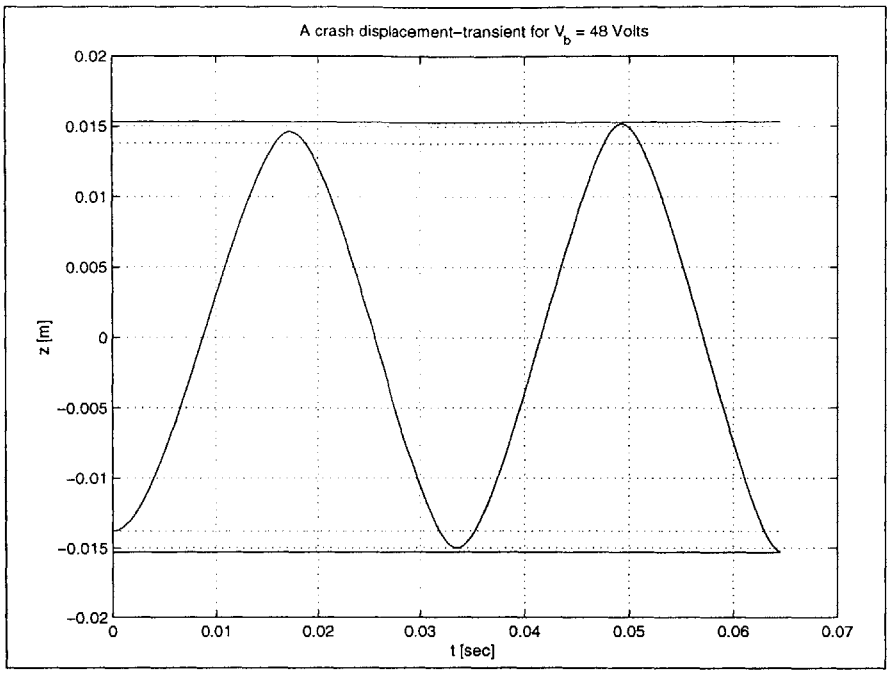

Figure 5-14: Typical displacement transient for $V_b = 48$ Volts ("crash"). Solid lines at $z = \pm 0.0153$ m indicate the positions of the left and right cylinder-heads, while the dashed lines at $z = \pm 0.0138$ m show the firing positions z_2 for this run

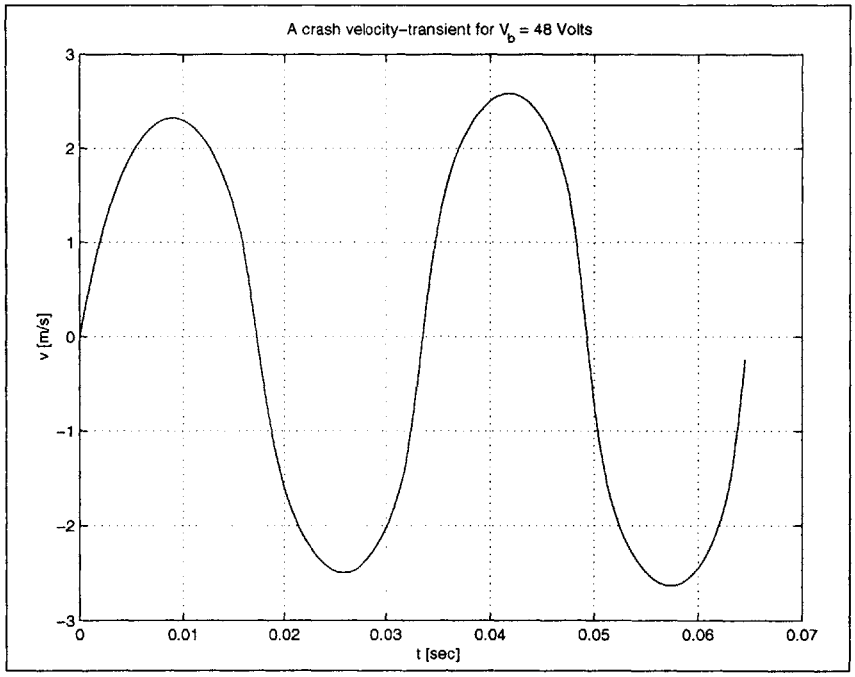

Figure 5-15: Typical velocity transient for $V_b = 48$ Volts ("crash")

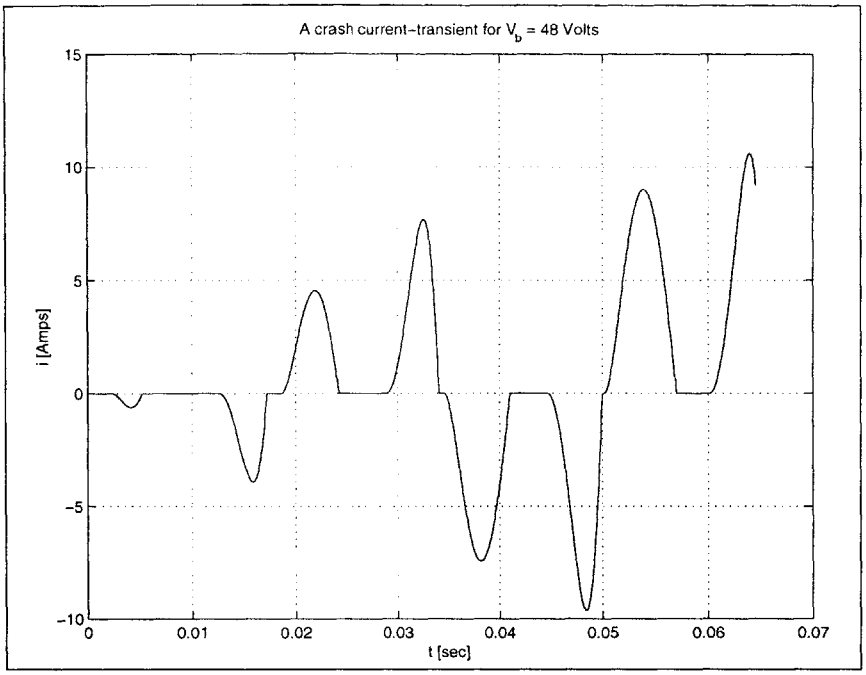

Figure 5-16: Typical current transient for $V_b = 48$ Volts ("crash")

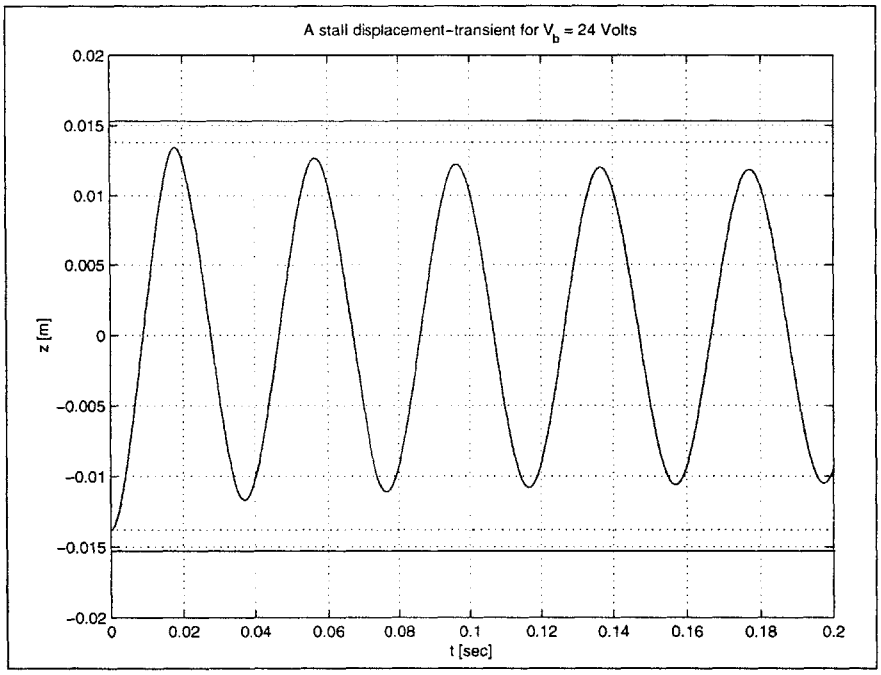

Figure 5-17: Typical displacement transient for $V_b = 24$ Volts ("stall"). Solid lines at $z = \pm 0.0153$ m indicate the positions of the left and right cylinder-heads, while the dashed lines at $z = \pm 0.0138$ m show the firing positions z_2 for this run

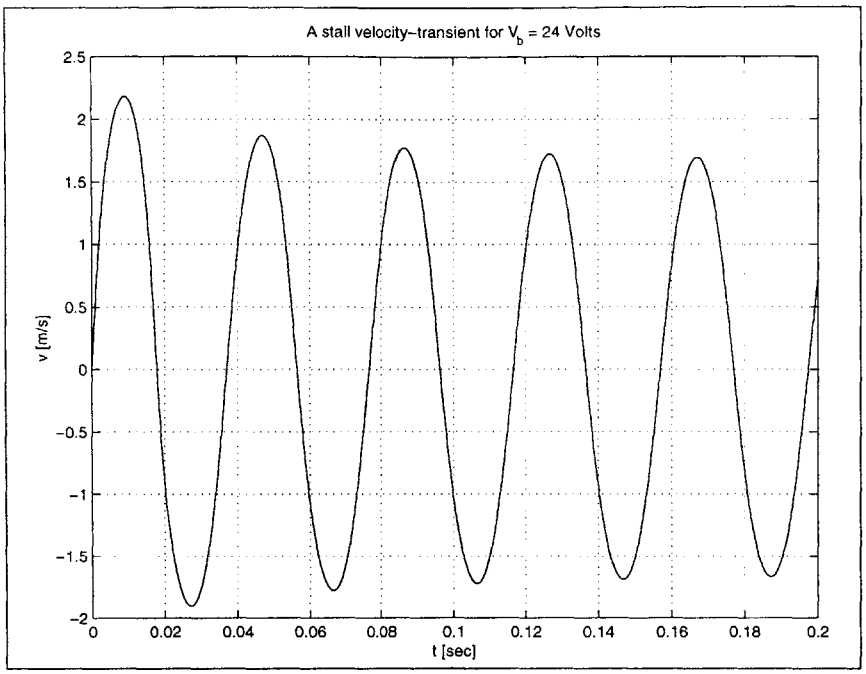

Figure 5-18: Typical velocity transient for $V_b = 24$ Volts ("stall")

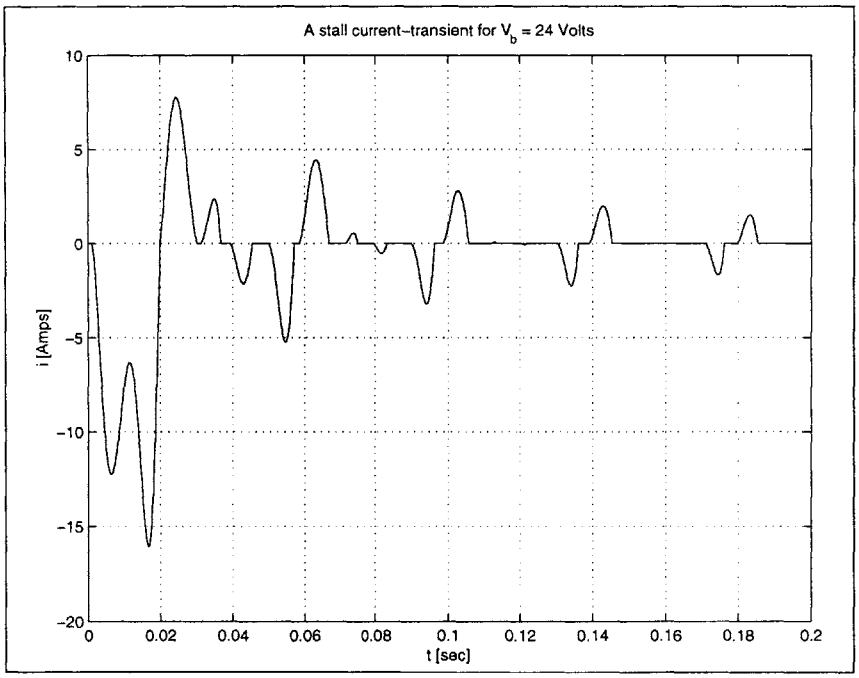

Figure 5-19: Typical current stall-transient for $V_b = 24$ Volts ("stall")

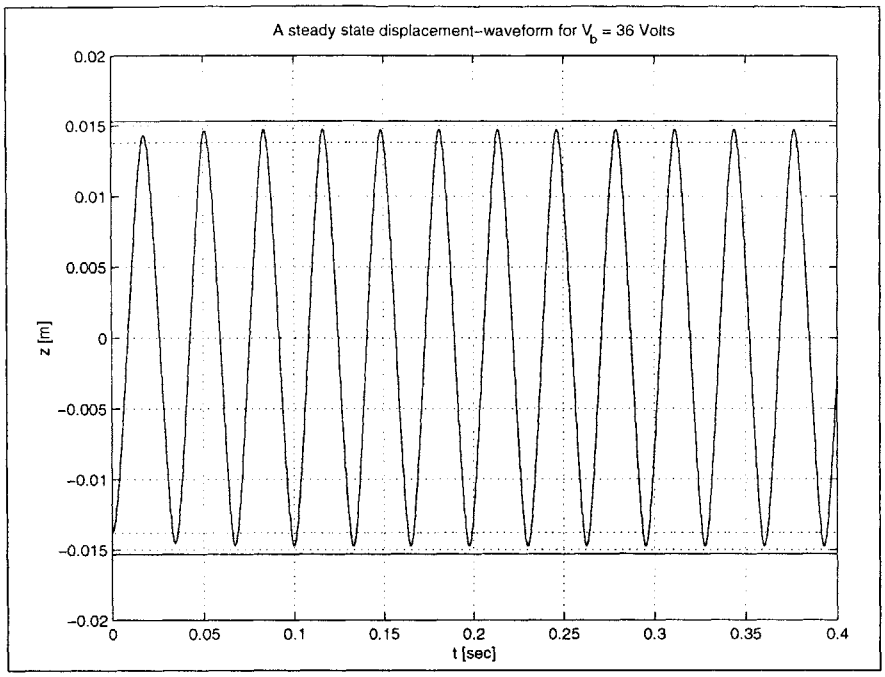

Figure 5-20: Typical steady-state displacement waveform for $V_b = 36$ Volts. Solid lines at $z = \pm 0.0153$ m indicate the positions of the left and right cylinder-heads, while the dashed lines at $z = \pm 0.0138$ m show the firing positions z_2 for this run

5.3.3 Steady-state operation

The simulation demonstrates that it is possible for the system to operate in the steady state for an intermediate range of battery voltages. Figures 5-20 through 5-22 show typical plots of the state variables for this operating regime. The battery voltage chosen for this representative run is 36 Volts.

Figure 5-20 shows the trajectory of the reciprocating assembly. Solid lines at $z = \pm 0.0153$ m indicate the positions of the left and right cylinder-heads, while the dashed lines at $z = \pm 0.0138$ m show the firing positions z_2 for this run.

Note from the figure that the position and velocity waveforms in Figures 5-20 and 5-21 are very sinusoidal considering the non-linearities in the system. However, the current waveform has significant third-harmonic content.

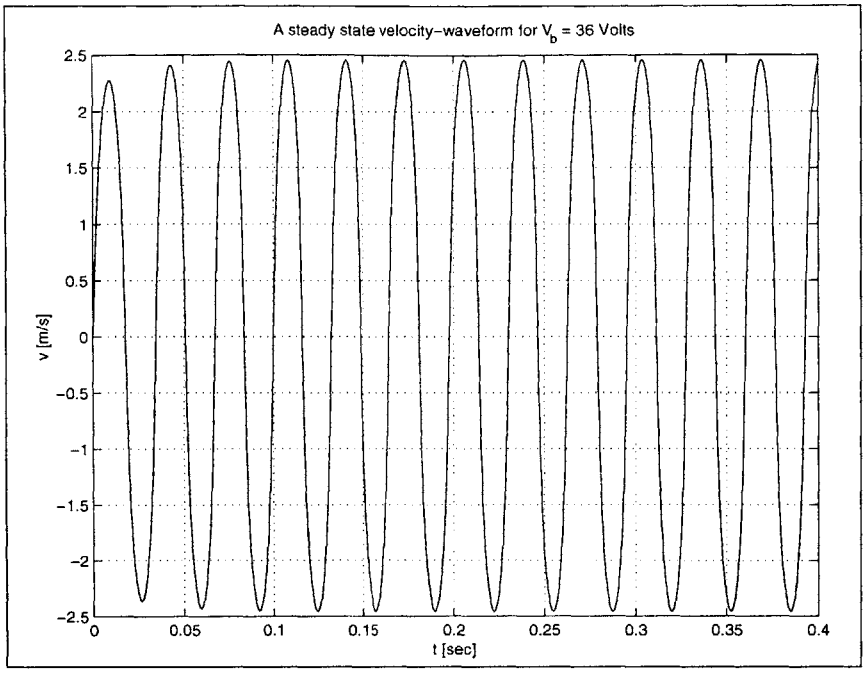

Figure 5-21: Typical steady-state velocity waveform for $V_b = 36$ Volts

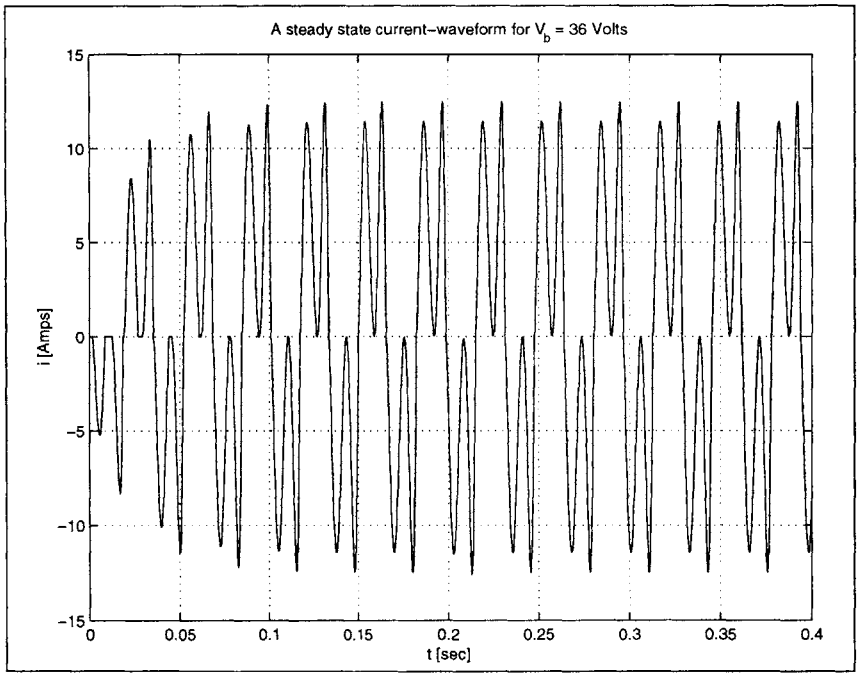

Figure 5-22: Typical steady-state current waveform for $V_b = 36$ Volts

5.4 Battery load operating-characteristics

A series of simulation runs show that the steady-state behavior in Section 5.3.3 manifests itself for a range of battery voltages and is relatively insensitive to small changes in the fixed simulation parameters. Figures 5-24 through 5-25 characterize the steady-state operation of the system for battery-charging operation.

Note that the linear relationship between the reciprocation frequency and the cycle-average electrical-power discussed in Section 5.2 still holds (see Figure 5-26). For $z_2 = 0.0138$ m the figure shows a slope of 7.52 W·s compared to the slope of 7.71 W·s predicted by Equation 5.5. For $z_2 = 0.0128$ m and $z_2 = 0.0118$ m the slopes shown on the figure are 6.82 W·s and 6.32 W·s, which are close to the predicted slopes of 7.02 W·s and 6.42 W·s. The errors are within engineering tolerance considering that the results in Figure 5-26 are based on 0.4 seconds of simulation time.

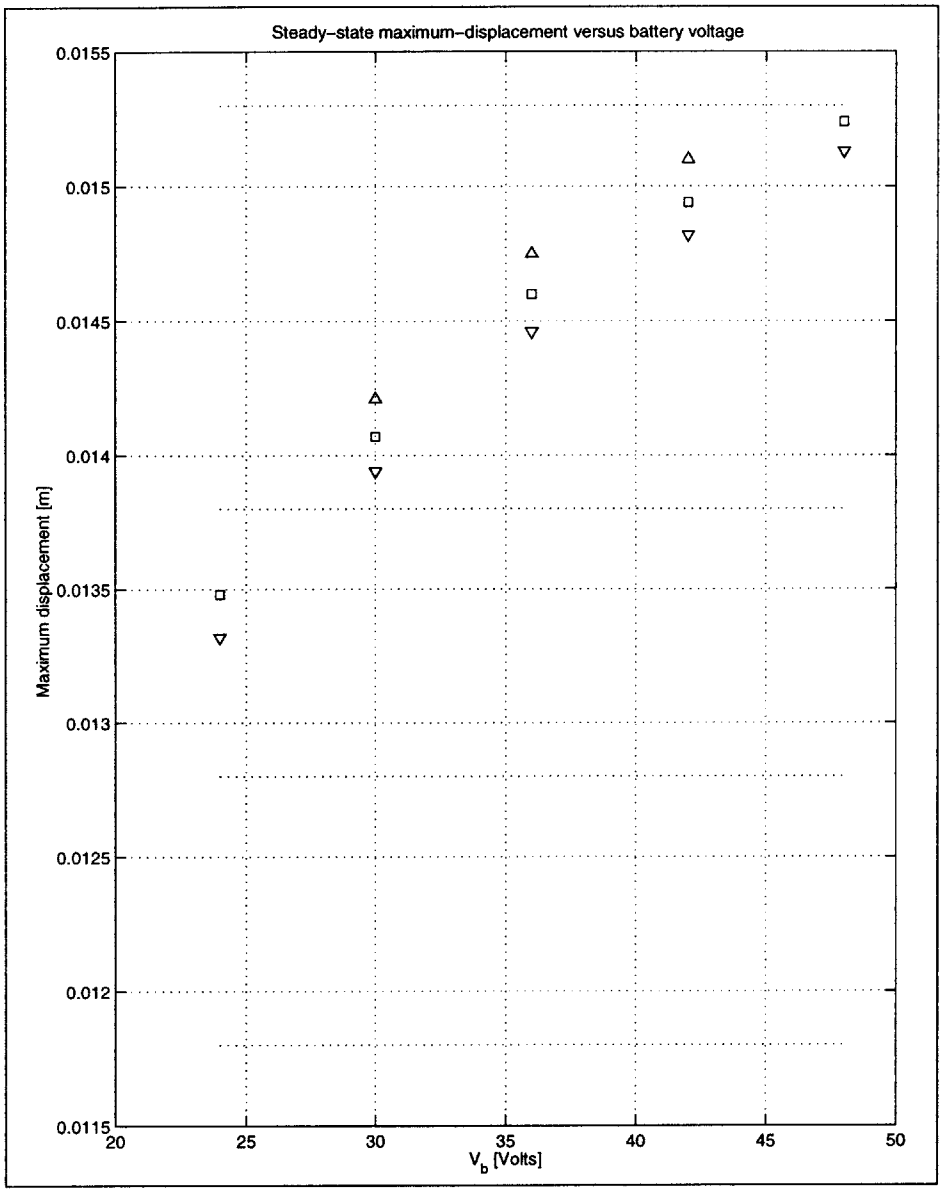

Figure 5-23: Characterization of the steady-state relationship between the maximum displacement and battery voltage for three firing positions: up triangles for $z_2 = 0.0138$ m, squares for $z_2 = 0.0128$ m and down triangles for $z_2 = 0.0118$ m

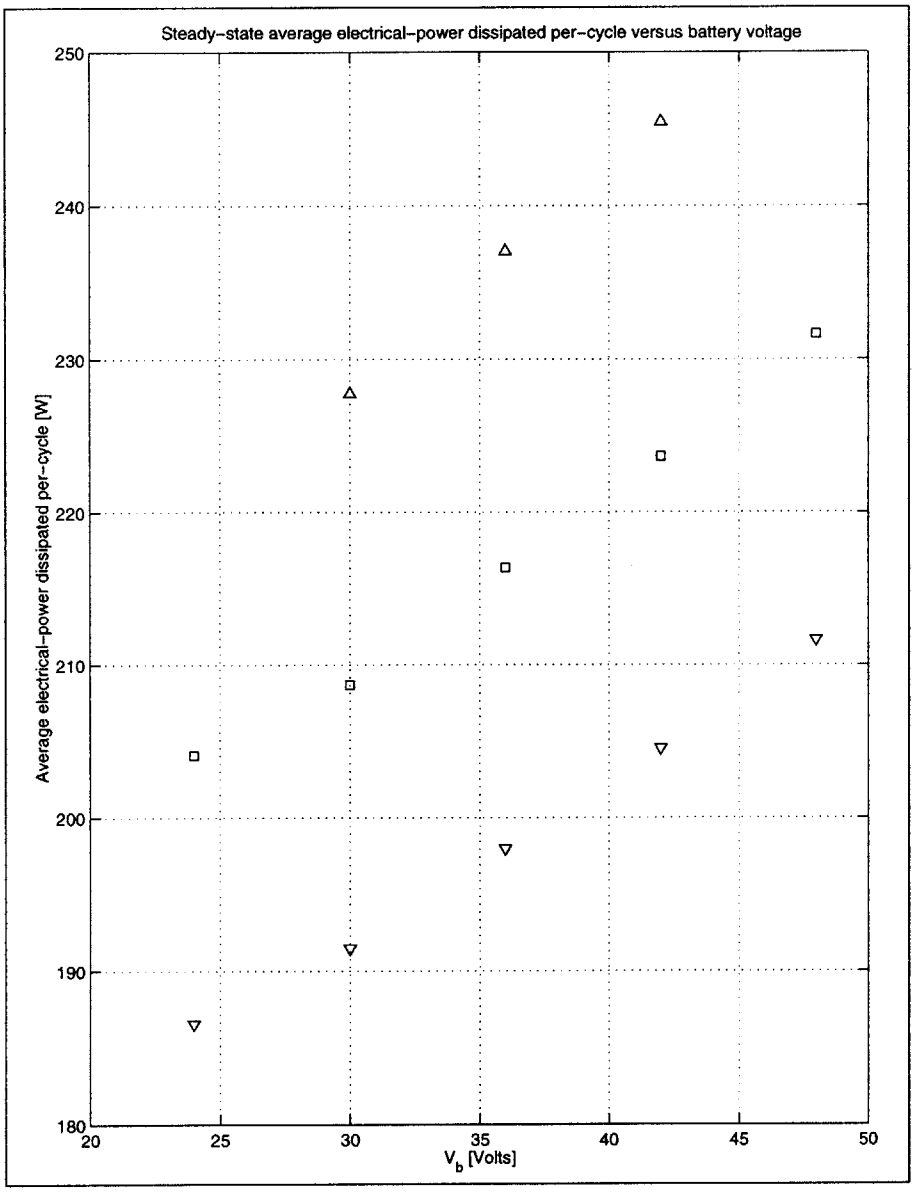

Figure 5-24: Characterization of the steady-state relationship between the cycle-average electrical-power and the battery voltage for three firing positions: up triangles for $z_2 = 0.0138$ m, squares for $z_2 = 0.0128$ m and down triangles for $z_2 = 0.0118$ m

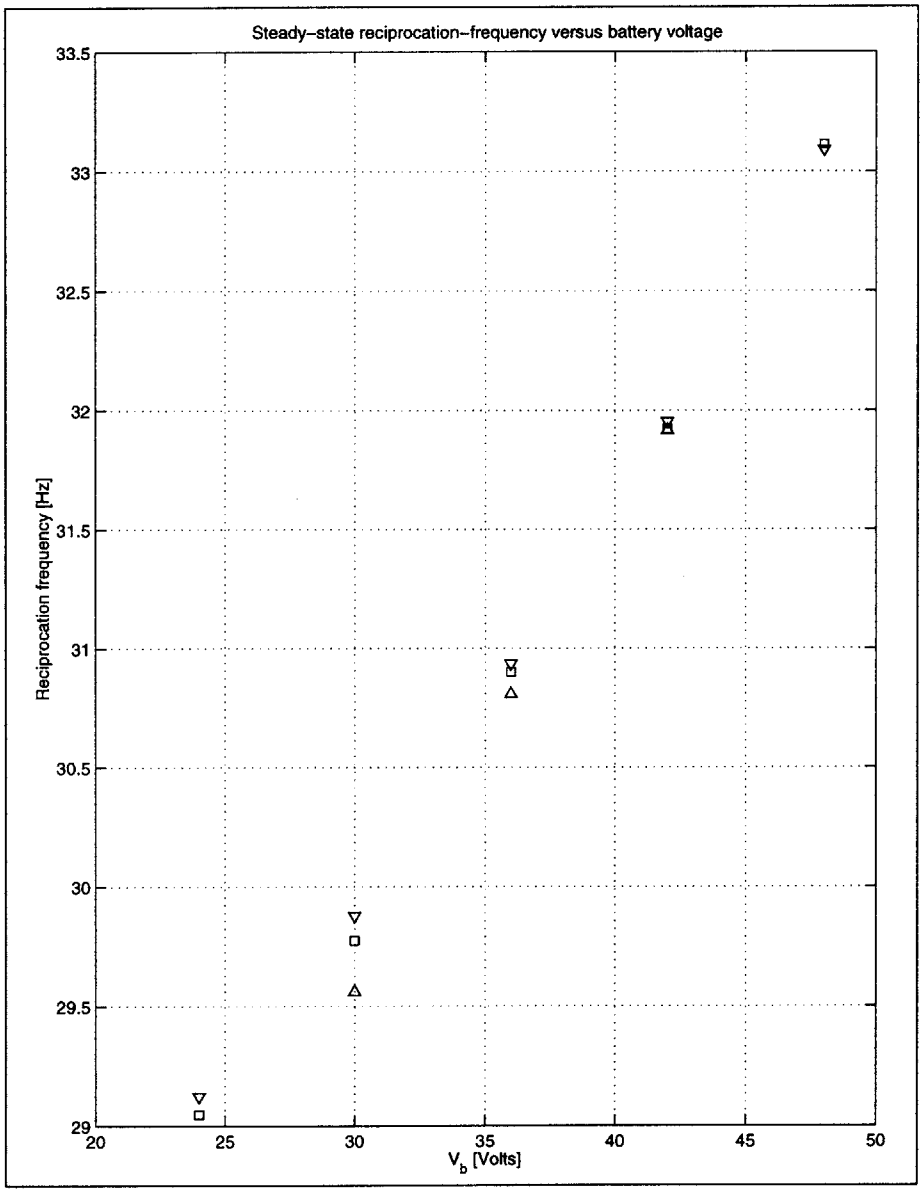

Figure 5-25: Characterization of the steady-state relationship between the reciprocation frequency and the battery voltage for three firing positions: up triangles for $z_2 = 0.0138$ m, squares for $z_2 = 0.0128$ m and down triangles for $z_2 = 0.0118$ m

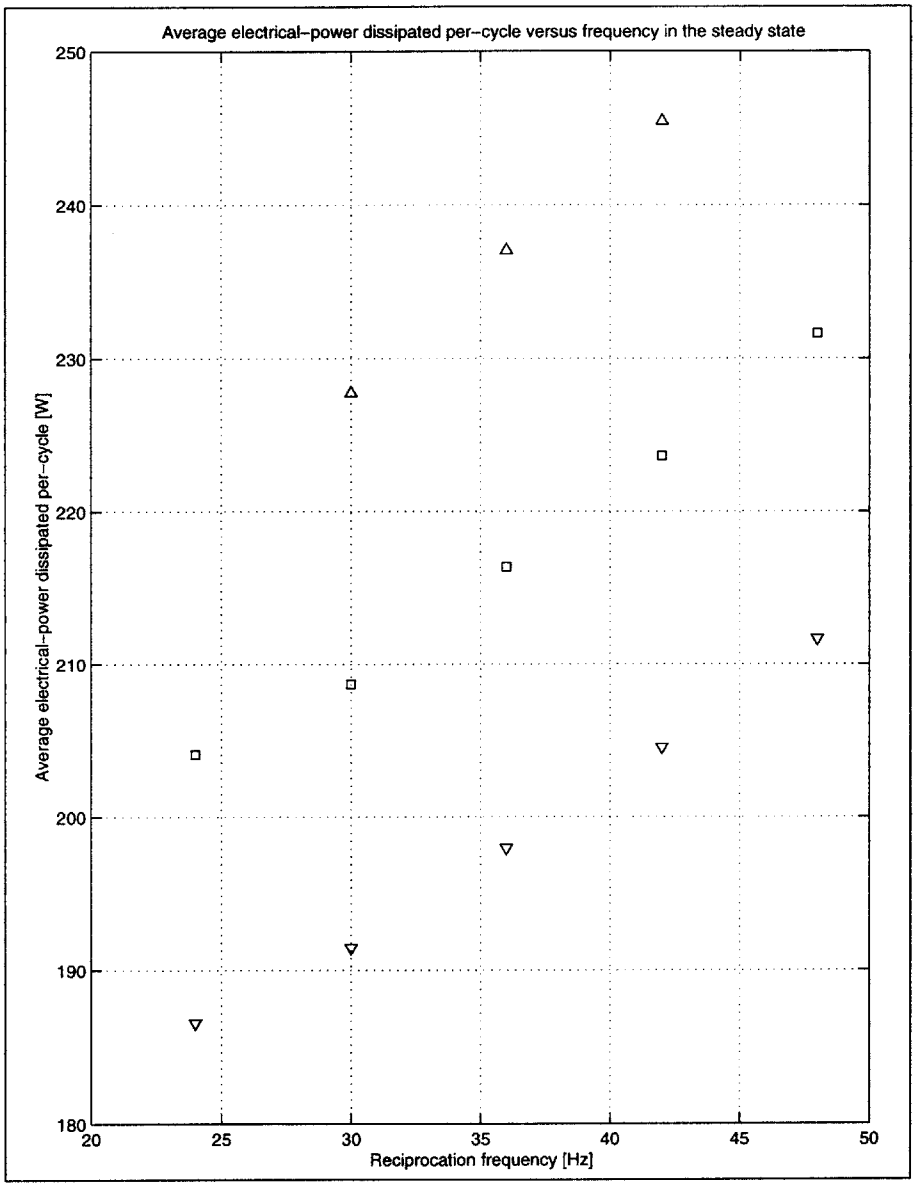

Figure 5-26: Characterization of the steady-state relationship between the cycle-average electrical-power and reciprocation frequency for three firing positions: up triangles for $z_2 = 0.0138$ m, squares for $z_2 = 0.0128$ m and down triangles for $z_2 = 0.0118$ m

Chapter 6

Preliminary experimental data

6.1 Experimental results

One objective of this thesis was to help Galileo Research design a control algorithm for their experimental free-piston-driven alternator system. The "self-stabilizing" operation discovered during the course of this thesis (see Chapter 5) was reported to Galileo Research and subsequently confirmed experimentally. This knowledge enabled them begin performing steady-state tests on the system. Although the testing performed to date has been limited, the results of two sets of experiments with a load resistance of 19 Ohms have been made available and will be discussed in this chapter.

For each of the test runs, the reported firing position was $z_2 = 0.0128$ m. The first run is reported to have lasted 17 minutes, which clearly demonstrates that the two-stroke, free-piston-engine driven linear-alternator can operate stably in the steady state. Unfortunately, only 30 seconds of pressure and position data from this run are available. The pressure versus position data from the first run presented in Figure 6-1 show that the pressure levels in the cylinders are lower than what one expects for a cylinder of this size[1]. The observed pressures are consistent with values of ΔQ_{23} much lower than 28 J.

Voltage, position and pressure data for a subsequent run were made available by

[1]Prof. J. L. Smith Jr., Private communication

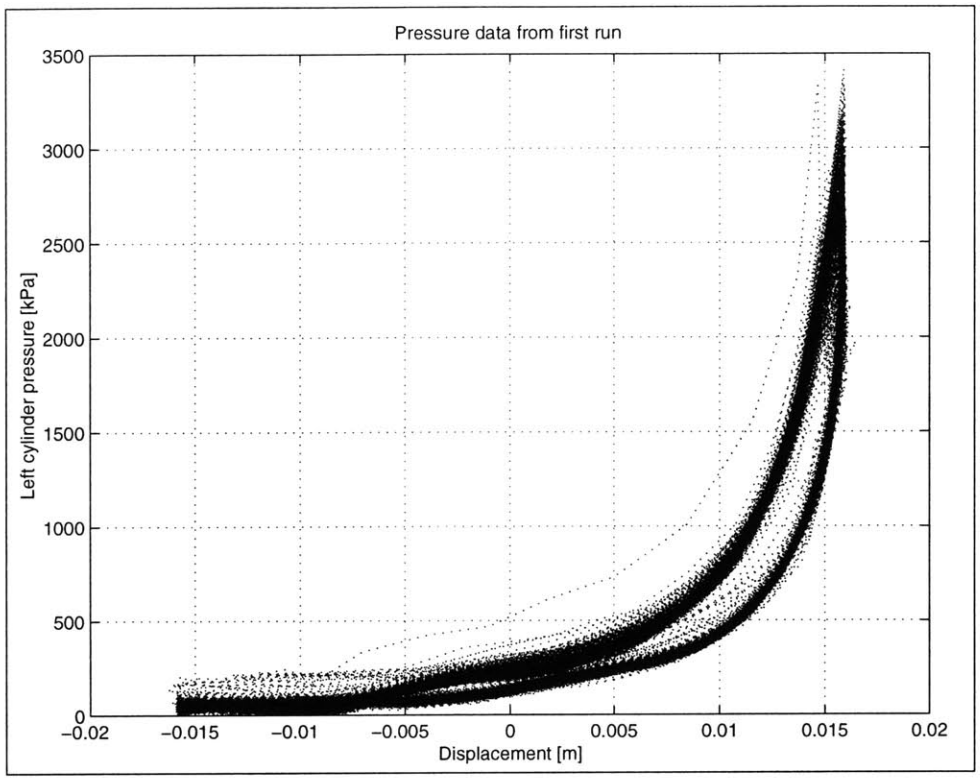

Figure 6-1: Pressure data from the first run

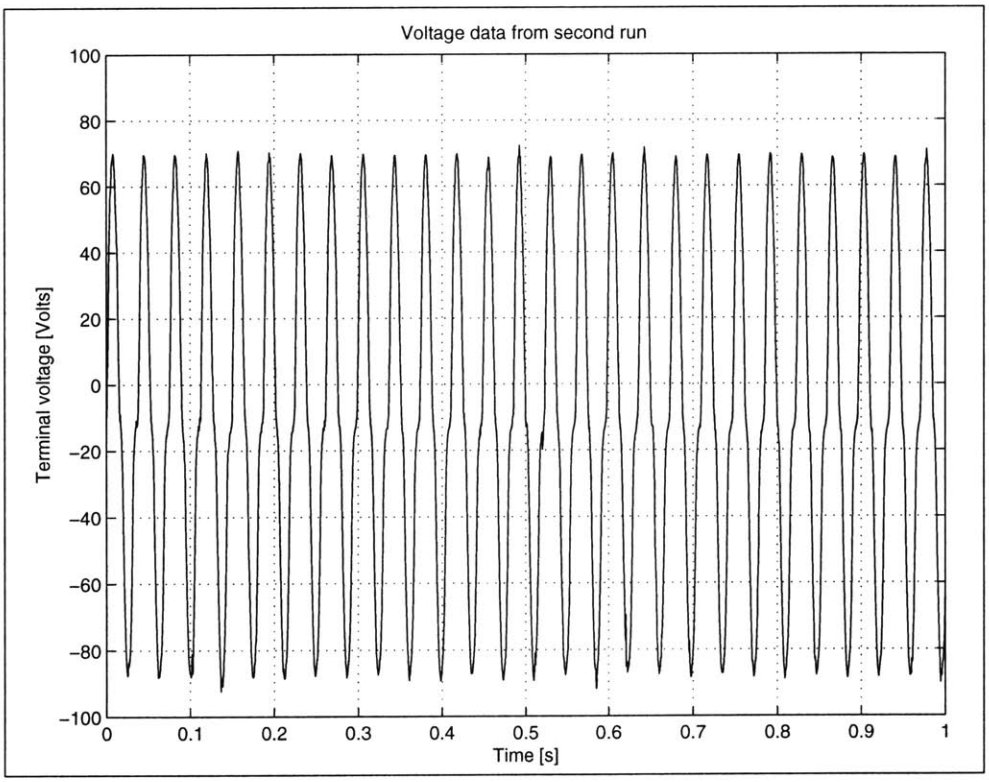

Figure 6-2: Voltage data from the second run

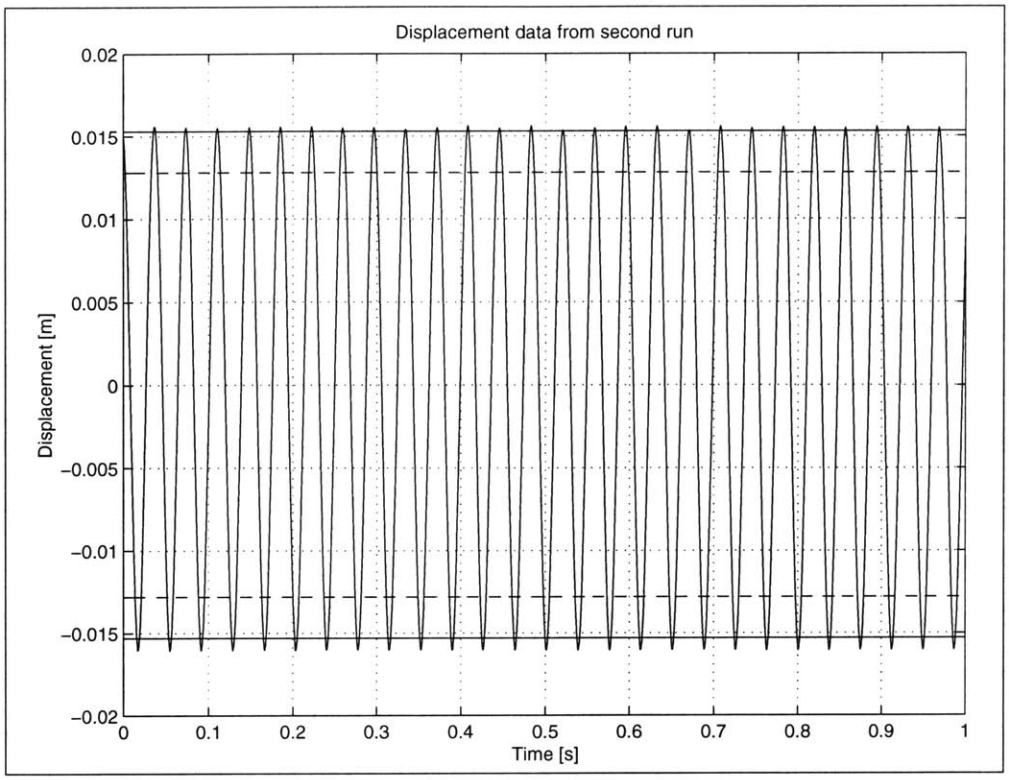

Figure 6-3: Displacement data from the second run. Solid lines at $z = \pm 0.0153$ m indicate the positions of the left and right cylinder-heads, while the dashed lines at $z = \pm 0.0128$ m show the firing positions for this run

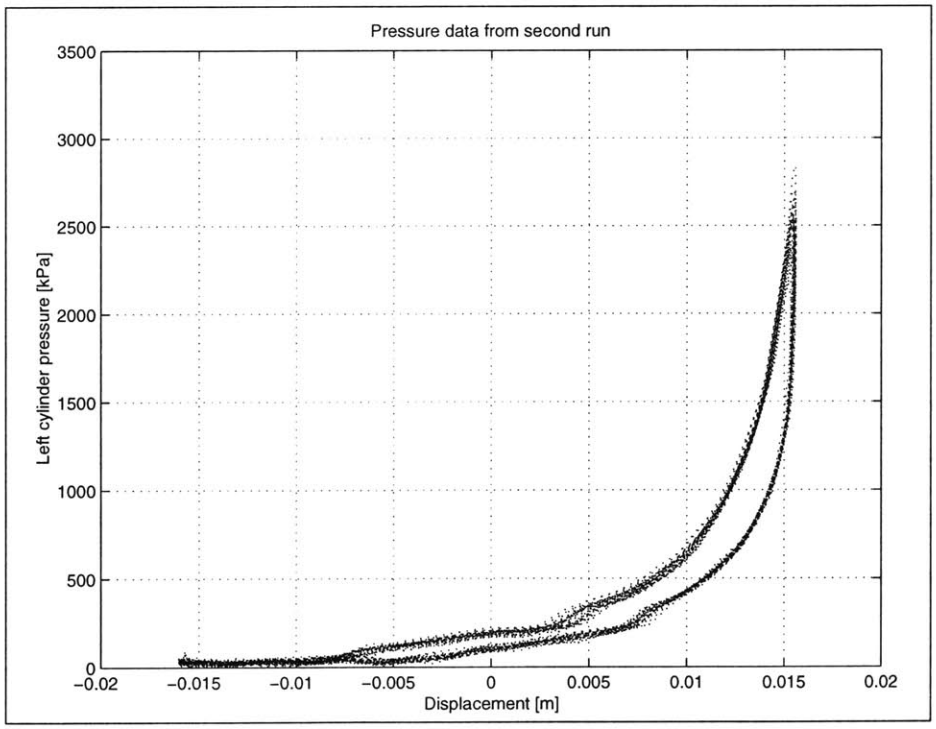

Figure 6-4: Pressure data from the second run

Galileo Research and are presented in Figures 6-2 through 6-4. The figures show that the reciprocating assembly has a frequency $f = 26.7$ Hz and an rms velocity $(v)_{rms} = 1.86$ m/s. The area enclosed by the pressure trajectory in Figure 6-4 corresponds to the fraction of combustion-heat input to the gas that gets converted into work each cycle, and hence $W_{cyc} = \eta \Delta Q_{23} = 2.96$ J. From Equation 3.43, the efficiency η for a firing position of $z_2 = 0.0128$ is 0.5, which means that ΔQ_{23} must be 5.9 J.

Note that the output voltage in Figure 6-2 has a DC offset of -10.6 Volts. This is clearly an error in the data acquisition-system since the alternator is an AC machine. The DC offset was subtracted from the data and the rms output-voltage was found to be $(e_o)_{rms} = 51.4$ Volts.

Note that the measured voltage waveform does not have as much third-harmonic content as predicted in Chapter 5. The data indicates that the simple analytical model of the internal voltage (see Equation 2.19) is more appropriate than the model based on a two-dimensional finite-element investigation (see Equation 2.52).

Figure 6-3 shows that the stroke of the reciprocating assembly is greater than the crash-to-crash distance. The figure also shows a slight negative offset in the displacement waveform. These effects are clearly unphysical since the piston cannot go through the cylinder head. The effects are probably due to sensor errors or an error in the shaft geometry supplied by Galileo Research.

The power delivered to the resistive load is given by,

$$< P_e^L >_{cyc} = \frac{(e_o)_{rms}^2}{R_L} \tag{6.1}$$

which for this set of data leads to $< P_e^L >_{cyc} = 146$ Watts. The rms current in the load $(i)_{rms}$ is given by the ratio of the rms terminal voltage $(e_o)_{rms}$ and the load resistance R_L. This enables us to calculate the cycle-average electrical power dissipated in the winding resistance as,

$$< P_e^w >_{cyc} = \frac{(e_o)_{rms}^2}{RL} \frac{R_w}{R_L} \tag{6.2}$$

which is 1.6 Watts for $R_w = 0.211$ Ohms.

The conservation of energy demands that the cycle-average power input from

the engine must equal the sum of the cycle-average electrical power delivered to the load, the cycle-average electrical power dissipated in the alternator and the cycle-average mechanical power dissipated in the engine. Hence we can write the following expression for the cycle-average power,

$$2\eta\Delta Q_{23} f = < P_e^L >_{cyc} + < P_e^w >_{cyc} + < P_m^d >_{cyc} \tag{6.3}$$

where P_m^d is the dissipated mechanical power. This means that mechanical losses must account for 11 Watts in each cycle.

Equation 6.3 can be used to estimate the damping coefficient B (discussed in Section 3.7). The cycle-average power dissipated in a linear damper is given by,

$$< P_m^d >_{cyc} = \frac{1}{T}\int_0^T f_d v dt = \frac{1}{T}\int_0^T B v^2 dt \tag{6.4}$$

which results in the following expression for B,

$$B = \frac{< P_m^d >_{cyc}}{(v)_{rms}} \tag{6.5}$$

After substitution, we find that $B = 6$ kg/s.

6.2 Simulation

To compare the predictions of the numerical simulation with the empirical results, the simulation was run with the following parameters,

- Firing position $z_2 = 0.0128$ m as reported by Galileo Research
- Load resistance $R_L = 19$ Ohms as reported by Galileo Research
- The internal-voltage model of Equation 2.19 was used (i.e., $e_{af} = (30.9)v$ Volts)
- The corresponding model for the force of electric origin was used (i.e., $f_e = (30.9)i$ Newtons)

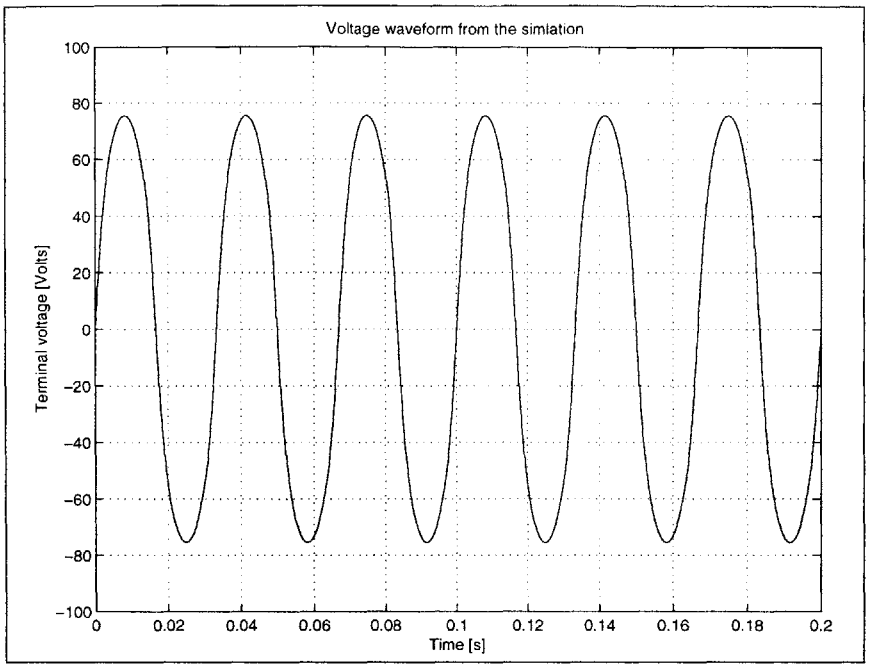

Figure 6-5: Voltage waveform from the simulation

- Combustion heat input $\Delta Q_{23} = 5.9$ J as derived from the data in Section 6.1
- Damping coefficient $B = 6$ kg/s as derived from the data in Section 6.1

Note that the results of the two-dimensional finite-element investigation of Section 2.3.2 have been abandoned in favor of the analytical linear-relationship, since the voltage data indicates that the analytical expression is more appropriate. A three dimensional analysis as well as additional measurements on the alternator should be conducted to resolve the discrepancy between the experimental data and the two-dimensional finite-element investigation.

Figure 6-6 shows the predicted voltage waveform, which has an rms value of 58.1 Volts, which is 13% higher than the measured value of 51.4 Volts. Figure 6-6 shows the trajectory of the reciprocating assembly, where solid lines at $z = \pm 0.0153$ m denote the positions of the left and right cylinder-heads, while the dashed lines at $z = \pm 0.0128$ m show the firing positions for this run. The frequency of reciprocation is predicted to be 30.1 Hz which is 13% greater than the measured value of 26.7 Hz. Figure 6-7 shows the predicted pressure trajectory.

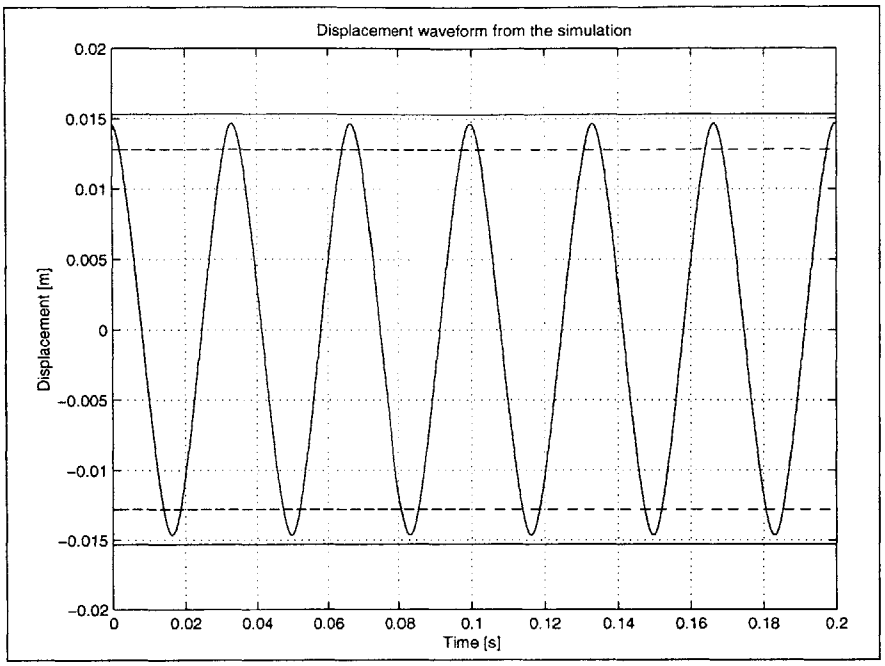

Figure 6-6: Displacement waveform from the simulation. Solid lines at $z = \pm 0.0153$ m indicate the positions of the left and right cylinder-heads, while the dashed lines at $z = \pm 0.0128$ m show the firing positions for this run

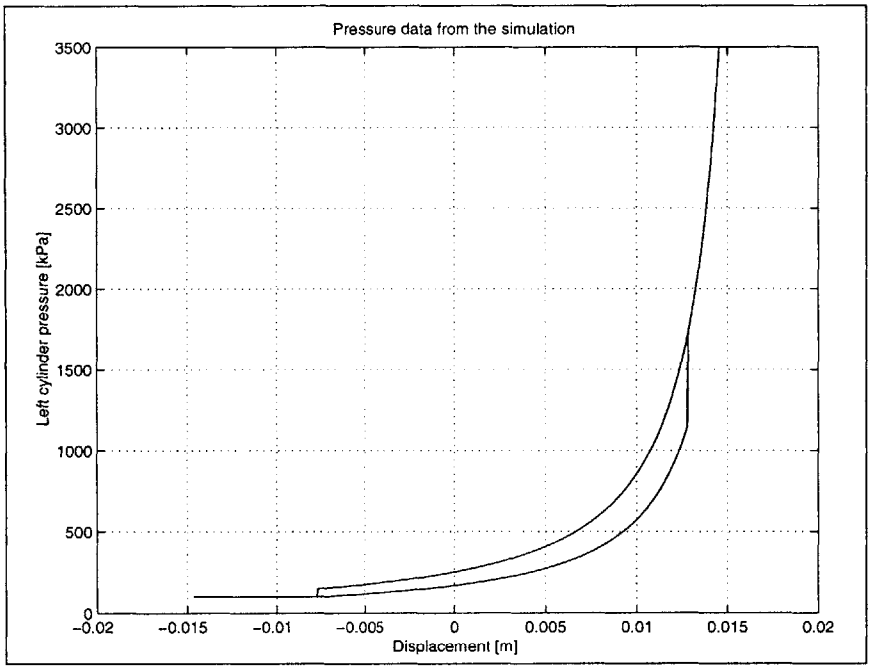

Figure 6-7: Pressure waveform from the simulation

Comparing the results of the simulation to the preliminary experimental data provided by Galileo Research verifies the validity of the system model developed for this thesis. The model clearly captures the essential physics and dynamics of the two-stroke, free-piston-engine driven linear-alternator. In addition, the model is reasonably good at predicting the frequency, power, output voltage and cylinder pressure levels of the experimental prototype. Further model refinement was not possible during the course of this thesis due to inaccessibility of the prototype system. Such refinement would most definitely be a logical next step in this work.

Chapter 7

Conclusions

7.1 Overview

Models for each of the three major components of the system were developed and then tied together into an overall system-model. The system model was formulated as a set of non-linear dynamic equations in three state variables. A numerical differential-equation solver was implemented in C-code to simulate the system dynamics. This program was subsequently used to conduct a detailed investigation of the dynamic behavior of the two-stroke, free-piston-engine driven linear-alternator. The results of the investigation are presented in Chapter 5.

The "self-stabilizing" operation documented in Chapter 5 was reported to Galileo Research and subsequently confirmed experimentally. The predictions of the numerical simulation have enabled Galileo Research to commence steady-state testing on their experimental prototype.

Preliminary data from the prototype confirms the validity of the modeling approach. However, the complete empirical investigation needed to thoroughly validate and refine the models had not been conducted by Galileo Research at the time of the writing of this thesis.

7.2 Findings and conclusions

When viewed as a whole, the simulations discussed in Chapter 5 demonstrate the existence of a range of resistive and battery-charging loads for which steady-state operation is possible without the aid of feedback-control. Within this range the system was observed to converge on a stable operating point through the interaction of the following mechanisms:

- Variations in the reciprocation frequency. This is the primary effect, since both the mechanical power input by the engine and the electrical power extracted by the alternator depend on the reciprocation frequency.
- Variations in the stroke. The terminal voltage depends on the velocity of the reciprocating assembly, which in turn is determined by both the frequency and the stroke.

In addition, the results clearly show that the maximum power the system under consideration is capable of delivering is not determined by the power-rating of the individual components. The combined dynamics of the engine, alternator and load determine the power transfered from the engine to the load. This issue manifests itself in the prototype built by Galileo Research, where both the engine and the alternator are each separately rated for a 1000 Watt operation. The simulations indicate that it will not be possible to extract more than 300 Watts of output power from the current prototype.

7.3 Recommendations for future work

The engine model developed for this thesis is very idealized and ignores many significant details of two-stroke-engine thermodynamics. In particular the details of the combustion process determine the heat transfered to the gas at combustion, which has been demonstrated to be significant in determining the stability and performance of the system. In order to confirm that the results and conclusions of this modeling effort are valid, the engine model needs to be replaced with a more realistic model.

The alternator model should be further refined. A combination of measurements and a three-dimensional analysis is necessary to reconcile the experimental data and the results of a two-dimensional investigation.

The system model has not yet been thoroughly investigated experimentally and stands to benefit greatly from an empirical investigation. Empirical data is needed to model the mechanical losses ignored in this modeling effort and refine both the engine and alternator models.

Once these modification have been incorporated into the system model, the computer program embodying the simulation of the two-stroke, free-piston-engine driven linear-alternator can serve as design tool for a new prototype capable of delivering the targeted 1000 Watts of output-power.

Appendix A

C-code

A.1 sim2n1.c

```
/*************************************************/
/*              Numeric simulation of            */
/*              A Two-Stroke,                    */
/*              Free-Piston-Engine               */
/*              Driven Linear                    */
/*              Alternator                       */
/*                                               */
/*              Master's Thesis                  */
/*              MIT, EECS                        */
/*              1999-2000                        */
/*                                               */
/*              STOP and GO driver               */
/*              For constant step size           */
/*              4th order Runge-Kutta           */
/*                                               */
/*              MIT Electromechanical            */
/*              Systems Laboratory               */
/*                                               */
```

```
/*              Shihab M. Elborai                */
/*************************************************/
/*
/* This code is based in part on the Runge-Kutta algorithm found
/* in the book Numercal Recipes in C
/*    ---------------------
/*
/* 16/09/99 Scavanged pieces from new1.c
/* 24/09/99 Model runs
/* 29/09/99 Modified derived mechanical variables
/* 01/10/99 keeps track of power
/* 19/10/99 keeps track of frequency, and pressure
/* 08/12/99 Fixed up the geometry of the cylinder, added V_dead
/* 07/02/00 Fixed error in stator geometry...tm and tg values doubled
/* 21/03/00 Added q3, q2, q1 from finite-element model for the internal voltage
/* Last modified: 21/3/2000
*/

#include <stdio.h>
#include <math.h>
#include <time.h>
#include "nrutil.h"

#define NVAR 6 /*Number of colmns in output matrix*/
#define MAX 1333334 /*Maximum allocated memory*/
#define PI 3.14159
#define MUEo 1.25664e-6 /*The permeability of free space*/

// Run-time memory
double **yy,/*Memory for state variables*/
```

```
*tt; /*and for the coressponding time*/

// Diagnostic variables
double fgas=0.0,/*Force due to Left and right pocket*/
/*Pressure difference*/
t_fire=0.0,/*Time when combustion event occured*/
L_cyl_pressure=0.0,/*The pressure in the left cylinder */
power; /*Instantanous electrical power*/

// Electrical load parameters

// Resistive load
double
R_load;
// Full-wave rectifier and battery
double V_batry,/*The voltage of a battery load*/
R_batry,/*The internal resistance of the battery*/
V_diode; /*Diode drop (not implemented)*/

int BRIDGEstate; /*State of the full-wave bridge*/
int CRASHflag; /*Crashed into cylinder head*/

// Electro-mechanical parameters
double Rw,/*Winding resistance*/
Lw,/*Winding inductance*/
/*Speed-voltage coeffecients*/
q1,//First order
q2,//Second order
q3; //Third order
```

```
// Geometry of the Star-alternator
double wm,/*Width of a magnet*/
tm,/*Thickness of a magnet*/
lm,/*Length of a magnet*/
tg,/*Thickness of the air gap*/
wi; /*Half the width of a pole piece*/

double Ncoils,/*Number of coils*/
Br; /*Residual flux density*/

// Thermodynamic parameters
double KC,/*Ratio of the pressures after and before combustion*/
gama,/*Unitless property of an ideal gas*/
dQ23; /*Esitmate of the heat input to the gas at combustion*/

double D_piston,/*Piston diameter*/
A,/*Cylinder cross-sectional area*/
p1,/*Atmospheric pressure*/
p2; /*Pressure just before combustion*/

double clearance,/*Minimum firing cylinder head to piston distance*/
z1,/*Location of exhaust port*/
z2,/*Firing position*/
ycc; /*Half the crash-to-crash-distance*/

double V1,/*Maximum compressed volume*/
V2min,/*Minimum compressed volume*/
Vdead,/*Dead volume*/
Y1; /*piston-head distance when volume is V1*/
```

```
int UPPERleg; /*Flag to implement hysterisis in the gas force*/

// Mechanical parameters
double M,/*Mass of moving assembly*/
K,/*Spring constant*/
B; /*Lumped mechanical losses*/



/*static memory allocation tricks*/
static double *dym = NULL;
static double *dytemp = NULL;
static double *ytemp  = NULL;
/*prepare some static memory for Runge-Kutta*/
void rk4_ini(int n)
{
   dym=dvector(1,n);
   dytemp=dvector(1,n);
   ytemp=dvector(1,n);
}
/*after youre done cleanup that memory*/
void rk4_fini()
{
   free_dvector(dym,1);
   free_dvector(dytemp,1);
   free_dvector(ytemp, 1);
}


/*************************** Runge Kutta *********************************/
```

```
int rk4(double y[], double dydt[], int n, double t,
                  double h, double yout[],
                  void (*derivs) (double, double [], double []))
{
int i;
double th,hh,h6;
hh=h*0.5;
h6=h/6.0;
th=t+hh;
for (i=1;i<=n;i++) ytemp[i]=y[i]+hh*dydt[i];
(*derivs)(th,ytemp,dytemp);
for (i=1;i<=n;i++) ytemp[i]=y[i]+hh*dytemp[i];
(*derivs)(th,ytemp,dym);
for (i=1;i<=n;i++) {
ytemp[i]=y[i]+h*dym[i];
dym[i] += dytemp[i];
}
(*derivs)(t+h,ytemp,dytemp);
for (i=1;i<=n;i++){yout[i]=y[i]+h6*(dydt[i]+dytemp[i]+2.0*dym[i]);}
if(BRIDGEstate  == 2){
yout[3] = 0;
}
return 0;
}


/****************************** Stepper ******************************/
void rkdumb(double vstart[],int nvar,double t1, double t2,double h,
void (*derivs)(double, double [], double []))
```

```
{
int i,k,nstep;
double t;
double *v,*vout,*deriv;

v=dvector(1,nvar);
vout=dvector(1,nvar);
deriv=dvector(1,nvar);
for (i=1;i<=nvar;i++) {
v[i]= vstart[i];
yy[i][1]=v[i];
}
yy[5][1]=0;
yy[6][1]=0;

tt[1]=t1;
t=t1;

nstep=(int)((t2-t1)/h);
printf("%d\n",nstep);
rk4_ini(nvar);
for (k=1;k<=nstep;k++)
{
(*derivs)(t,v,deriv);
rk4(v,deriv,nvar,t,h,vout,derivs);
if (fabs(v[1]) >= ycc) {
 CRASHflag = 1;
 printf("\n\nBOOM!CRASH!BANG!\n\n");
exit(0);
}
```

```
if ((double) (t+h) == t) {
nrerror("Step size too small in routine rkdumb");
}
t += h;
tt[(k)+1]=t;
for (i=1;i<=nvar;i++) {
v[i]=vout[i];
yy[i][(k)+1]=v[i];
}
yy[4][(k)+1]=power;
yy[5][(k)+1]=L_cyl_pressure;
yy[6][(k)+1]=t_fire;
}
rk4_fini();
free_dvector(deriv,1);
free_dvector(vout,1);
free_dvector(v,1);
}
```

```
/****************************** Subroutines ********************************/
/******************************** Fgas *************************************/
double Fgas(double z, double t)
{
double Force;
double res;
res = .00000075 ;
/*determine which leg of the force-position curve to use*/
if(UPPERleg)
```

```
{
if(((z2-z)<=res)&&((z2-z)>=0))
{
UPPERleg = 0;
t_fire=t;
}
}
else
{
if(((z2+z)<=res)&&((z2+z)>=0))
{
UPPERleg = 1;
t_fire=t;
}
}

/*Then calculate the force given the current leg*/
if (UPPERleg)
{
if(fabs(z)<=z1) {
Force = A*p1*(KC*pow((V1/(A*(ycc+z)+Vdead)),gama)
      - pow((V1/(A*(ycc-z)+Vdead)),gama));
L_cyl_pressure = p1*KC*pow((V1/(A*(ycc+z)+Vdead)),gama);
}
else if(z > z1) {
Force = A*p1*( 1 - pow((V1/(A*(ycc-z)+Vdead)),gama));
L_cyl_pressure = p1;
}
else {
Force =  A*p1*(KC*pow((V1/(A*(ycc+z)+Vdead)),gama) - 1);
```

```
L_cyl_pressure = p1*KC*pow((V1/(A*(ycc+z)+Vdead)),gama);
}

}
else
{
if(fabs(z)<=z1) {
Force = A*p1*(pow((V1/(A*(ycc+z)+Vdead)),gama)
      - KC*pow((V1/(A*(ycc-z)+Vdead)),gama));
L_cyl_pressure = p1*pow((V1/(A*(ycc+z)+Vdead)),gama);
}

else if(z<-z1)  {
Force =  A*p1*( pow((V1/(A*(ycc+z)+Vdead)),gama) - 1);
L_cyl_pressure =  p1*pow((V1/(A*(ycc+z)+Vdead)),gama);
}

else {
Force =  A*p1*(1 - KC*pow((V1/(A*(ycc-z)+Vdead)),gama));
L_cyl_pressure = p1;
}
}
return(Force);
}


/*************************** Equations ************************************/
void derivs(double t,double y[],double dydt[])
{
/*figure out the state of the diode bridge*/
```

```
/*On:D1,D2  Off:D3,D4*/
if(BRIDGEstate  ==1){
if(y[3]>0) {
BRIDGEstate  = 2;
}
}

/*Off: D1,D2,D3,D4*/
if(BRIDGEstate  ==2){
if(q3*y[1]*y[1]*y[2]+q2*y[1]*y[2]+q1*y[2]>V_batry){
BRIDGEstate  =1;
}
else if(q3*y[1]*y[1]*y[2]+q2*y[1]*y[2]+q1*y[2]<-V_batry){
BRIDGEstate  =3;
}
}

/*On:D3,D4 Off:D1,D2*/
if(BRIDGEstate  ==3){
if(y[3]<0){
BRIDGEstate  =2;
}
}

/*The dynamic equations*/
fgas = Fgas(y[1],t);

dydt[1] = y[2];
dydt[2] = (1/(M))*(q3*y[1]*y[1]*y[3]+q2*y[1]*y[3]+q1*y[3]+fgas-K*y[1]);
```

```
/*The electrical dynamics depend on the state of the bridge*/
if(BRIDGEstate ==1){
dydt[3]= -(1/Lw)*(q3*y[1]*y[1]*y[2]+q2*y[1]*y[2]+q1*y[2]+(Rw+R_batry)*y[3]-V_batry)
power = -V_batry*y[3]+y[3]*y[3]*(Rw+R_batry);
}

if(BRIDGEstate  ==2){
dydt[3]= 0.0;
power=0.0;
}

if(BRIDGEstate  ==3){
dydt[3]= -(1/Lw)*(q3*y[1]*y[1]*y[2]+q2*y[1]*y[2]+q1*y[2]+(Rw+R_batry)*y[3]+V_batry)
power = V_batry*y[3]+y[3]*y[3]*(Rw+R_batry);
}

}



/****************************** Main ************************************/

void main()
{
// misc.
FILE *ofp1;
    int i;
int kount;
double t1,t2,h,*vstart;
```

```
// Electrical load parameters
/**/
V_batry =  0.000;   //[V]
R_batry =  19.0;   //[Ohm]
V_diode =  0.0;      // [V]
R_load  =  0.0;      // [Ohm]
/**/

// Geometry of the STAR-alternator
wm = 0.02794; // magnet width [m]
tm = 0.02250; // magnet thickness [m]
lm = 0.02540; // magnet length [m]
tg = 0.00158; // air-gap thickness [m]
wi = 0.0127 ; // stator-arm width [m]
Ncoils = 63; // number of coils on one stator arm
Br = 1.25; // residual magnetization [T]


// Electro model parameters

Lw = 7.19e-3;
        //(1.0)*(8*4*(Ncoils*Ncoils)*MUEo*wm*lm/(tm+(2*tg)));
        // Winding inductance [H]

        Rw=  0.211; // Winding resistance [Ohm]

q1 = 30.87;//1*8*Ncoils*(0.0118);
/*The linear model for internal voltage is used*/
q2 = 2*8*Ncoils*(0.0);// must be zero! flux-position has odd symmetry!
q3 = (0)*3*8*Ncoils*(152.8);//disabled the cubic fit
```

```
// Thermodynamic model parameters
D_piston  =  0.0350;                  // piston diameter [m]
clearance =  0.0015;                  // clearance in meters [m]
Y1        =  0.0230;                 // y coordinate of exhaust port [m]
Vdead   =  1.8e-6;                  // spark plug cavity 2 ml [m^3]
A   =  (D_piston*D_piston)*PI/4;  // cylinder cross-sectional area [m^2]
p1   =  1.01e5; // atmospheric-pressure [Pa]
gama   =  1.4; // property of an ideal gas [-]
V1   =  A*Y1+Vdead; // maximum compressed volume [m^3]
V2min   =  A*clearance+Vdead;     // clearanace and cavity [m^3]

/**/
dQ23   =  5.92; // pow(V1,gama)*p1*(2.5)/((gama-1)*pow(V2min,(gama-1)));
/**/

ycc   = 0.0153;             /*half of crash-to-crash [m]*/
z1   = Y1-ycc;     /*+- exhaust port z-location [m]*/

/**/
z2   = 0.0128;    /*spark fires at +- this positon [m]*/
/**/

KC = 1+(gama-1)*dQ23*pow(A*(ycc-z2)+Vdead,(gama-1))/(p1*pow(V1,gama)); /*[-]*/


//Mechanical constraints
M = 6.404;          // Reciprocating mass [kg]
```

```
K = 9.516e4;        // Flexture spring const [kg/s^2]
B = 6.17;           // Linear damper coeffecient [kg/s]

//Runge-Kutta runtime memory
vstart=dvector(1,NVAR);
tt=dvector(1,MAX);
yy=dmatrix(1,NVAR,1,MAX);

//Start simulation from the time
t1=0.0;
//until the time
t2=0.2;
//with step size
h=.00000015;
//this means you take this many steps
kount=(int)((t2-t1)/h);



/*Initialize flags
*/
UPPERleg = 0; //gas force hysterysis flag
BRIDGEstate = 3; //full-wave bridge topology flag
/*
*/
/* Initial Conditions
*/
vstart[1]= /**/ -1.00*z2; /* displacement from center in m  */
vstart[2]= /**/  0.0;     /* velocity in m/s   */
vstart[3]= /**/  0.0;     /* current in the winding in Amps */
```

```
/*
*/
/********************** call runge-kutta ********************************/
printf("Calling Runge-Kutta...\n");
rkdumb(vstart,NVAR,t1,t2,h,derivs);
printf("...Done calling Runge-Kutta\n");

/********************** Output summary ******************************/
/*Display all the info regarding this run*/
printf("\n\nInput parameters:\n");
printf("_________________\n");

printf("V_batry = %5.4g,R_batry = %6.4g,V_diode = %6.4g\n",V_batry,R_batry,V_diode)
printf("R_load  = %5.4g                                          \n", R_load);
printf("wm      = %5.4g,  tm      = %6.4g,  tg      = %6.4g  \n", wm,tm,tg);
printf("lm      = %5.4g                                          \n", lm);
printf("wi = %5.4g,  Ncoils  = %6.4g,  Br= %6.4g\n", wi, Ncoils, Br);

printf("Lw = %5.4g,  q2 = %6.4g,  Rw= %6.4g\n", Lw, q2, Rw);

printf("D_piston= %5.4g,clearance=%6.4g,Y1= %6.4g \n", D_piston, clearance, Y1);
printf("V1      = %5.4e,  V2min   = %6.4e,  dQ23   = %6.4g\n", V1, V2min, dQ23);
printf("Vdead   = %5.4e \n", Vdead);
printf("A       = %5.4e,  p1    = %6.4e,  gama    = %6.4g  \n", A, p1, gama);
printf("ycc     = %5.4g,  z1    = %6.4g,  z2      = %6.4g\n", ycc, z1, z2);
printf("KC      = %5.4g \n", KC);

printf("M = %5.4g,  K    = %6.4e,  B       = %6.4g\n", M, K, B);
printf("E/cyc   = %5.4g,  UPPERleg= %6d, BRIDGEstate= %6d  \n",
       2*dQ23*(1-pow(((A*(ycc-z2)+Vdead)/V1),.4)) , UPPERleg, BRIDGEstate);
```

```
/********************** Output results ********************************/
ofp1 = fopen("C:/users/El-Borai/matlab/d2.m","w");
/*generate a matlab script*/

fprintf(ofp1,"%%  Linear Alternator Simulation Output Data File\n");
fprintf(ofp1,"%%--shihab m. elborai,\n %% MIT ESL\n");
fprintf(ofp1,"V_batry = %3.2g;\n R_batry = %3.2g;\n V_diode = %3.2g;\n",
V_batry ,R_batry,V_diode);
fprintf(ofp1,"R_load = %3.2g;\n\n",R_load);

fprintf(ofp1,"wm=%4.3g; tm=%4.3g; lm=%4.3g; tg=%4.3g;\n",wm,tm,lm,tg);
fprintf(ofp1,"wi=%4.3g; Ncoils=%3g; Br=%4.3g;\n\n",wi,Ncoils,Br);

fprintf(ofp1,"Lw=%4.3g; q2=%4.3g; Rw=%4.3g;\n\n",Lw,q2,Rw);

fprintf(ofp1,
"D_piston=%4.3g; clearance=%4.3g; Y1=%4.3g; Vdead=%5.3e;\n",
D_piston,clearance,Y1,Vdead);
fprintf(ofp1,"V1 = %4.3e; V2min = %4.3e; dQ23 = %4.3g;\n\n",V1,V2min,dQ23);

fprintf(ofp1,"A=%5.3e; p1=%4.3e; gama=%4.3g;\n",A,p1,gama);
fprintf(ofp1,"ycc = %4.3g; z1 = %4.3g; z2 = %4.3g; KC = %4.3g;\n\n",ycc,z1,z2,KC)

fprintf(ofp1,"M = %4.3g; K = %4.3e; B = %4.3g;\n\n",M,K,B);
fprintf(ofp1,
"%s %g; UPPERleg= %d; BRIDGEstate  = %d;\n\n\n","Epcyc = ",
2*dQ23*(1-pow(((A*(ycc-z2)+Vdead)/V1),.4)) , UPPERleg, BRIDGEstate );

fprintf(ofp1,"%%  The solution to the state equations is in dmatrix p\n");
```

```
fprintf(ofp1,"%%  dmatrix p has four column dvectors [t   z(t)  v(t)  i(t)]\n\n\n")

fprintf(ofp1, "p = [ \n");
for (i=1;i<=kount;i++)
if((i % 256)==0)
  fprintf(ofp1,
  "%10.4g %10.4g  %10.4g  %10.4g  %10.4g  %10.4 %10.4 %10.4g %10.4e\n",
  tt[i], yy[1][i],yy[2][i],yy[3][i],yy[4][i],yy[5][i], yy[6][i]);
fprintf(ofp1,  "];\n");
fprintf(ofp1,"t=p(:,1);\n");

fprintf(ofp1,"z=p(:,2);\n");
fprintf(ofp1,"v=p(:,3);\n");
    fprintf(ofp1,"i=p(:,4);\n");
fprintf(ofp1,"power=p(:,5);\n");
fprintf(ofp1,"Fg=p(:,6);\n");
fprintf(ofp1,"t_fire=p(:,7);\n");

fprintf(ofp1,"stepsize=%g;\n",h);
fclose(ofp1);

/*************** Allways cleanup after you're done! ****************************/
free_dmatrix(yy,1,1);
free_dvector(tt,1);
free_dvector(vstart,1);
}
```

A.2 nrutil.h

```
#include <stdio.h>
```

```
#include <stddef.h>
#include <stdlib.h>

#define NR_END 1
#define FREE_ARG char*

#ifndef _NR_UTILS_H_
#define _NR_UTILS_H_

static float sqrarg;
#define SQR(a)((sqrarg=(a)) == 0.0 ? 0.0 : sqrarg*sqrarg)

static double dsqrarg;
#define DSQR(a) ((dsqrarg=(a)) == 0.0 ? 0.0 : dsqrarg*dsqrarg)

static double dmaxarg1, dmaxarg2;
#define DMAX(a,b)
        (dmaxarg1=(a),dmaxarg2=(b),(dmaxarg1)>(dmaxarg2)?(dmaxarg1):(dmaxarg2))

static double dminarg1, dminarg2;
#define DMIN(a,b)
        (dminarg1=(a),dminarg2=(b),(dminarg1)<(dminarg2)?(dminarg1):(dminarg2))

static float maxarg1, maxarg2;
#define FMAX(a,b)
        (maxarg1=(a),maxarg2=(b),(maxarg1)>(maxarg2)?(maxarg1):(maxarg2))

static float minarg1, minarg2;
#define FMIN(a,b)
        (minarg1=(a),minarg2=(b),(minarg1)<(minarg2)?(minarg1):(minarg2))
```

```
static long lmaxarg1, lmaxarg2;
#define LMAX(a,b)
        (lmaxarg1=(a),lmaxarg2=(b),(lmaxarg1)>(lmaxarg2)?(lmaxarg1):(lmaxarg2))

static long lminarg1, lminarg2;
#define LMIN(a,b)
        (lminarg1=(a),lminarg2=(b),(lminarg1)<(lminarg2)?(lminarg1):(lminarg2))

static int imaxarg1, imaxarg2;
#define IMAX(a,b)
        (imaxarg1=(a),imaxarg2=(b),(imaxarg1)>(imaxarg2)?(imaxarg1):(imaxarg2))

static int iminarg1, iminarg2;
#define IMIN(a,b)
        (iminarg1=(a),iminarg2=(b),(iminarg1)<(iminarg2)?(iminarg1):(iminarg2))

#define SIGN(a,b) ((b) >= 0.0 ? fabs(a) : -fabs(a))


void nrerror(char error_text[])
     /* Error handler*/
{
  fprintf(stderr,"Numerical Recipies run-time error...\n");
  fprintf(stderr,"%s\n",error_text);
  fprintf(stderr,"...now exiting to system...\n");
  exit(1);
}

double *dvector(long nl, long nh)
```

```
    /* allocate a float vector with subscript range v[nl..nh] */
{
  double *v;
  v = (double *)malloc((size_t) ((nh-nl+1+NR_END)*sizeof(double)));
  if (!v) nrerror("allocation failure in dvector()");
  return v-nl+NR_END;
}

int *ivector(long nl, long nh)
    /* allocate a float vector with subscript range v[nl..nh] */
{
  int *v;
  v = (int *)malloc((size_t) ((nh-nl+1+NR_END)*sizeof(int)));
  if (!v) nrerror("allocation failure in ivector()");
  return v-nl+NR_END;
}

double **dmatrix(long nrl, long nrh, long ncl,long nch)
{
  long i, nrow=nrh-nrl+1,ncol=nch-ncl+1;
  double **m;

  m=(double **) malloc((size_t)((nrow+NR_END)*sizeof(double*)));
  if (!m) nrerror("allocation failure 1 in dmatrix()");
  m += NR_END;
  m -= nrl;

  m[nrl]=(double*) malloc((size_t)((nrow*ncol+NR_END)*sizeof(double)));
  if (!m[nrl]) nrerror("allocation failure2 in dmatrix()");
  m[nrl]+=NR_END;
```

```
  m[nrl]-=ncl;
  for (i=nrl+1;i<=nrh;i++) m[i]=m[i-1]+ncol;
  return m;
}

void free_dvector(double *v, long nl)
     /* free a float vector allocated with vector() */
{
  free((FREE_ARG) (v+nl-NR_END));
}

void free_dmatrix(double **m, long nrl,long ncl)
{
  free((FREE_ARG)(m[nrl]+ncl-NR_END));
  free((FREE_ARG)(m+nrl-NR_END));
}


#endif
```

References

1. Cravalho, E. G., Smith, J. L. Jr., Engineering Thermodynamics, Pitman(1981)

2. Fitzgerald, A. E., Kingsley, C. Jr., Umans, S. D., Electric Machinery, McGraw-Hill(1990)

3. Haus, H. A., Melcher, J. R., Electromagnetic Fields and Energy, Prentice Hall(1989)

4. Galitello, K., Two-Stroke Cycle Engine, U.S. Patent Application No. 281,530, Application filed May 16, 1980, U.S. Patent No. 4,876,991, Patent issued October 31, 1989.

5. Woodson, H., Melcher J. R., Electromechanical Dynamics, Part I: Discrete Systems, John Wiley and sons(1968)